The geometry and evolution of deformation bands in volcaniclastic rocks: insights from Eastern Taiwan

Master in Basin and Reservoir Studies

Martin Kjenes

Department of Earth Science
University of Bergen
February, 2018

Abstract

Deformation bands are millimeter to centimeter tabular zones formed by strain localization in porous, granular media, most commonly found in porous sandstones. They also occur in carbonates and volcaniclastics, but are less understood in these rocks. This MSc thesis characterizes deformation bands in volcaniclastic rocks through field-based studies carried out in deformed tuffs in Shihtiping, Eastern Taiwan, in an attempt to document their geometry, evolution and deformation mechanisms. The studied bands are hosted in a 38-meter-thick succession of pyroclastic and volcaniclastic deposits that formed related to the Luzon volcanic arc activity in Miocene times. Subsequently, the bands developed in response to shortening due to plate convergence between the Eurasian Plate and Philippine Sea Plate.

Three types of deformation bands are documented in the studied Shihtiping succession. The classification is based upon the orientation of the bands relative to bedding, kinematic vector, and the porosity decrease relative to the host rock, and are termed: i) *Pure compaction bands* which express loss of volume/porosity without shear displacement, ii) *Reverse compactional shear bands* and, iii) *Strike-slip compactional shear bands* that show cataclastic deformation mechanisms and slip surfaces. Findings in this study suggests that interplay between granular flow and cataclastic mechanisms dominate development of the studied deformation bands. Notably, both mechanisms are heavily influenced the orientation of mineral cleavage relative to the deformation band. Microstructural investigations have, for the first time, documented the occurrence of S-C fabric in deformation bands within volcaniclastic host rocks. Further findings within this thesis shed light on the on the geometry and evolution of deformation bands in porous, non-welded tuffs. Field-observations and microstructural evidence suggests that *pure compaction bands* were the first to develop, followed by *reverse compactional shear* bands and *strike-slip compactional shear bands*, respectively.

In addition to improving the understanding of deformation bands in volcaniclastic rocks, this outcrop-based study provides analogs for volcaniclastic subsurface reservoirs. This can further lead to an advance in the understanding of reservoirs, concerning, e.g. geothermal energy, hydrocarbons, groundwater contamination, and ore deposition.

Acknowledgements

This thesis is part of my MSc degree in Structural Geology at the Department of Earth Science at the University of Bergen. First and foremost, I would like to express my deepest gratitude to my main supervisor Prof. Atle Rotevatn for guidance, support, motivation and great discussions over the last two years. Thank you for always being positive and keeping me focused. I would also like to express my sincere gratitude to my co-supervisor Prof. Thibault Cavailhes for your guidance, feedback and undivided interest in this project. Thank you for inviting Hanna Serina Jervidalo and me to Bordeaux for a "workshop-week" with our projects. In addition, I would like to thank Dr. Eivind Bastesen, Maria Erichsen Ordemann and Maria Marvik for your contributions during our fieldwork.

A special thanks to both Irene Heggstad and Leif-Erik Rydland Pedersen for assistance regarding the Scanning Electron Microscope. Ray Leadbitter at the Independent Petrographic Services in Aberdeen is thanked for providing this project with amazing thin sections. I also want to send my gratitude to Mr. and Mrs. Wang at the "Sea Fan Guesthouse" for great hospitality and kindness, despite our language barriers.

I want to thank my fellow students and friends at the University in Bergen for your endless support and companionship. Thank you for making the last years the time of my life. Special thanks are directed to Tone Hetland Hansen, Kristine Sleen Jensen, Synne Skaar Ågotnes, Vilde Dimmen and Theodor Lien for proof reading and feedback. I would also send my gratitude to my family who have been patient and supportive during my "absence" from the outside world.

BKK are acknowledged for funding this project and making it possible for us to study deformation bands on the island of Taiwan.

Last, but not least, I would like to thank my friend and field partner, Hanna Serina Jervidalo, for excellent company, support, discussions and lots of great memories throughout these years. Thank you for putting up with me throughout our journey of deformation bands in Taiwan, Bordeaux and Bergen. I could not have asked for a better travel companion, and partner in crime.

Martin Kjenes

Bergen, February 2018

CONTENTS

1 Introduction

1.1 Rationale and background

Deformation bands (DBs) are millimeter- to centimeter-thick tabular zones formed by strain localization in porous granular media, widely reported from porous sandstones (e.g. Aydin, 1978; Antonellini et al., 1994; Fossen et al., 2007; Torabi and Fossen, 2009). The microstructure and evolution of DBs have been a topic of interest ever since they were first described by Aydin (1978). In addition, particular interest has been devoted to DBs due to their influence on petrophysical properties (porosity and permeability) (e.g. Fossen and Bale, 2007; Sternlof et al., 2006; Kolyukhin et al., 2010; Ballas et al., 2015), and their ability to affect fluid flow within subsurface reservoirs/acquifers (e.g. hydrocarbon, geothermal or groundwater reservoirs). Although extensively researched in sandstones (e.g. Aydin and Johnson, 1978; Aydin and Ahmadov, 2009; Charlampidou et al., 2011) and to some extent in carbonate rocks (e.g. Rustichelli et al., 2012; Tondi et al., 2012; Rotevatn et al., 2017), less attention has been devoted to DBs in porous volcaniclastic rocks.

Despite some existing work on DBs in volcaniclastic rocks (e.g. Wilson et al., 2003; Evans et al., 2004; Okubo et al., 2012), there are a range of open questions related to their evolution, occurrence, geometry, mechanisms of formation, and influence on fluid flow. Internal properties of host rocks related to DB development is also still unclear. In addition, volcaniclastic rocks are known reservoir rocks for hydrocarbons, groundwater and geothermal systems (Feng, 2008; Farooqui et al., 2009; Vinciguerra et al., 2009; Lenhardt and Götz, 2011; Mielke et al., 2015; Tang et al., 2017). Outcrop-based studies are important in order to advance the understanding of DBs in porous volcaniclastic rocks. This project represents such a contribution, presenting an outcrop-based study of DBs affecting a well-exposed volcaniclastic succession in eastern Taiwan.

1.2 Aims and objectives

Motivated by the above, the main aims of this thesis are to improve the understanding of the overall structure and evolution of DBs in porous volcaniclastic rocks. Particularly, it is an aim to better understand the deformation mechanisms responsible for DBs formation in volcaniclastic rocks. The aims are achieved through the specific objectives listed below:

i. Document, characterize and sample DBs from the studied outcrops.
ii. Analyze the microstructural and lithological/mineralogic characteristics of DBs and host rocks by the means of standard optical microscope and Scanning Electron Microscope.
iii. Investigate and document any porosity contrast between the host rocks and DBs by the means of digital image analysis techniques.

1.3 Study area

This thesis is based on fieldwork carried out on the island of Taiwan in East Asia (Fig. 1.1A). The studied outcrops are comprised of wavecut platforms and cliff exposures at and around a coastal cliff (termed 'Cuesta' locally and herein) along the coastline of Shihtiping (Fig. 1.1C). The Cuesta is located in the eastern part of the Coastal Range, which is delineated to the east by the coastline and to the west by the Longitudinal Valley Fault (Fig. 1.1B). The Coastal Range, and the studied succession, represents the relict and deformed Luzon volcanic arc (Sibuet and Hsu, 2004), which collided and accreted onto the Eurasian Plate during plate convergence of the latter and the Philippine Sea Plate (Malavieille and Trullenque, 2009). The Longitudinal Valley is a large, seismically active strike-slip fault system, which separates the Philippine Sea Plate (of which the Coastal Range is part) and the Eurasian Plate (Yu and Kuo, 2001).

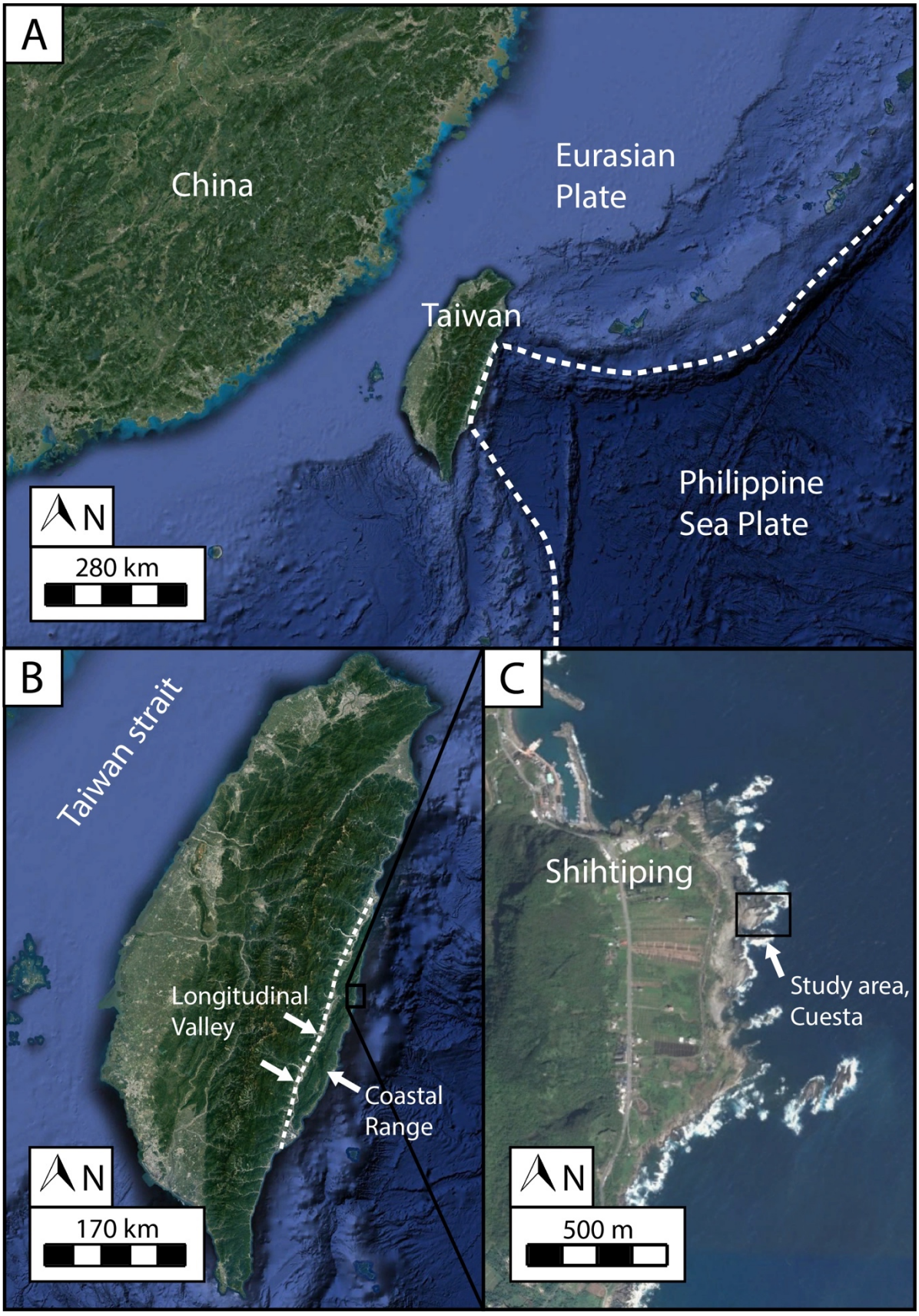

Figure 1.1: A) Satellite photo of Taiwan and South-East China. Tectonic plates are highlighted. B) Satellite photo of the island of Taiwan, pointing out the Longitudinal Valley and the Coastal Range. C) Satellite photo, zooming in on the eastern coastline of Taiwan, pointing out the study area in Shihtiping. Image courtesy of Google Earth.

2 Geological setting

The purpose of this chapter is to introduce and provide an overview of the geologic, tectonic and stratigraphic evolution of Taiwan. Additionally, this chapter outlines the local geologic context in which the studied area is set. The area of focus is the Coastal Range, which is situated along the eastern coast of Taiwan.

2.1 Regional tectonic framework

The island of Taiwan is situated at the junction of the Eurasian and Philippine Sea Plate, and prone to continuous tectonic convergence (Fig. 2.1A) (Yui et al., 2012). East of Taiwan, the Philippine Sea Plate is being subducted beneath the Ryukyu arc. South of Taiwan, the oceanic lithosphere of the South China Sea is being subducted beneath the Philippine Sea Plate, inducing volcanism within the Luzon Arc (Fig. 2.1B) (Teng, 1990; Sibuet and Hsu, 2004; Malavieille and Trullenque, 2009). In terms of the present-day appearance and tectonic framework, Taiwan can be subdivided into two major geological provinces, separated by the Longitudinal Valley (Fig. 2.1B). The eastern part is defined as the Coastal Range, which is a relict volcanic arc-forearc basin of the Luzon Arc. The western part constitutes of the fold-and-thrust belt (Coastal Plain, Western Foothills and Hsuehshan Range) and a relict accretionary prism (Central Range) (Fig. 2.1C) (Chen et al., 2017).

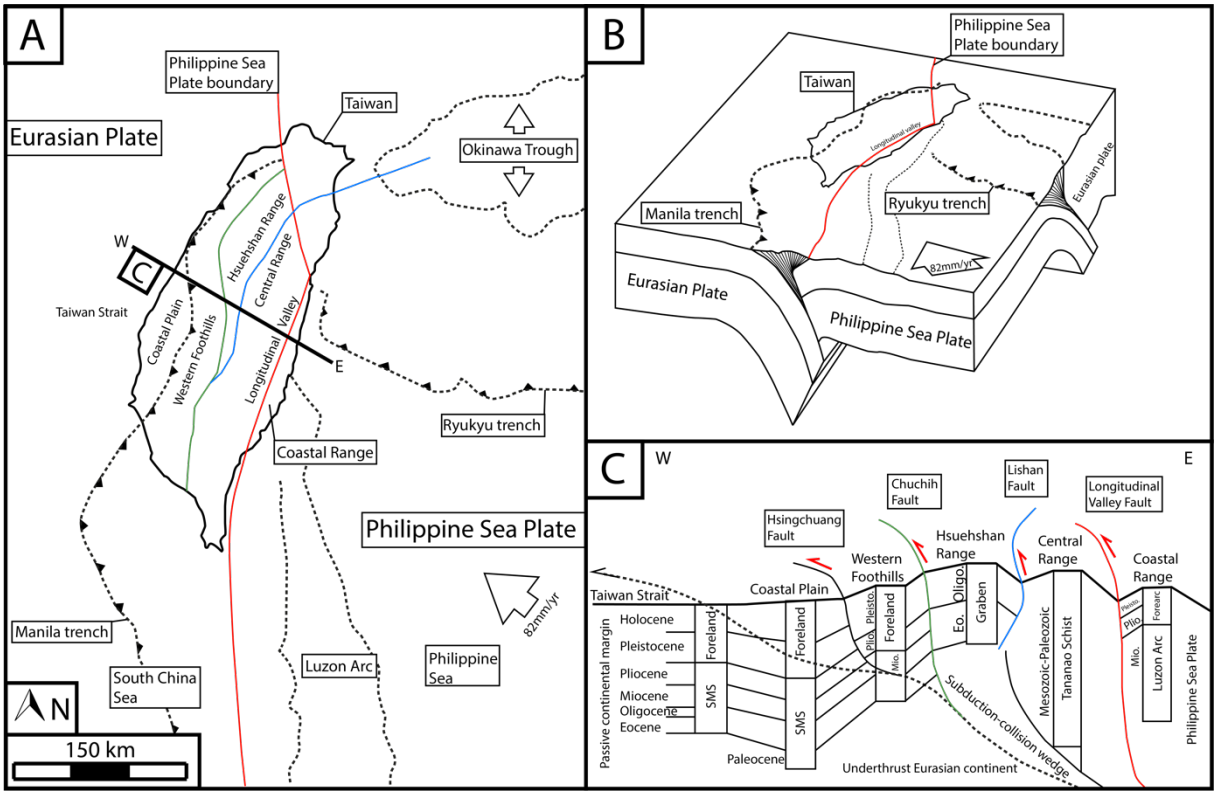

Figure 2.1: Overview of the geodynamic framework of the Taiwan area. A) Map overview of the surrounding tectonics of Taiwan, modified from Sibuet and Hsu (2004). B) Block diagram showing arc-continent collision and tectonic setting. Modified from Chang et al. (2001). C) Tectonostratigraphic cross section derived from the line C in A), which shows a summary of the units and major geologic provinces within the Taiwan orogen. SMS: Shallow marine siliciclastics. Modified from Chang et al. (2001).

The uplift and evolution of Taiwan is the result of the collision between the Luzon arc and the Eurasian plate, which occurred in Middle Miocene to Late Pliocene (Chai, 1972; Page and Suppe, 1981; Ho, 1986; Teng, 1990; Malavieille and Trullenque, 2009). However, additional events and specific age relations are debated and uncertain.

The initial state that induced the formation of Taiwan started with a major plate reorganization along the Pacific plate around 16 Ma (Early Miocene) (Sibuet and Hsu, 1997). About 15 Ma ago, the Manila trench became active due to the consumption of the oceanic lithosphere of the South China Sea by the Philippine Sea plate. The Manila trench extended northwards to the Ryukyu subduction zone, which became inactive due to the plate reorganization, along the western boundary of the Philippine archipelago. As a result, the Luzon arc developed as an intra-oceanic arc (Fig. 2.2a) (Sibuet and Hsu, 2004; Yui et al., 2012).

The young Luzon arc acquired significant topographic expression to resist the subduction around 9 Ma ago, and started to collide obliquely with the Eurasian Plate (Sibuet et al., 2002; Sibuet and Hsu, 2004). During the collision process, the forearc basin (North Luzon

Trough) and its basement were consumed until the Luzon volcanic arc was juxtaposed next to the fold-and-thrust belt of Taiwan in the mature collision zone (Fig. 2.2b) (Hirtzel et al., 2009). The Philippine Sea plate was moving westwards with a constant velocity of 5-9 cm/year (Sibuet and Hsu, 2004; Lai and Song, 2013; Thomas et al., 2014a; Thomas et al., 2014b). Subsequently, the Luzon experienced a 20° counter-clockwise rotation (Stephan et al., 1986). Manila-Ryukyu transform fault was consumed as a result of the continuously subduction and rotation of the Philippine Sea plate. This initiated a collision between the opposite-verging Manila trench and Ryukyu trench (Sibuet and Hsu, 1997). In addition, the collision between the Ryukyu subduction zone and the Luzon arc started 9 Ma ago, based on constant westward motion of the Luzon arc (4.5 cm/year with respect to Eurasia) (Sibuet and Hsu, 1997; Sibuet and Hsu, 2004). Exhumation of metamorphic basement in the Central range is caused by the westward thrusting and accretion of the Luzon arc and forearc sequence. This marks the final stage of the arc-continent collision (Fig. 2.3c) (Thomas et al., 2014a).

The Proto-Taiwan chain, in western Philippine Plate boundary, increased in length, but continuously subsided due to both erosional processes and extension in the newly opened Okinawa Trough backarc basin. The Okinawa trough opened 6 Ma ago (Sibuet and Hsu, 2004). Erosion increased as the uplift of Taiwan progressed, and the products of erosion were deposited on the continental margin south of the ocean-continent transition zone within the Eurasian slab and in the Manila trench (Sibuet and Hsu, 2004).

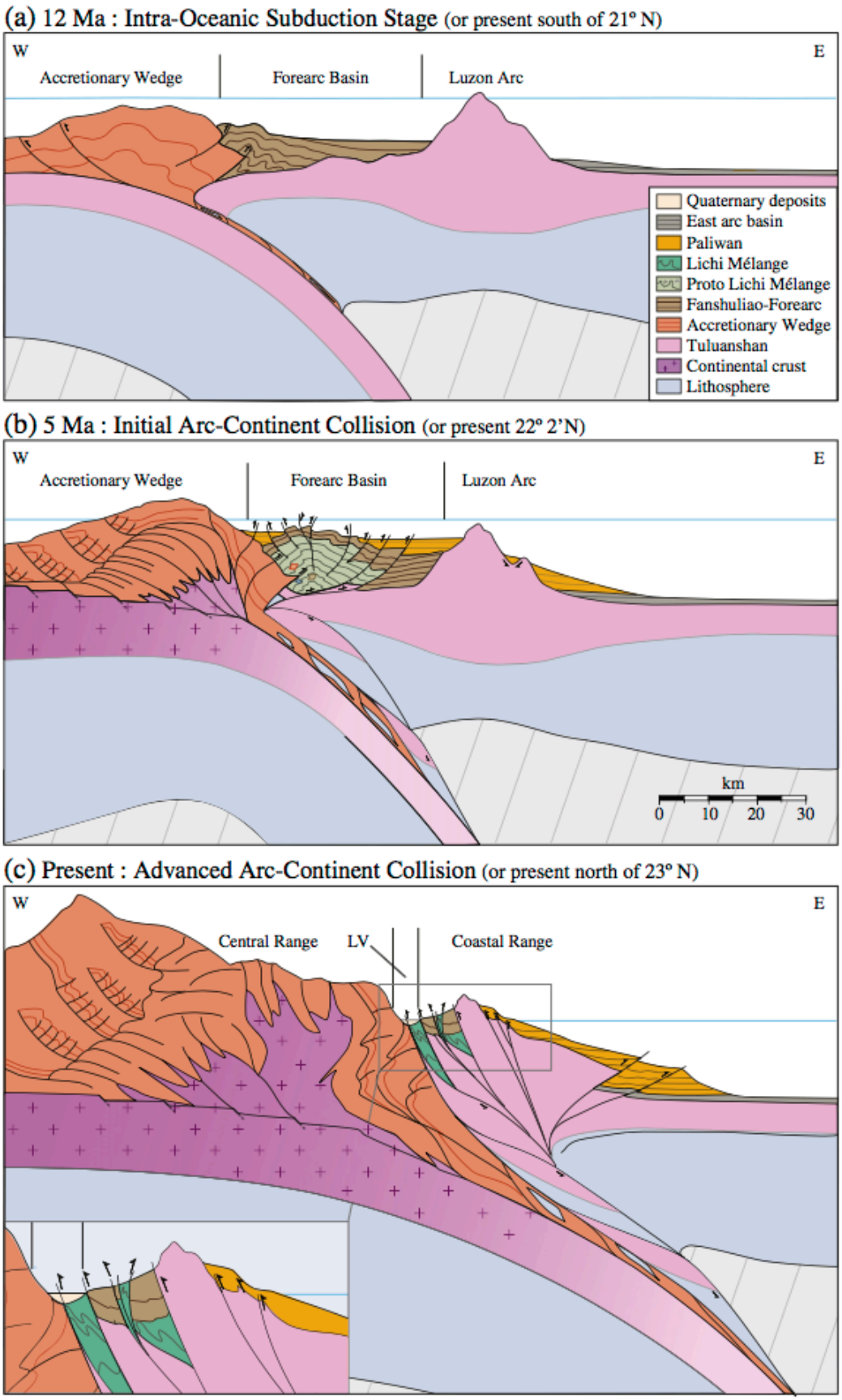

Figure 2.2: Sequential step-by-step model of the arc-continent collision, from Thomas et al. (2014a). The Luzon arc and forearc are thrusted westwards by the subduction of the Eurasian margin. A) Intra-oceanic subduction stage and the creation of the Luzon arc. B) Initial arc-continent collision stage. C) Present tectonic framework of the area, highlighting the Coastal Range (relict Luzon arc and forearc).

2.1.1 Eastern Coastal Range

The Coastal Range, also known as the Hai'an Range, is a 150 km long and approximately 15 km wide mountain chain located along the eastern coast of Taiwan, which represents the western edge of the Philippine Sea plate (Jahn et al., 1986; Hsieh et al., 2004; Sibuet and Hsu, 2004; Yamaguchi and Ota, 2004; Malavieille and Trullenque, 2009; Yui et al., 2012). The Coastal Range also corresponds to the outcropping portion of the relict Luzon Arc, and is separated from the Eurasian margin by the Longitudinal Valley (Barrier and Angelier, 1986; Kosuga et al., 1988; Sibuet and Hsu, 2004). The Longitudinal Valley delineates the Coastal Range to the east as an active thrust fault with a minor sinistral strike-slip component (Teng and Wang, 1981; Malavieille and Trullenque, 2009), where the Coastal Range is overthrust onto Central Range (Barrier and Angelier, 1986). The Coastal Range is structurally characterized by low-angle east-dipping imbricate thrust faults, and NNE- trending synclines and anticlines (Ho, 1986).

The island arc character of the Coastal Range can be recognized today from the lithological characteristics of the relict island arc lithofacies, i.e. the Tuluanshan formation, the Lichi formation and the Fanshuliao formation (Teng and Wang, 1981; Liew et al., 1993).

Based on the background information provided in chapter 2.1, the Coastal Range is a result of the subduction and collision of the Luzon arc, as a part of the Philippine Sea plate, and the Eurasian margin around 12-9 Ma ago. As the accretion of the island arc and the continental front developed, the magma generated from the subduction zone continually erupted, which instituted a series of volcanic arc islands (Teng and Wang, 1981). The northern tip of the Luzon island arc collided with the Eurasian continental margin as the plate motion progressed, which formed the Central Range to the west due to buckling of the continental margin (Barrier and Angelier, 1986). Consequently, the rocks of the Coastal Range were continuously deformed and thrusted upon the margin (Teng and Wang, 1981).

2.2 Lithostratigraphy

The studied area for this thesis consist solely of the Shihtiping White Tuff unit, which belongs to the Tuluanshan Formation (Barrier and Angelier, 1986; Teng et al., 1988). The lithostratitgraphy of the Coastal Range in eastern Taiwan can be subdivided into five different units based on the major lithology:

i. The Tuluanshan Formation
ii. The Fanshuliao Formation
iii. The Lichi Formation
iv. The Paliwan Formation
v. The Peinanshan Conglomerate

Four volcanic bodies have been studied by Lai and Song (2013), in terms of understanding the evolutionary model of the Costal Range and the northern Luzon Arc. During collision, the volcanoes became dormant or extinct, before they were uplifted and accreted by additional collision. The five lithostratigraphic units are composed of the material of these volcanoes, and their variety of rock types reflects the origin in terms of geological setting of the Costal Range. The Tuluanshan Formation is comprised of andesitic volcanics and associated volcaniclastic limestones, while the Fanshuliao Formation consist of volcanogenic bioclastic flysch. These are the volcanic sequences within the stratigraphy of the Coastal Range (Teng and Wang, 1981). The Lichi Formation represents Mélange from the relict forearc sequence, while the Paliwan Formation reflects lithic flysch and polymictic conglomerate (Chen et al., 2017). The Peinanshan Conglomerate is comprised of molassic conglomerate beds along the eastern slope of the Central Range (Teng and Wang, 1981).

2.2.1 Tuluanshan Formation

The volcanics of the Tuluanshan formation originates from the aforementioned Luzon arc, which formed in response to the subduction of the South China Sea plate beneath the Philippine Sea plate (Teng, 1990; Song and Lo, 2002). The Tuluanshan formation is defined as the volcanic basement of the Coastal range and is estimated to be at least 1500 m thick (Chai, 1972; Barrier and Angelier, 1986; Ho, 1986).

The Tuluanshan formation is comprised by a large variety of volcanic- and volcaniclastic rocks, such as agglomerates, tuffs, conglomerates, tuffaceous conglomerates, lapillistones and

associated limestones (Teng and Wang, 1981; Teng et al., 1988; Song and Lo, 2002). The various rocks are of andesitic origin, and are dated by K-Ar to Middle Miocene to Early Pliocene age (16-5 Ma) (Teng et al., 1988; Song and Lo, 2002). Petrochemical analyses done by Chen (1975) and Miyashiro (1974) of the igneous formation shows that the rocks belong to the calc-alkalic series, while some are of more tholeiitic composition. Lithologically, hornblende andesite is the most dominant rock type in the Tuluanshan formation (Song and Lo, 2002).

The Tuluanshan formation is divided into four lithostratigraphic subunits, based on the major lithology (Song and Lo, 1988; Teng et al., 1988):

i. The Chimei Igneous Complex
ii. The Shipmen Volcanic Breccia
iii. The Shihtiping White Tuff
iv. The Kangkou Limestone

The latter units reflect the evolutionary state of the island arc and shows the evolution of the volcanoes within the Luzon arc. Volcanic eruptions commenced in a deep marine environment in Early Miocene, where mainly massive lava flows, pillow lavas and hyaloclastites were produced (Song and Lo, 1988, 2002; Lai and Song, 2013). In the Middle to Late Miocene, the arc reached a shallower environment, which is reflected in the abundance of volcaniclastic rocks (Song and Lo, 2002). The volcano breached the surface and became subaerially exposed in the Late Miocene to Early Pliocene, which is reflected by the abundance of ignimbrites and pyroclasts in the rock record from this period onwards (Song and Lo, 1988). The presence of impacted, fractured sag-blocks, plastic deformation and erosional process in the ignimbrite also support this assumption (Song and Lo, 2002).

2.2.2 The Shihtiping White Tuff

The Shihtiping White Tuff is a member of the Tuluanshan formation (Fig. 2.3A), and the main lithology of interest in this study. The investigated deformation bands (DBs) occur in this 100 meter section, consisting of pyroclastic- and volcaniclastic rocks ranging from breccias, lapillistones, and coarse- to fine-grained tuffs (Song and Lo, 1988). The uppermost part, approximately 30-40 meters, is outcropped at Cuesta, in Shihtiping. The outcropping part of

the succession is shown in Fig. 2.3B, and is dominantly comprised by tuffaceous sandstone and ignimbrites (Song and Lo, 1988, 2002; Lai and Song, 2013).

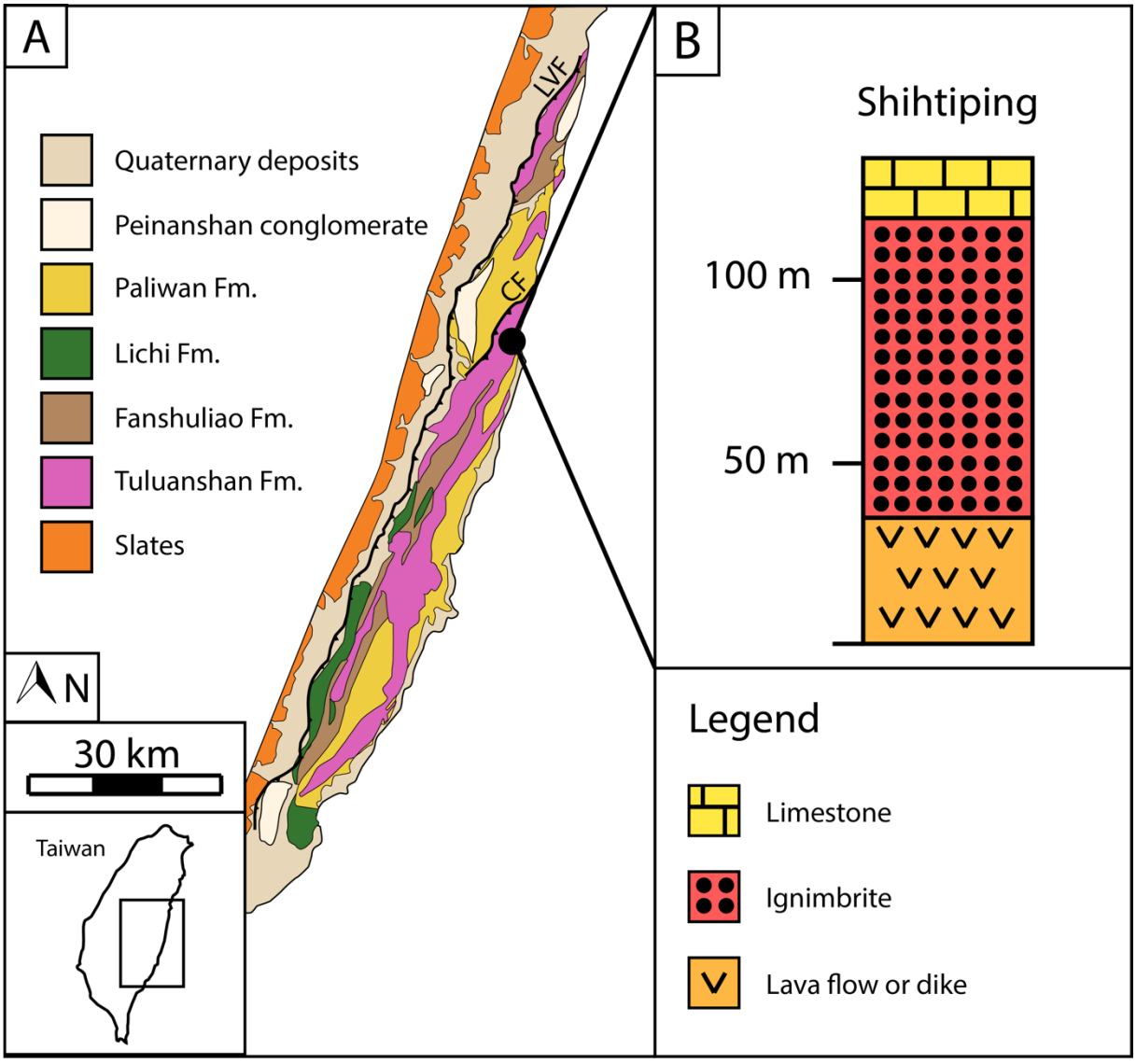

Figure 2.3: A) Geological map of the Coastal Range, modified after Thomas et al. (2014a). B) Representation of the previously logged Shihtiping area by Song and Lo (2002). CF: Chimei Fault. LVF: Longitudinal Valley Fault. Modified after Lai and Song (2013).

Based on studies carried out by Song and Lo (2002), the tuffs are interpreted to be deposits from volcanic surge, which is produced by the collapse of eruption columns during magmatic eruptions. In addition, juvenile fragments within the ignimbrites occasionally occur as accessory lithic grains, which might be a result from a ground derived surge or an ash-cloud surge by a phreatomagmatic eruption (Song and Lo, 2002). The pyroclastic and volcaniclastic rocks of Shihtiping are dated to be of later Miocene age (Song and Lo, 1988).

The lithological layers of the Shihtiping White Tuff exhibits different depositional structures, which reflects the environment of accumulation, i.e. cross- and parallel laminations, normal and reverse graded beddings, impacted sag blocks, plastic deformations and erosion surfaces (Song and Lo, 1988). These structures are related to subaerial environments. The ignimbrites show abundance of eutaxitic texture and welded beddings, which also implies a subaerial depositional environment (Song and Lo, 2002). The depositional structures will be shown in Chapter 5 Results, in the stratigraphic log of the studied area.

3 Theoretical background

The purpose of this chapter is to provide an introduction to the state-of-the-art related to the deformation bands (DBs). Since DBs have mainly been studied in siliciclastic rocks, namely porous sandstones, it is necessary to deal with DBs occurring mainly in sandstones first (section 3.1), before introducing DBs in volcaniclastics (section 3.2).

3.1 Deformation bands

DBs are millimeter to centimeter thick tabular zones formed by strain localizing in porous granular media (e.g. Aydin, 1978; Wilson et al., 2006; Fossen et al., 2007; Torabi and Fossen, 2009; Tondi et al., 2012; Rotevatn et al., 2016). Several characteristics in DBs allow them to be distinguished from discrete faults and fractures. Primarily, the bands tend to have enhanced cohesion and reduce permeability and porosity compared to the host rock, which is associated with strain hardening behavior (Antonellini et al., 1994; Davis et al., 2000; Lothe et al., 2002; Fossen et al., 2007). Also, individual DBs generally do not host discrete slip surfaces, and their offsets are smaller than faults of comparable length (Lothe et al., 2002; Rotevatn and Fossen, 2012). The displacement caused by the DBs is distributed in a shear zone of less than a few millimeters in thickness (Fossen et al., 2007; Rotevatn et al., 2008). DB clusters have been predominantly described and interpreted as fault precursors by Aydin and Johnson (1978). This resulted in a widely accepted three-stage model for sequential development of DBs and resulting fault development in porous sandstones. Although extensively studied in the field, DBs have also been produced and analyzed in experimental studies, e.g. by triaxial compression of rock samples (Mair et al., 2000; Lothe et al., 2002).

DBs may be classified according to kinematics or mechanisms. Based on kinematics, the bands can be classified as dilation bands (volume increase), shear bands (no volume change), compaction bands (volume decrease) or hybrids of these types (Aydin et al., 2006; Fossen et al., 2007; Eichhubl et al., 2010; Fossen et al., 2018). The hybrid bands, or mixed-mode bands, consist of: shear enhanced dilation bands, dilation shear bands, compactional shear bands, and shear enhanced compactional bands (Fig. 3.1). However, the most common DBs are those that are dominated by a combination of shear displacement with volume loss (compaction) (Aydin et al., 2006; Charalampidou et al., 2011; Fossen et al., 2018).

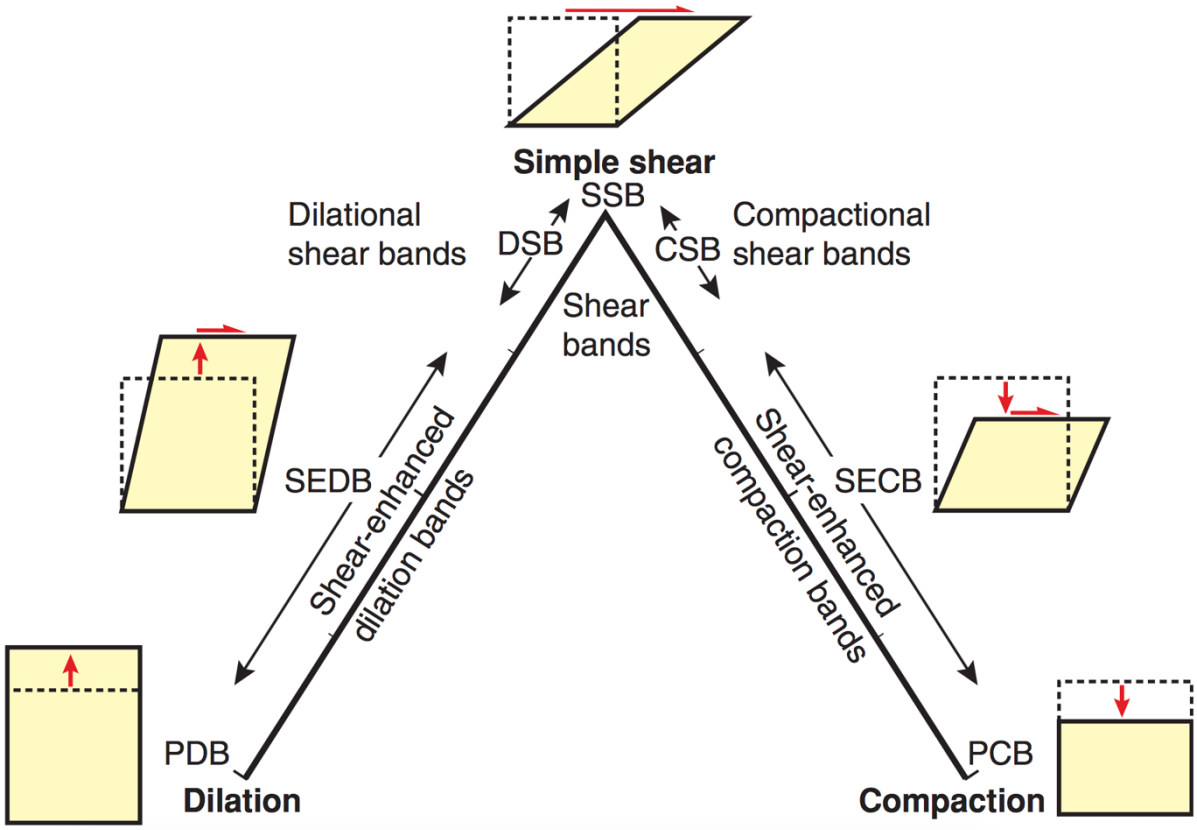

Figure 3.1: Kinematic classification of DBs, which contains three end-members: isochoric shear bands (no volumetric change), compaction bands (negative volumetric change) and dilation bands (positive volumetric change). Combinations of these end-members may occur naturally. From Fossen et al. (2018).

Isochoric, or simple shear, bands are defined by no volume loss, where grains are deformed by rigid rotation and translation (Aydin et al., 2006; Fossen et al., 2018). They are characterized by displacement parallel to the band and rarely found in nature (Engelder, 1974; Aydin et al., 2006).

Compaction bands are characterized by no shear displacement and a low degree of grain comminution (Charalampidou et al., 2011). Strain is accommodated exclusively by compactional volumetric change, which induce localized porosity loss and reduction of permeability (Mollema and Antonellini, 1996; Issen and Rudnicki, 2001; Bésuelle and Rudnicki, 2004; Fossen et al., 2015). Pure compaction DBs have documented and described by e.g. Mollema and Antonellini (1996) and Sternlof et al. (2006) in Jurassic aeolian sandstone. They have also been documented in limestones by e.g. Antonellini et al. (2014) and Rotevatn et al. (2016). In addition, experimental investigations of compaction bands have successfully reproduced such bands in the laboratory (e.g. Baud et al., 2004; Charalampidou et al., 2011).

Dilation bands are distinguished by increasing porosity compared to the host rock in addition to no shear displacement (Antonellini et al., 1994; Du Bernard et al., 2002a; Aydin et

al., 2006). Dilation bands appear uncommon (Fossen et al., 2007), and have been documented by Du Bernard et al. (2002a) in porous, poorly consolidated sand.

As aforementioned, DBs may also be classified according to the dominant deformation mechanism in the formation of the bands. The main mechanisms are: granular flow (disaggregation/reorganization of grains), phyllosilicate smearing, cataclasis, cementation and solution (Fossen et al., 2007; Torabi and Fossen, 2009). These mechanisms are illustrated in Fig. 3.2.

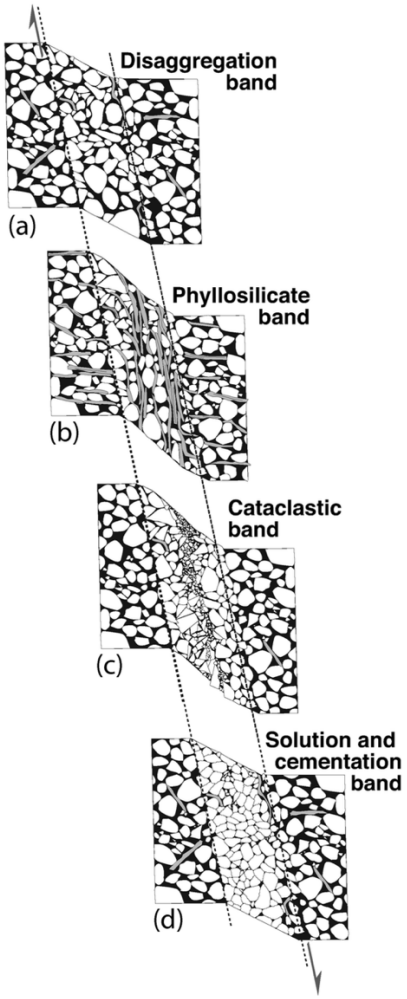

Figure 3.2: Classification system of DBs based on dominant deformation mechanism. A) Disaggregation band form as a result of granular flow. B) Phyllosilicate bands develop as a result of phyllosilicate smearing. C) Catalclastic band occur as a result of grain fracturing and comminution. D) Solution and cementation band develop as a result of solution and cementation processes. Modified after Fossen et al. (2007).

Disaggregation bands are characterized as localized, shear-related disaggregation of grains formed as a result of grain- rolling, translation and boundary sliding (Fossen et al., 2007). These

processes are often referred to granular flow (Twiss and Moores, 1992) or particulate flow (Rawling and Goodwin, 2003). Disaggregation bands are most typically formed at shallow burial depths (< 1 km) and commonly found in poorly consolidated rocks (Bense et al., 2003; Fossen et al., 2007; Torabi, 2014). These bands are usually associated with only a minor reduction in porosity and permeability (Hesthammer and Fossen, 2001).

Phyllosilicate bands, commonly referred to as framework phyllosilicates, develop under the same conditions as disaggregation bands if the phyllosilicate mineral content exceeds 15% (Fossen et al., 2007; Fisher et al., 2009). These bands are thus considered a sub-group of disaggregation bands (Fossen et al., 2003). The platy minerals (e.g. mica) induces frictional grain boundary sliding rather than comminution, resulting in greater offsets than the other types of DBs, respectively (Fisher and Knipe, 2001). Studies by Wibberley (1999) suggests that strain hardening and softening may result from alteration of platy minerals, depending on the behavior of silica released during alteration. In addition, the rearrangement of phyllosilicates parallel to the bands result in a reduction of permeability (Fossen et al., 2018).

Cataclastic bands develop when mechanical grain fracture is the principal deformation mechanism (Aydin, 1978; Fossen et al., 2007; Fossen et al., 2018). Recent studies suggest that the intensity of cataclasis can be subdivided based upon environmental conditions, such as burial depth during deformation and properties of the host rock (Ballas et al., 2015; Fossen et al., 2018). The DBs may evolve from single strands to clusters due to increasing intensity; in more evolved zones, these are associated with slip surfaces (Antonellini et al., 1994; Nicchio et al., 2018). Cataclastic DBs cause relative permeability and porosity reduction, which results in an increase of Bulk and Young's modulus. This induces the strength of the DB, causing it to be stronger and stiffer than the host rock and more resistant to weathering, respectively (Exner and Tschegg, 2012; Rotevatn et al., 2013; Torabi, 2014; Tindall and Eckert, 2015). Cataclastic DBs have been observed in unconsolidated marine sand buried at 80 meters (Cashman and Cashman, 2000), but form more typically at depths of 1.5-2.5 kilometers (Fossen et al., 2007). These bands are documented in a great range of host rocks, e.g. porous sandstone (Du Bernard et al., 2002b), limestones (Rotevatn et al., 2016), unconsolidated sands in accretionary prism sediments (Ujiie et al., 2004), non-welded ignimbrites and tuffs (Wilson et al., 2003) and subglacial till (van der Meer et al., 2003).

Cementation and solution bands are related to coating of grains by minerals, and chemical compaction or pressure solution (Fossen et al., 2007). As shown by Ehrenberg (1993) and Storvoll et al. (2002), cementation is especially promoted in DBs where diagenetic minerals such as chlorite and illite coat the undeformed grains in the host rock. Cementation is a result

of a large grain surface area and the availability of a reactive fractured surface (Fossen et al., 2007). Pressure solution, however, is largely temperature dependent and become pervasive for quartz at > 90°C (burial depths greater than 3 kilometers) (Walderhaug, 1996). These solution bands are promoted by clay minerals on grain boundaries, and commonly consist of tightly packed grains smaller than the host rock (Gibson, 1998; Fossen et al., 2007).

Both external conditions and internal host rock properties are key factors to determine the mechanism of the development of DBs. Internal properties are comprised of porosity, mineralogy, grain size and shape, grain packing geometry and degree of cementation (Fig. 3.3A) (Fossen et al., 2007; Fossen et al., 2018). External conditions include confining pressure (burial depth), deviatoric stress (tectonic environment) and pore-fluid pressure (Torabi et al., 2007; Fossen et al., 2018). However, some of these factors are not constant and subjected to change over time, e.g. increase of confining pressure due to burial depth. In Fig. 3.3B, temporal evolution of DBs in sandstones affected by increasing burial depth and phyllosilicate content is illustrated.

A

Variable	Granular flow → Cataclasis
Burial depth (confining stress)	Shallow → Deep
Lithification	Unconsolidated → Well lithified
Fluid overpressure	High → Low
Cement strength	FeO(OH) (low) → $CaCO_3$ → SiO_2 (high)
Grain roundness	Angular → Rounded
Grain sorting	Poor → Good
Mineralogy (grain strength)	Strong → Weak
Phyllosilicate content	High → None
Tectonic regime	Extensional → Contractional

B

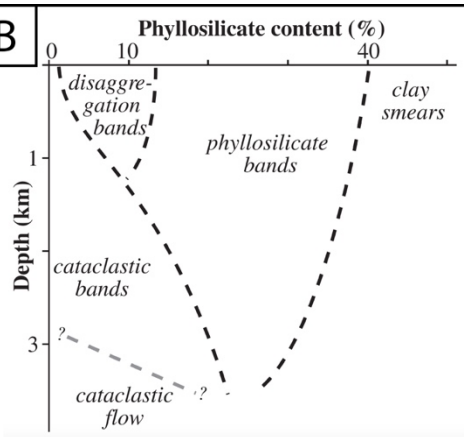

Figure 3.3: Table and schematic illustration of factors influencing the development of DBs. A) Factors influencing the degree of cataclasis presented in a table. Modified after Fossen et al. (2018). B) Schematic illustration showcasing how different DB mechanisms are affected by burial depth and phyllosilicate content. Modified after Fossen et al. (2007).

3.2 Deformation bands in volcaniclastics

As aforementioned, DBs have been predominantly described in siliciclastic rocks. However, the bands have relatively recently been documented in volcaniclastic rocks, mainly in ignimbrites (Wilson et al., 2003) and tuffs (Evans and Bradbury, 2004). DB clusters have been documented on Mars based on characteristic meter-scale architectures and geologic context from High-Resolution Imaging Science Experiment (HiRISE) camera (Okubo et al., 2009; Okubo, 2012). Notably, documentation of DBs in volcaniclastic rocks depend on the degree of welding as a result of their different properties (Wilson et al., 2003, 2006). The welding process sinters and fuses particles together (increases grain-contact area) and decreases porosity, hence increasing the mechanical strength of the rock (Moon, 1993; Soden et al., 2016). Findings from Wilson et al. (2003) suggested that welded units fail by fracture, whereas failure by cataclasis within bands only occur in non-welded units. Thus, the degree of welding works as the key factor for the development of DBs in ignimbrites and tuffs, and the general mode of failure (Wilson et al., 2003; Soden and Shipton, 2013; Korkanç and Solak, 2016). Secondary factors include post-depositional crystallization and weathering (Wilson et al., 2003; Pola et al., 2016).

Non-welded pyroclastic flow deposits, e.g. ignimbrites, are often weakly consolidated, but still accommodate sufficient strength to undergo localized brittle failure (Dinwiddie et al., 2006). Various DBs types have been documented in these volcaniclastic rocks: both dilation and disaggregation bands in ash and pumice beds (Dinwiddie et al., 2012), cataclastic bands in the glassy pumice (Wilson et al., 2003), nonwelded tuffs (Evans and Bradbury, 2004), and in basal pumice-fall deposits (Dinwiddie et al., 2006).

DBs in volcaniclastic rocks accommodate a loss of both porosity and permeability due to pore collapse (Evans and Bradbury, 2004). In addition, a secondary reduction of permeability occurs in unsaturated conditions, as the smaller mean pore size produces an increased capillary effect (McGinnis et al., 2009).

4 Methods

The purpose of this chapter is to give an overview of the methods used in the research presented in this thesis. The field work consisted of six weeks divided into two periods in Shihtiping, Taiwan, during November 2016 and March 2017.

4.1 Field data

Sedimentary-based logging of the volcaniclastic host rocks was conducted in order to gain a better understanding of the studied area and its succession. Further, structural data were acquired in various localities. Measuring tape were aligned parallel to deformation bands (DBs) of interest, in order to quantifying their characteristics (e.g. occurrence, orientation, displacement). UAV (Unmanned Aerial Vehicle) mapping was carried out during the last field season, in order to improve the map quality of cuesta and adjacent areas.

4.1.1 Volcaniclastic logging

In order to describe the volcaniclastic host rock, a stratigraphical log of the cuesta was made for this project. The log was mainly based on field observations, in addition to previous descriptions by Song and Lo (2002), and the sedimentary classification scheme by Folk (1954). Subsequently, the various units within the log are based on quantified differences of grain sizes and generalized clast material, such as pumices and volcanic bombs. The stratigraphic log is made for orientation purposes only, as the DBs are the main focus of this study. Only one log was considered representative, as the studied outcrops are situated at the same stratigraphic level.

4.1.2 Macro and meso localities

Data of the DBs were obtained from various localities which were chosen upon good access, exposure, and the features of the bands. A total of seven bands were selected for further investigations and characterization (Fig. 4.1).

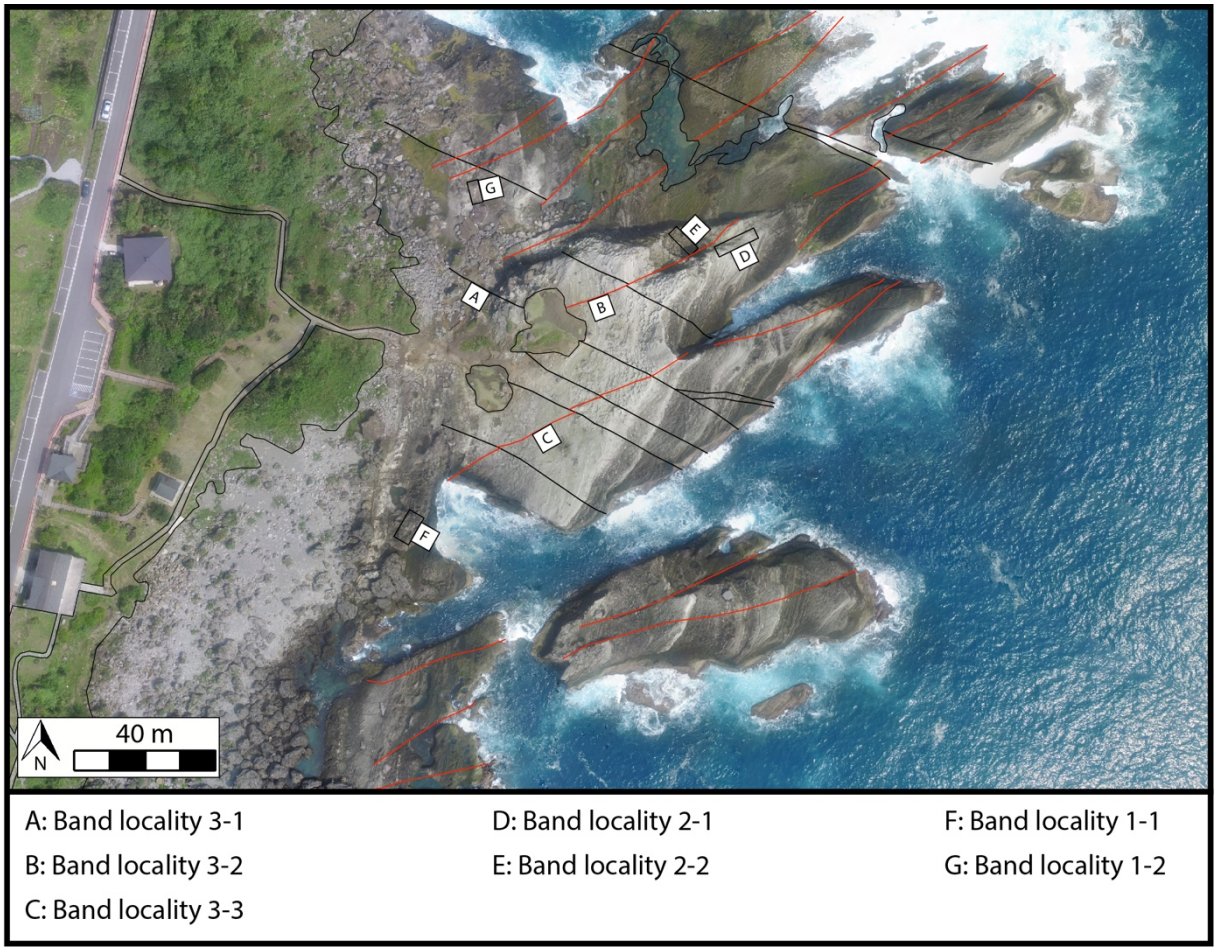

Figure 4.1: UAV photo of the studied area and the band localities. Notably, not all DBs are visually represented in this figure due to their extent. Only localities 3-1, 3-2, 3-3 features these types of bands. The red and black color distinguish similar bands with different orientation. Band localities 2-1, 2-2, 1-1 and 1-2 are carried out in the cross section of the studied area, or too small to be visualized in the UAV photo.

A measuring band was placed parallel to the bands in order to quantify their characteristics and occurrence through the succession. This is referred to as macro localities (> 2 meters in length). However, distinct sections along these bands were further investigated, namely meso localities (< 2 meters). The following data were acquired:

i. Description of locality
ii. DB intensity
iii. DB thickness
iv. Offset
v. Orientations
vi. Rock samples

All of the structural data listed above is well documented in the meso localities (Fig. 4.2B), while only (ii), (iv) and (v) is included in the macro localities (Fig. 4.2A). Subsequently, 40 DB samples were collected for microstructural analysis of the DBs in their respective meso locality (Fig. 4.2C).

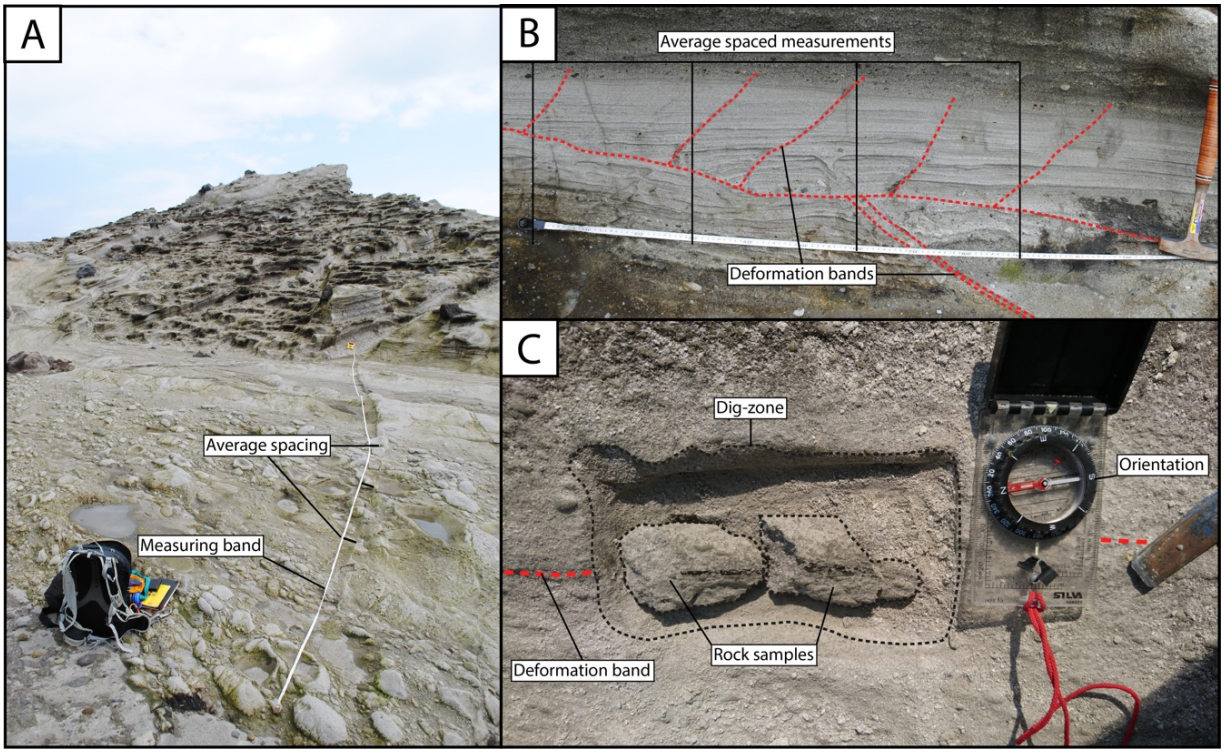

Figure 4. 2: Field photos of the various band localities. A) Macro locality 3-3. Measuring band is stretched out parallel to the band with an average spacing. B) Example of meso locality 2-1-A. Measuring band is stretched parallel to the overall displacement surface. Data is collected perpendicular with an average spacing. C) Example of how rock samples are collected. After finding a suitable sample, a chisel and a geological hammer is used to dig around the area of interest. Orientation of sample is measured, before the sample is marked and wrapped in plastic.

4.1.3 UAV

Images of the studied area were conducted by UAV, model *Phantom Dji 3*, in order to acquire a more detailed overview. The complimentary mapping revealed structures adjacent to the area of interest; two folds were documented by aerial investigations of the entire studied area and unreachable islands along the coastline.

4.2 Microscopic analysis

The collected rock samples from the meso localities were sent to the *Independent Petrographic Services Ltd* in Aberdeen, UK, for preparation of thin sections. The samples were polished to a thickness of 30 microns and injected with blue epoxy with the sole purpose of easier pore space recognition. The characterization of the volcaniclastic host rocks were inspired by IODP's expedition 350 methods by Tamura et al. (2015). The host rocks were analyzed as sedimentary rocks (e.g. grain contacts, sorting), and as igneous rocks (e.g. phenocryst characterization, magmatic texture). However, the quality of samples featuring DBs varies within types and localities. Type 3 bands were the most common bands at Cuesta, thus more abundant sampling. In addition, type 3 bands produced better thin section than the two other types. Type 1 bands resulted in thin section with the poorest quality. Studies by Scanning Electron Microscope were carried out at the University of Bergen and University of Bordeaux.

4.2.1 Regular light microscopy

A *Nikon Eclipse E400 POL*- and *Nikon Eclipse LV100 POL* polarizing microscope was used for the thin section analysis. The latter microscope was used with a *Nikon digital sight DS-Fi1* camera and *NIS Elements F* image software to acquire photos at various magnifications (4X, 10X and 16X). These photos were used for interpretation of structures related to the DBs, and the 2D porosity estimations.

4.2.2 Scanning Electron Microscope

A Scanning Electron Microscope (SEM), *Zeiss Supra 55VP Field Emission SEM*, was used to conduct investigations of the thin sections at a much higher magnification, and to increase the resolution of the porosity measurements. The depth of field is increased in a SEM analysis as it uses a beam of high-energy electrons to form an image of the thin section, which gives the opportunity to study the samples at nanometer scale (Egerton, 2005). The electron source produce electrons by thermionic heating, in addition to accelerate the electrons to an energy level of 0.1-30 keV (Zhou et al., 2006) compressing them into a narrow beam. This beam requires a high-vacuum environment, which disables the electrons to scatter and simultaneously lower the chance of damaging the electron gun (Zhou et al., 2006). A series of electromagnetic lenses (e.g. condenser lenses) (Fig. 4.3) and apertures in the electron column direct and process the electron beam into small, focused electrons on the specimen (Reichelt, 2007).

The thin sections were covered with a thin layer of carbon prior to the SEM analyses to conduct electricity, which prevent accumulation of charge when the electrons hit the samples. The electrons will decelerate on impact, and scatter (inelastically or elastically) into a variety of signals due to their high amount of kinetic energy. These signals are comprised of: heat, visible light, photons (x-rays), backscattered electrons (BSE), diffracted backscattered electrons (EBSD), and secondary electrons (Zhou et al., 2006; Reichelt, 2007).

BSE has been used to illustrate contrasts in composition in multiphase samples. These electrons are scattered elastically and generated from larger volumes of the samples, typically a few micrometers below the specimen surface (Krinsley et al., 2005; Reed, 2005). The backscatter electron detector (BSD) is located overhead the stage (Fig. 4.3) and collects the BSE-signals. These signals provide key information regarding the compositional contrasts, due to the high sensitivity between BSE and the composition of the analyzed specimen (Zhou et al., 2006). The resulting BSE-SEM images from the thin sections are depicted on a visual display monitor and limited to grayscale. Variations in brightness reflects the elements of the mineral, as a higher average atomic number in the elements will cause brighter areas. Identification of these minerals may be carried out by performing point and area analyses with the electron dispersive spectroscopy (EDS) detector (Egerton, 2005).

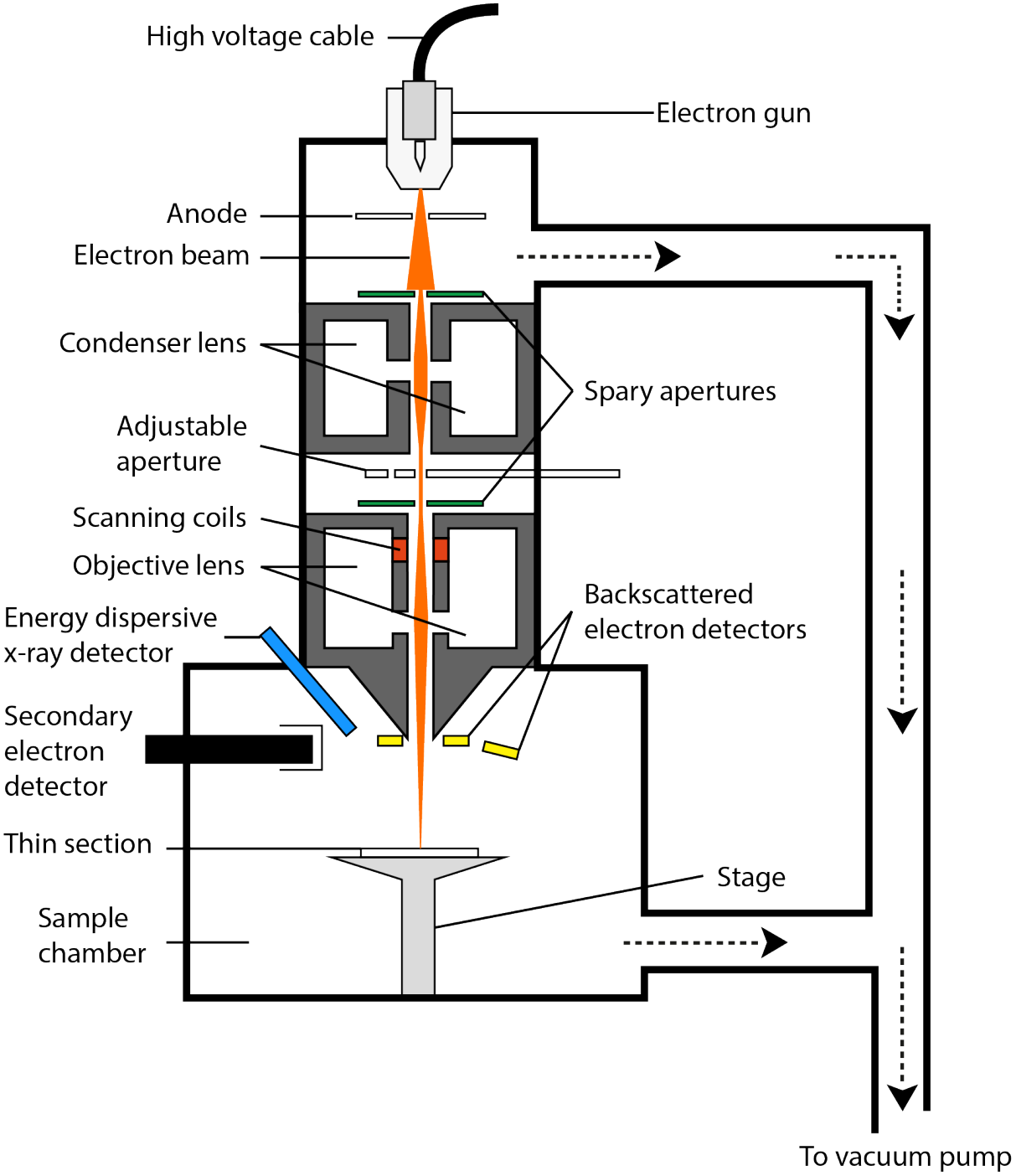

Figure 4.3: Simplified sketch of a Scanning Electron Microscope, modified after Wittke (2015), showing the main components. The microscope features an electron gun at the top, several lenses and apertures to control the electron beam, and a sample chamber. Vacuum pumps are applied to create vacuum in the sample chamber.

4.3 Image analysis

Images derived from the UAV and thin sections by light microscope and SEM are further processed using *Dronedeploy*, *Adobe Illustrator CC* and *ImageJ*. *Dronedeploy* is used for creating mosaics and large-scale figures of the studied area in map view. Photomicrographs derived from the thin sections are investigated and used for interpretation of the structures, e.g. fractures caused by the DB, in *Adobe Illustrator CC*. These pictures were also used for calculating the 2D macro-porosity in *ImageJ*, while pictures derived from BSE-SEM were used for 2D macro- and micro-porosity. At least 6 measurements were made within characteristic zones in each of the selected thin section (e.g. DB, transitional zone, host rock).

4.3.1 ImageJ porosity analysis of light microscope pictures

Photomicrographs derived from light microscope were acquired in color, with the pore space shown in clear blue due to the epoxy. This allows for determination of the Total Optical Porosity (TOP), i.e. 2D macroporosity. The estimations were performed by a set of two macros, developed by Niels Bo Jensen (University of Bergen). These macros were applied to provide a fast and efficient method of porosity estimations for the photomicrographs. The RGB images (Red, Green, Blue) are converted into HSB (Hue, Saturation, Brightness). Hue describes the attribute of pure color, thus distinguishing the colors. Saturation shows the purity or shade of the color, while brightness shows the overall brightness of the color (Ferreira and Rasband, 2012). The hue of the blue epoxy is selected from the rest of the color spectrum by setting its threshold color to red. Further, the threshold image is converted to black and white, and set to 8-bit to acquire a binary image for “particle” analysis. Automated measuring gives the total pore space area, and individual pore area size. The schematic flow chart showing the different steps in the analysis featuring photomicrographs are illustrated in Fig. 4.4.

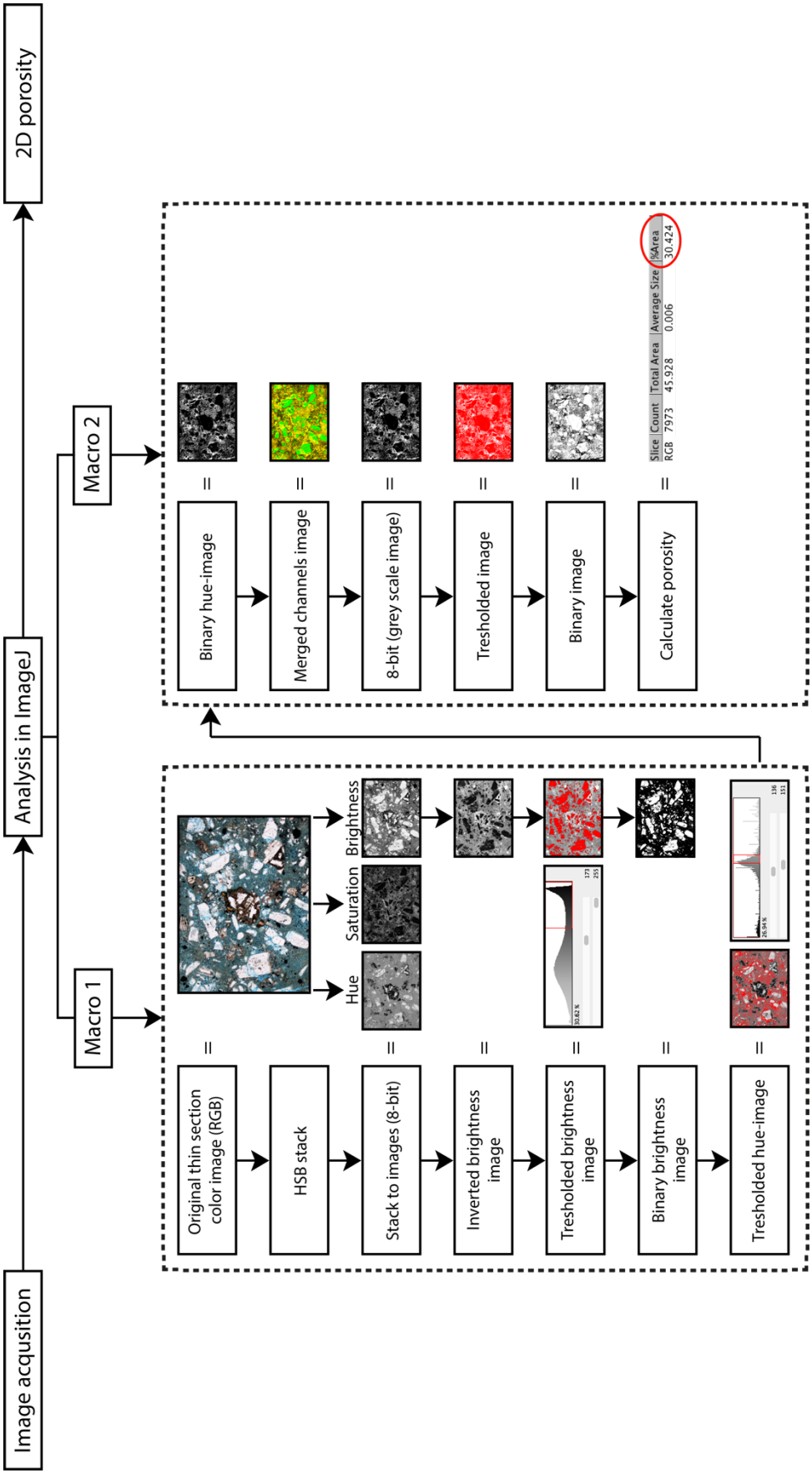

Figure 4.4: Schematic flow chart illustrating the steps performed in the digital image analysis of the microphotographs in ImageJ. The porosity is measured by pixel counting on a binary image, after several steps of thresholding has been applied. Modified after Thorsheim (2015).

4.3.2 ImageJ porosity analysis of BSE-SEM images

BSE-SEM images are used to measure the total porosity, as the micro-porosity is defined as the porosity that falls below the resolution of regular optical light microscope imagery (Dimmen et al., 2017).

The image analysis of the BSE-SEM images is quite similar to the photomicrographs, but fewer steps is needed to acquire the porosity estimations. Firstly, the images are converted to 8-bit, as they are initially acquired in greyscale. The threshold between shades of grey are adjusted to separate the pore space (black) from the mineral grains (grey). Further, the pixels within the threshold, i.e. pore space, are highlighted in red. The accuracy of this thresholding-process can be monitored by continuously comparing the image to the original BSE-SEM image. The thresholded image is then converted to a binary image, where the pore space appears black and the mineral grains are white. Pixel counting on the binary image allows for measurements of both 2D macro- and micro-porosity. The work flow is illustrated in Fig. 4.5.

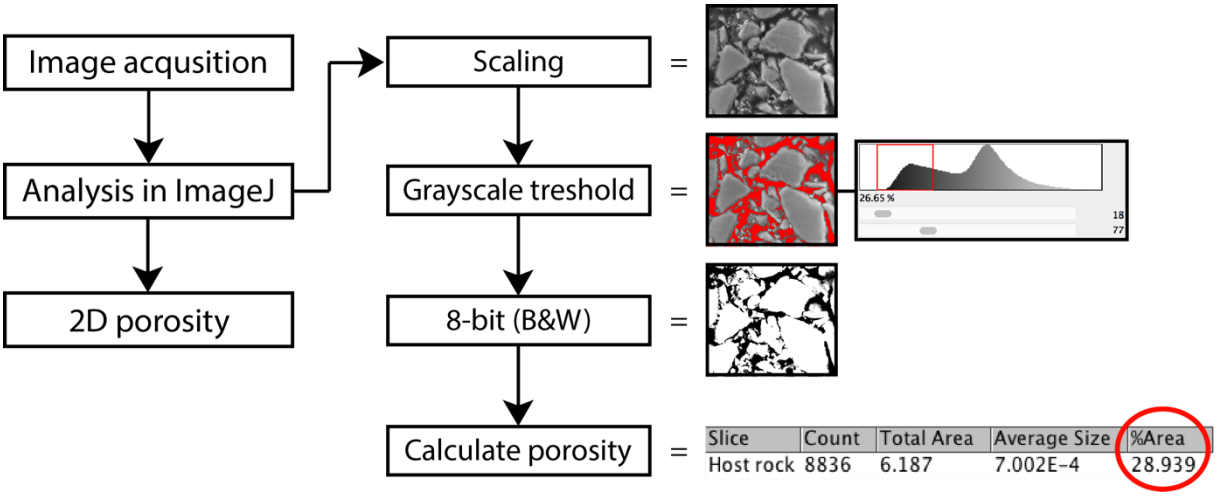

Figure 4.5: Schematic flowchart illustrating the steps performed in the digital image analysis of the BSE-SEM images in ImageJ for porosity measurements. Pixel counting on the binary image allows for measurements of 2D macro- and microporosity.

4.3.3 Uncertainties related to the image-based porosity analysis

Various limitations and possible sources of error occurs when 2D porosity estimations are performed. The thin sections provide a two-dimensional view of the pore space, in which the porosity estimations are based on the visible grain boundaries. However, this is not accurate since the pore space is in reality three-dimensional. Hence, mineral grains and adjoining pore space smaller than the thickness of the thin section may be excluded from the estimations (Fig. 4.6). Therefore, the porosity estimations are based on the principle that the porosity is recorded

at the top of the thin section, and the pore-grain boundary should be defined at the surface. The thickness of the sample that appears in focus has to be properly set when defining the latter boundary, in order to perform the estimations in the most accurate manner.

Other pitfalls that might occur during the analysis is porosity variations throughout the rock and within the thin section. Hence, the heterogeneity of the rock is a key factor. The rock samples gathered in the studied area appear homogeneous in hand specimens, but porosity variations are observed in the thin sections. Several photos were obtained from each thin section to counter and minimize this potential error.

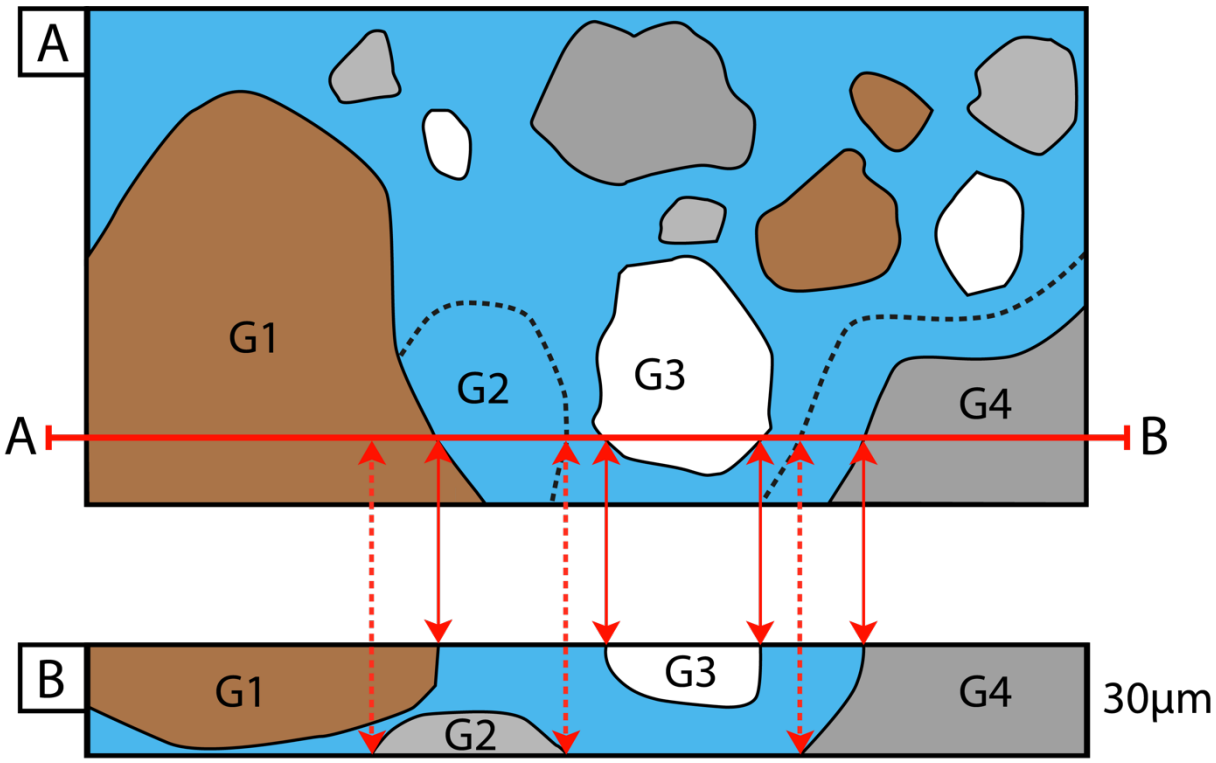

Figure 4.6: Schematic sketch of top- and cross-sectional view of a thin section. G: grain. Blue: epoxy. A) Top view of an imagined thin section. The grains G1, G3 and G4 are shown, while the dashed G2 indicate grain boundaries located deeper in the thin section. B) Cross sectional view of the thin section. All the grains are visible, as well as the pore space between them. G4 also show an irregular thickness. Modified after Thorsheim (2015).

5 Results

The purpose of this chapter is to present the field observations and microstructural analyses, as well as the porosity image-based measurements carried out on thin section from the studied area and deformation bands (DBs).

5.1 Host rock characterization

The studied lithology at Cuesta (Fig. 5.1) is composed of folded pyroclastic rocks and tuffs, which is previously described by Song and Lo (2002). Their classification is adopted in the descriptions herein; the volcaniclastic rocks observed in the studied area are therefore subdivided into the following lithologies:

i. Polygenic conglomerate
ii. Ignimbrites
iii. Tuffaceous sandstone

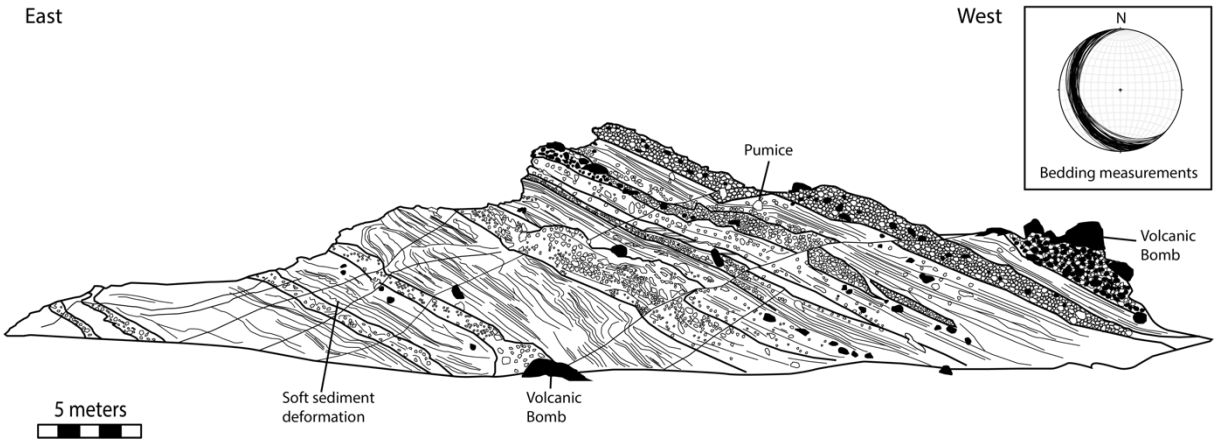

Figure 5.1: Illustration of the studied area. The Cuesta is shown as tilted layers of bedrock, with a long and gentle backslope on the western side. The volcaniclastic bedding have been measured to a mean strike/dip value of 158/26. Inspired by Cavailhes and Rotevatn (Submitted).

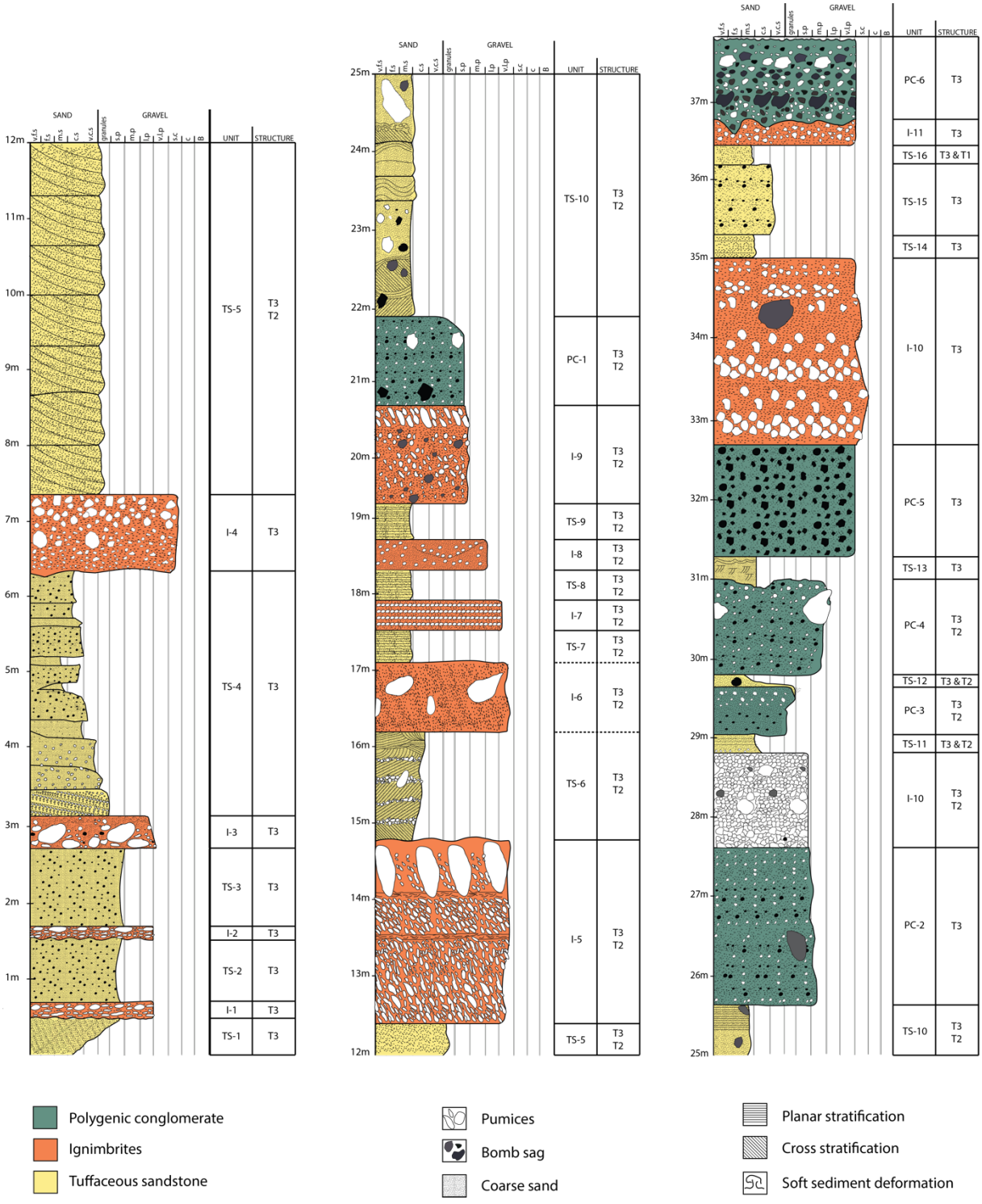

Figure 5.2: Stratigraphic log of the Shihtiping White Tuff member, based on field observations. The different lithologies are comprised of pyroclastic rocks and tuffs. The structure column indicates which type of DB is occurring in the given unit.

POLYGENIC CONGLOMERATES

Six distinct layers of polygenic conglomerates are found in the studied area. In general, the succession is appearing 1-2 meters-thick with almost exclusively large pyroclasts of bomb sags and pumices (Fig. 5.3). The clasts are mainly lapilli (32 to 64 millimeters), and angular to sub-

rounded. Volcanic bombs may occur locally (>64 millimeters). The breccia is mainly clast supported, with matrix of coarse graded tuffs.

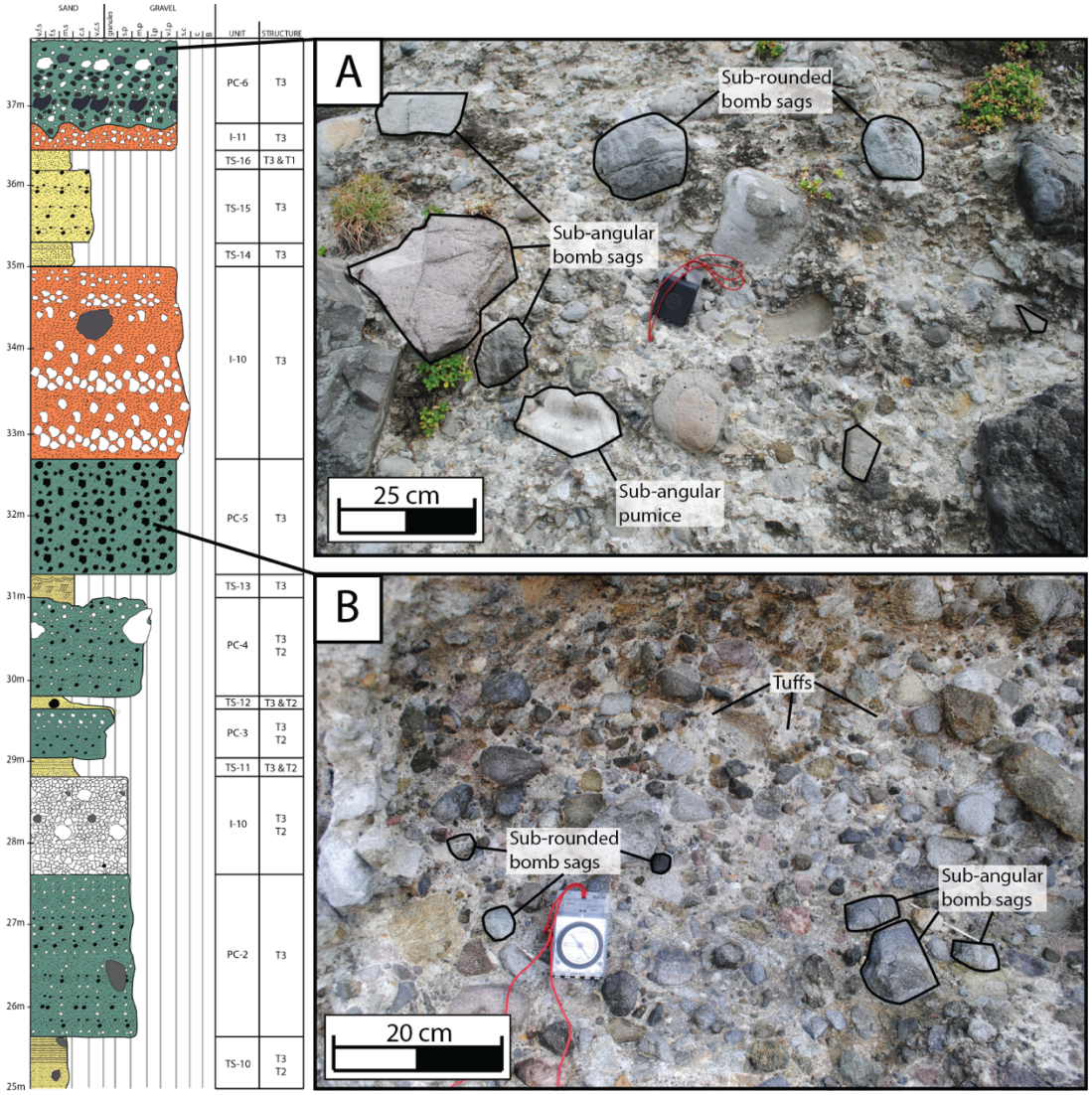

Figure 5. 3: Pictures showing the characteristics of polygenic volcanic breccia units. A) Representative picture from PC-6 unit. The pyroclastic rocks (bomb sags and pumice) appear sub-angular to sub-rounded. B) Shows a representative picture of the PB-1 unit.

IGNIMBRITES

The ignimbrite units are primarily comprised of pumices (mostly white, grey and sometimes reddish) with visible phenocrysts of hornblende and plagioclase (Fig. 5.4A). Some volcanic bombs may crop out locally. Thicknesses of the ignimbrite units ranges from tens of centimeters to several meters. The clasts are generally lapilli (4 to 64 millimeters), while some grain sizes up to blocks and bombs (>64 millimeters) may occur locally. The ignimbrite units (Fig. 5.4) are matrix supported by coarse graded tuffs. Some units are layered and exhibit imbricated

pumices (Fig. 5.4B). Some pumices crop out with eutaxitic texture, which is compaction or flattening of glass shards and pumice fragments (Fig. 5.4C).

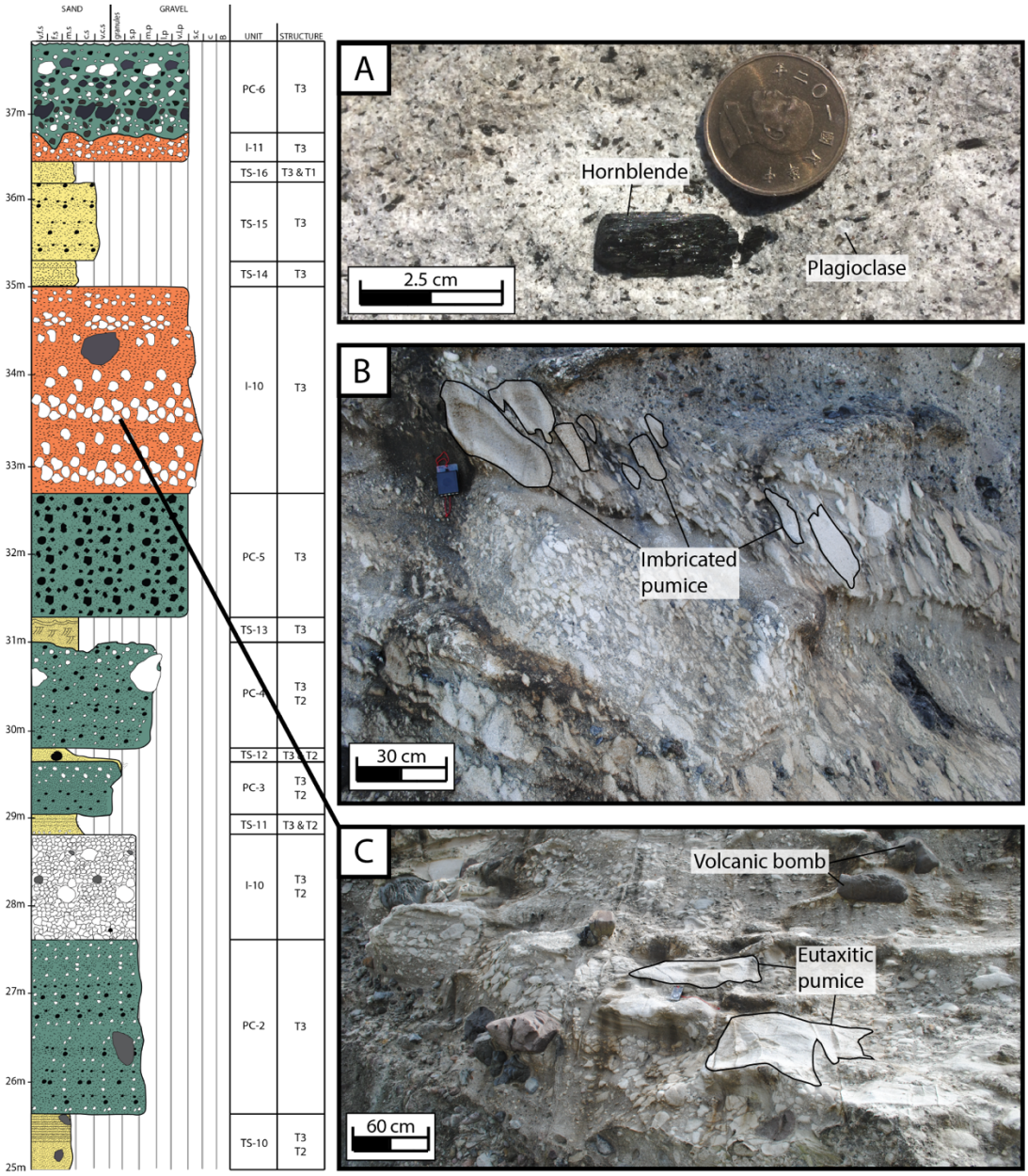

Figure 5.4: Field pictures showing examples from the ignimbrite units. A) Shows a representative picture of the pumices. Minerals are easily distinguished by hand lense. Picture acquired from Thibault Cavailhes. B) Imbricated pumices from unit I-5. C) Representative picture from I-10 unit. Both pyroclastic bombs (>256 mm) and ignimbrites with eutaxitic texture is present.

TUFFACEOUS SANDSTONES

The tuffaceous sandstone layers are the most abundant units at Cuesta, and was initially interpreted by Song and Lo (2002) to consist of crystal tuffs (tuffs herein) due to the abundance of magmatic mineral grains as well as lithic fragments. The units appear with a variety of

sedimentary structures, including planar stratification (Fig. 5.5A), herringbone cross-bedding stratification (Fig. 5.B), hummocky stratification (Fig. 5.5A) and soft sediment deformation features (Fig. 5.5C). The thickness of the tuffaceous sandstone varies laterally as it pinches out in two of the units (TS-4 and TS-12, Fig. 5.2). The tuffaceous sandstone units are supported by a matrix of very fine (0.06 to 0.125 millimeters) to very coarse ash (1 to 2 millimeters).

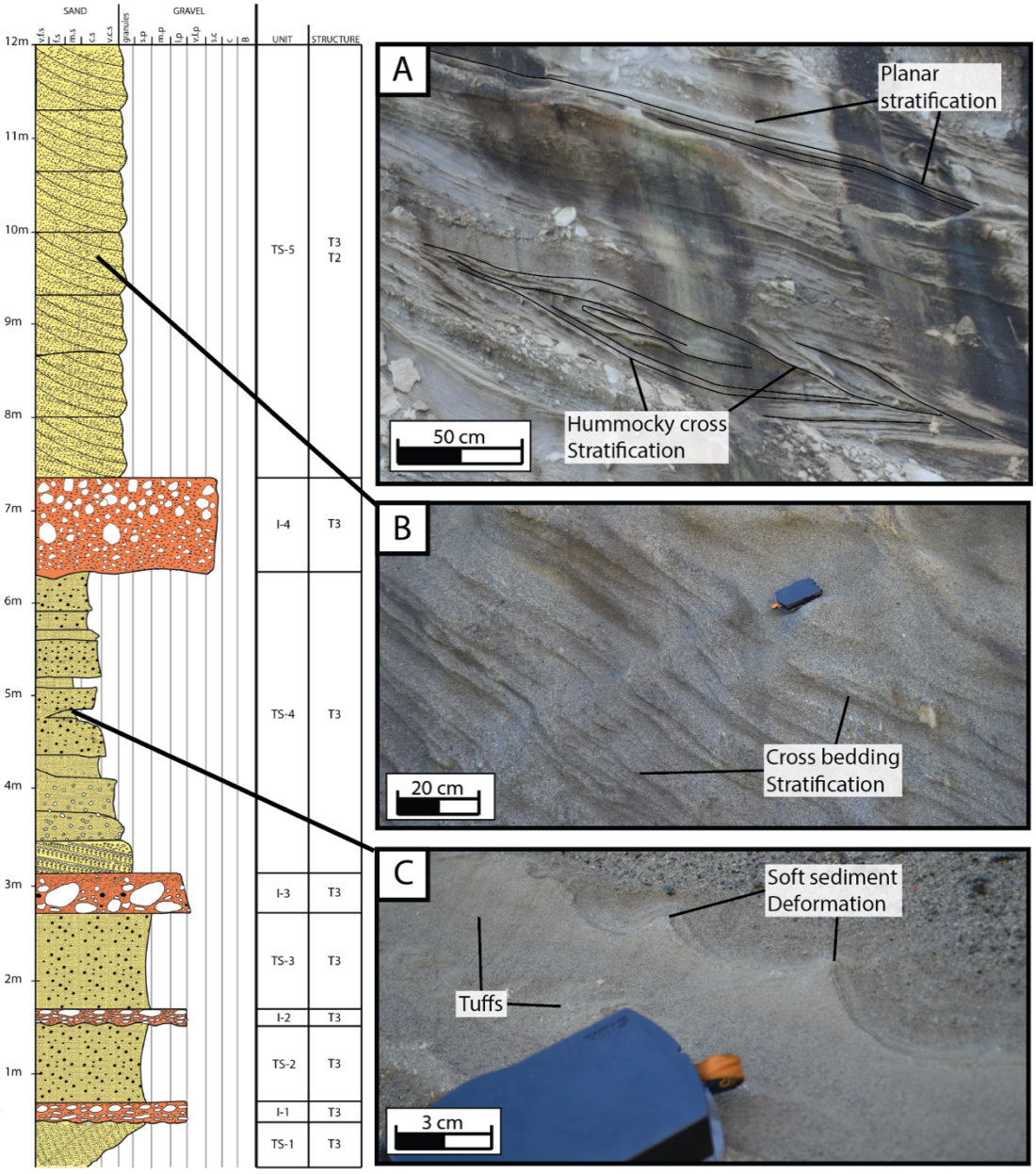

Figure 5.5: Generalized representation of the tuffaceous sandstone. A) Field photo from unit TS-10, showing both the hummocky cross stratification and the planar stratification. B) Field photo visualizing the cross-bedding stratification, observed in unit TS-5. C) Field photo showing the soft sedimentation deformation, as well as the tuffs in TS-4.

MICROSTRUCTURAL CHARACTERIZATION OF THE HOST ROCKS

The various subunits illustrated in the schematic log (Fig. 5.2) exhibit identical mineral assemblage, even though they appear visually different in the field. Generally, five different minerals have been identified in the microscopic analyses of the host rocks, which corresponds to findings by Song and Lo (2002) (in decreasing proportion): Plagioclase, hornblende (amphibole), hypersthene (orthopyroxene), augite (clinopyroxene) and magnetite (iron-oxide). In Fig. 5.6, these minerals are presented with euhedral to subhedral crystal shape, while the majority of the mineral grains in the thin sections appear either fractured or deformed. In addition, lithic fragments and volcanic glass are observed. The lithic fragments consist of the same mineralogy as that of the surrounding host rock. The mineral grains vary in size, from 0.03 to 3 millimeters.

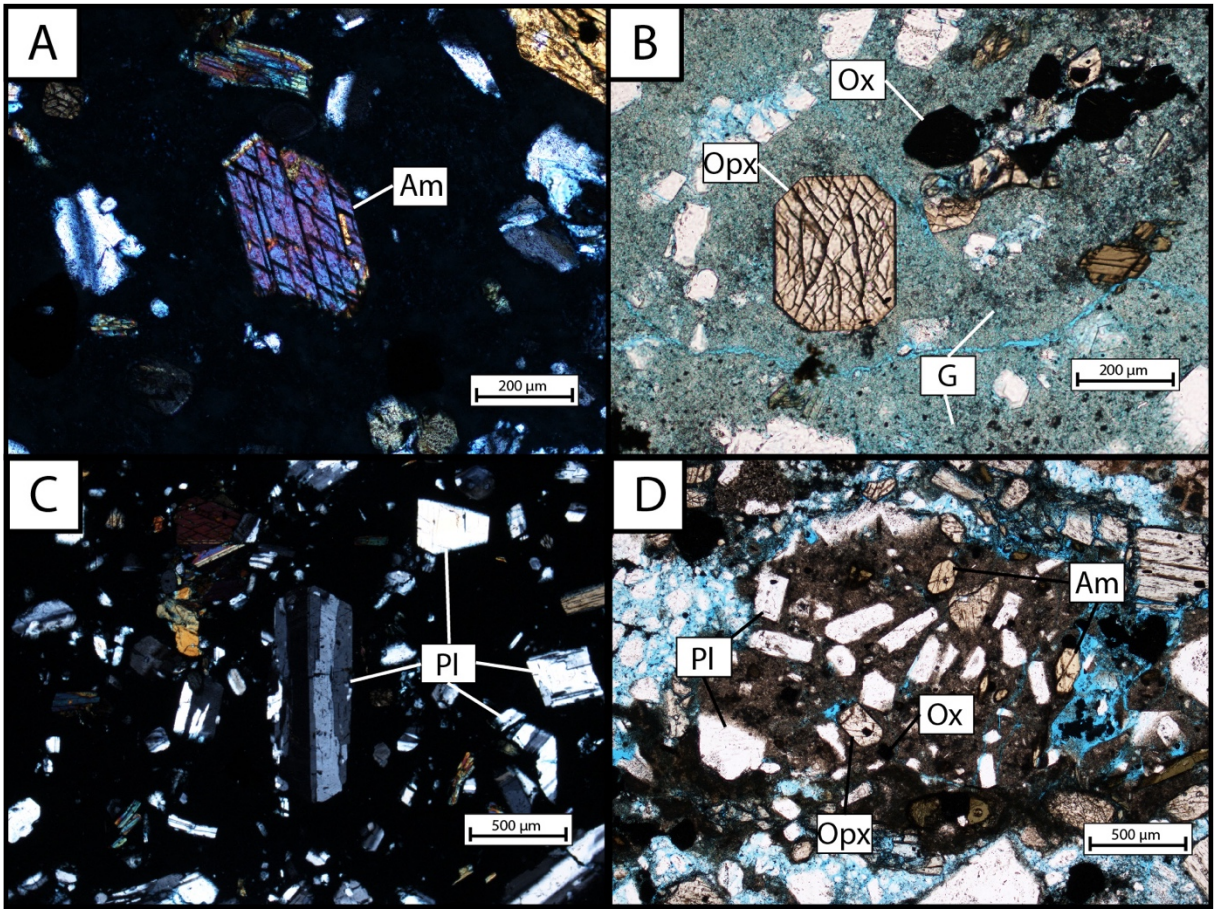

Figure 5.6: Pictures derived from light microscope. A) Shows a euhedral hornblende (Am) in XPL. B) Hypersthene (Opx) and magnetite (Ox) incorporated in volcanic glass (G), which is the greenish matrix observed. Viewed in PPL. C) Image showcasing plagioclase minerals (Pl). D) Picture of a lithic fragment. The fragment contains various minerals; plagioclase (Pl), hypersthene (Opx), magnetite (Ox) and hornblende (Am). The blue colored zones (blue epoxy) indicate free pore space.

The minerals appear with various magmatic textures and properties, even though the volcaniclastic host rocks fall between sedimentary- and igneous. The plagioclase minerals occur with mainly oscillatory zoning (Fig. 5.7A), but a minor amount is observed with continuously zoning (Fig. 5.7B). Some lithic grains exhibit radiate structures, in which elongated minerals diverge from a common nucleus (Fig. 5.7C). The mineral grains are either enclosed in volcanic glass (Fig 5.6D) or situated in free pore space (Fig. 5.6B). Different mineral relation contacts are observed in the thin sections, e.g. flat contact (Fig. 5.6A) and point contact (Fig. 5.6B).

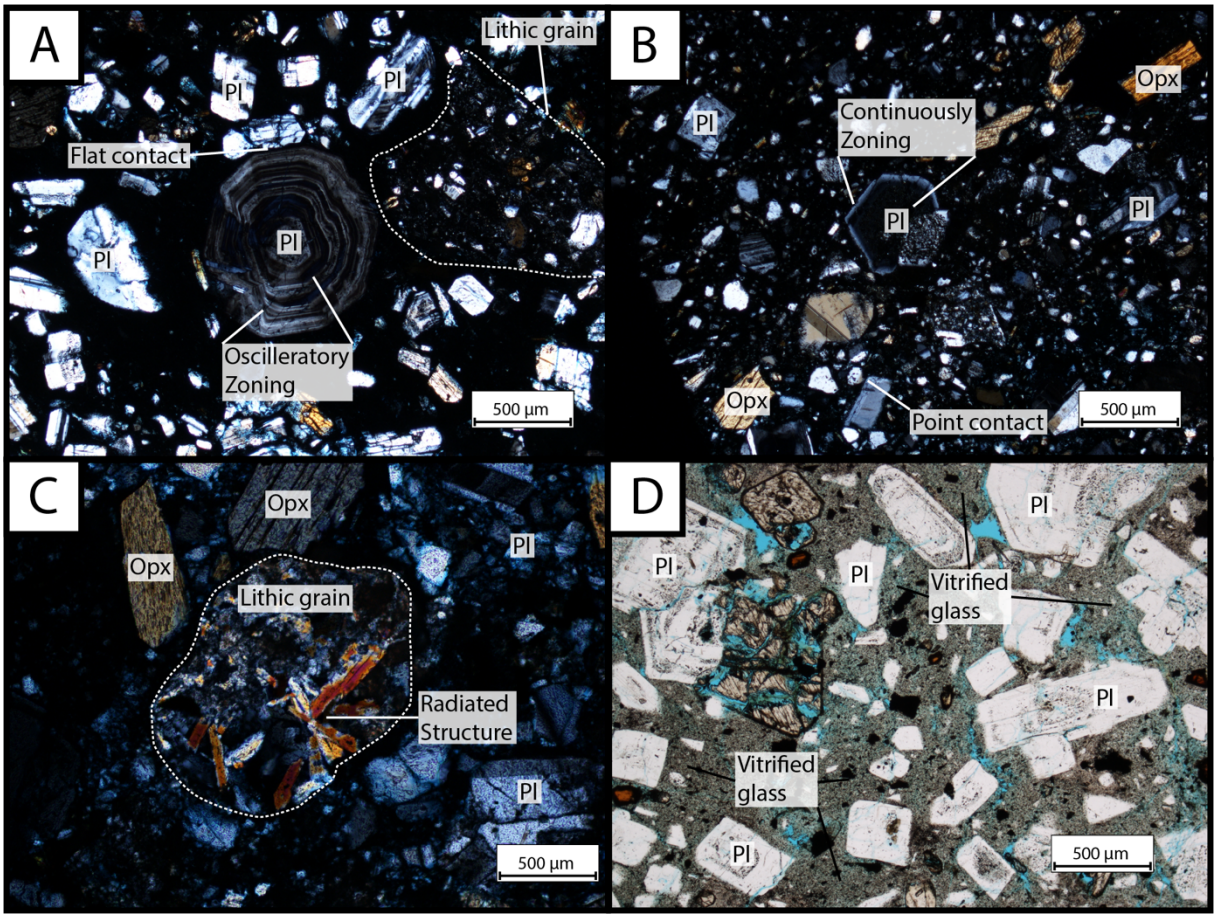

Figure 5.7: The minerals appear with different magmatic textures and grain contacts. A) Many plagioclase minerals are observed with oscillatory zoning. B) Image showing a plagioclase with continuously zoning. C) The minerals in the lithic fragments may appear with radiated structures. D) Minerals are situated in vitrified volcanic glass. Picture acquired from volcanic bomb.

5.2 Characterization of the studied deformation bands

The studied DBs are described and classified (following Aydin et al., 2006; Fossen et al., 2007) on the basis of: i) occurrence in the stratigraphy and orientation relative to bedding, ii) presence/absence of shear displacement, iii) porosity contrast to host rock, and iv) dominant deformation mechanism. The evidence is presented in the following subchapters, where the DBs are subdivided into three types.

5.2.1 Type 1

The DBs classified as type 1 appear as singular (rarely interacting) strands, which forms slightly elevated reliefs in terms of millimeter high ridges (Fig. 5.8A and C). These observable reliefs reflect a higher resistance to weathering compared to the host rock and make the DBs easy to distinguish from the surrounding volcaniclastic rocks. However, the type 1 DBs crop out only in the uppermost layer of tuffaceous sandstone, as expressed in the stratigraphic log (Fig. 5.2). The type 1 DB is cross cut by type 3, as shown by Fig. 5.8D.

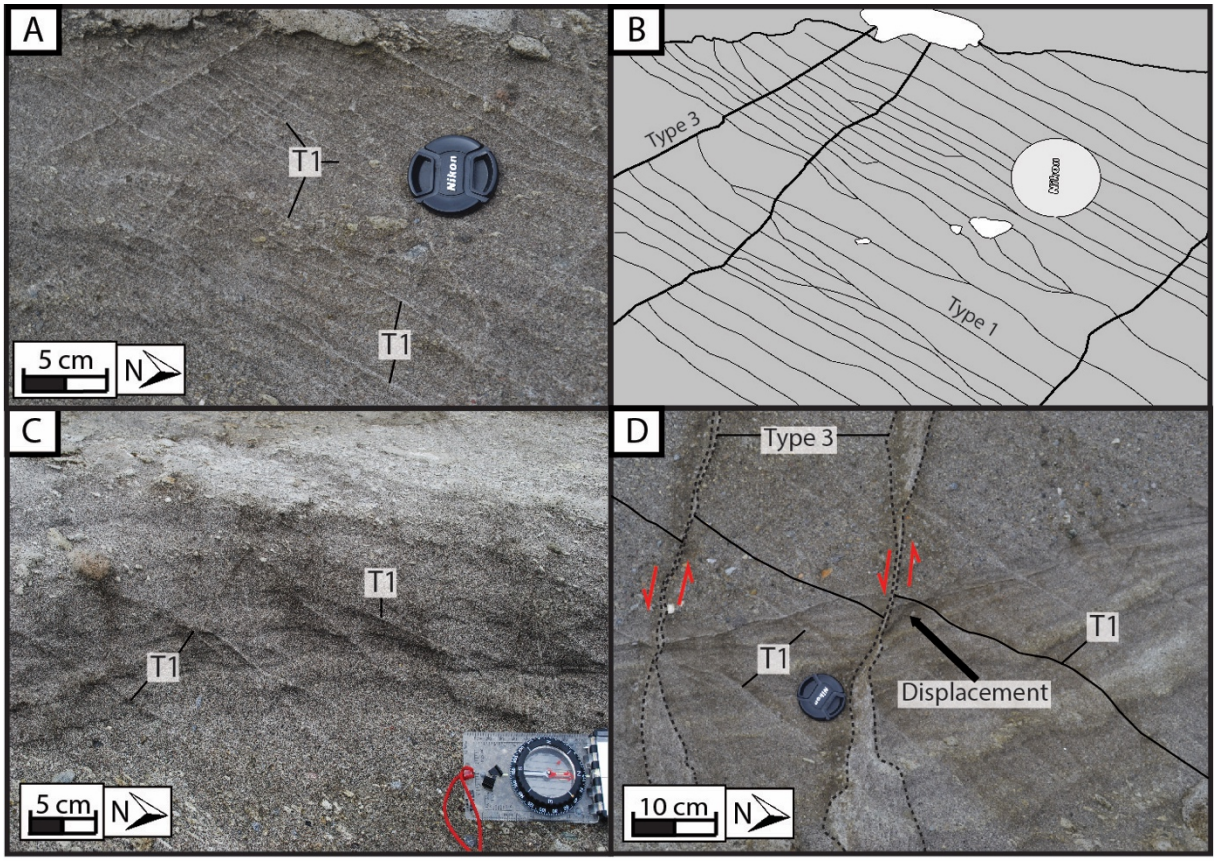

Figure 5.8: Field pictures and line sketches illustrating the type 1 DB as observed in the studied area. A) Picture of the individual strands in medium-grained tuffaceous sandstone. B) Line sketch comparison of the latter picture. The presence of type 3 DB is presented by a thicker stroke. C) Field picture from a medium to coarse-grained tuffaceous sandstone. D) Field picture showing the interaction and cross cutting relationships between the type 1 and type 3 DB. The type 1 is displaced by type 3.

The individual strands typically range in thickness from 2-8 millimeters, but are more consistent in thickness within individual localities around the studied area. At location 1-1-A (Fig. 5.9A), the type 1 DB appear with a mean thickness value of 1.6 millimeters, while at location 1-2-A (Fig. 5.9B) they appear with a mean value of 5.5 millimeters (Fig. 5.10). The frequency of strands varies between different areas at the outcrop. Locality 1-1-A shows an average spacing of 5.4 centimeters, while locality 1-2-A appear with an average spacing of 11.2 centimeters.

Generally, the type 1 DB in the tuffaceous sandstone exhibit a high dip compared to the folded bedding, ranging from 50-80° (Fig 5.9A). A similar orientation of the bands is seen in Fig. 5.9B, gathered from strike-dip values from locality 1-2-A.

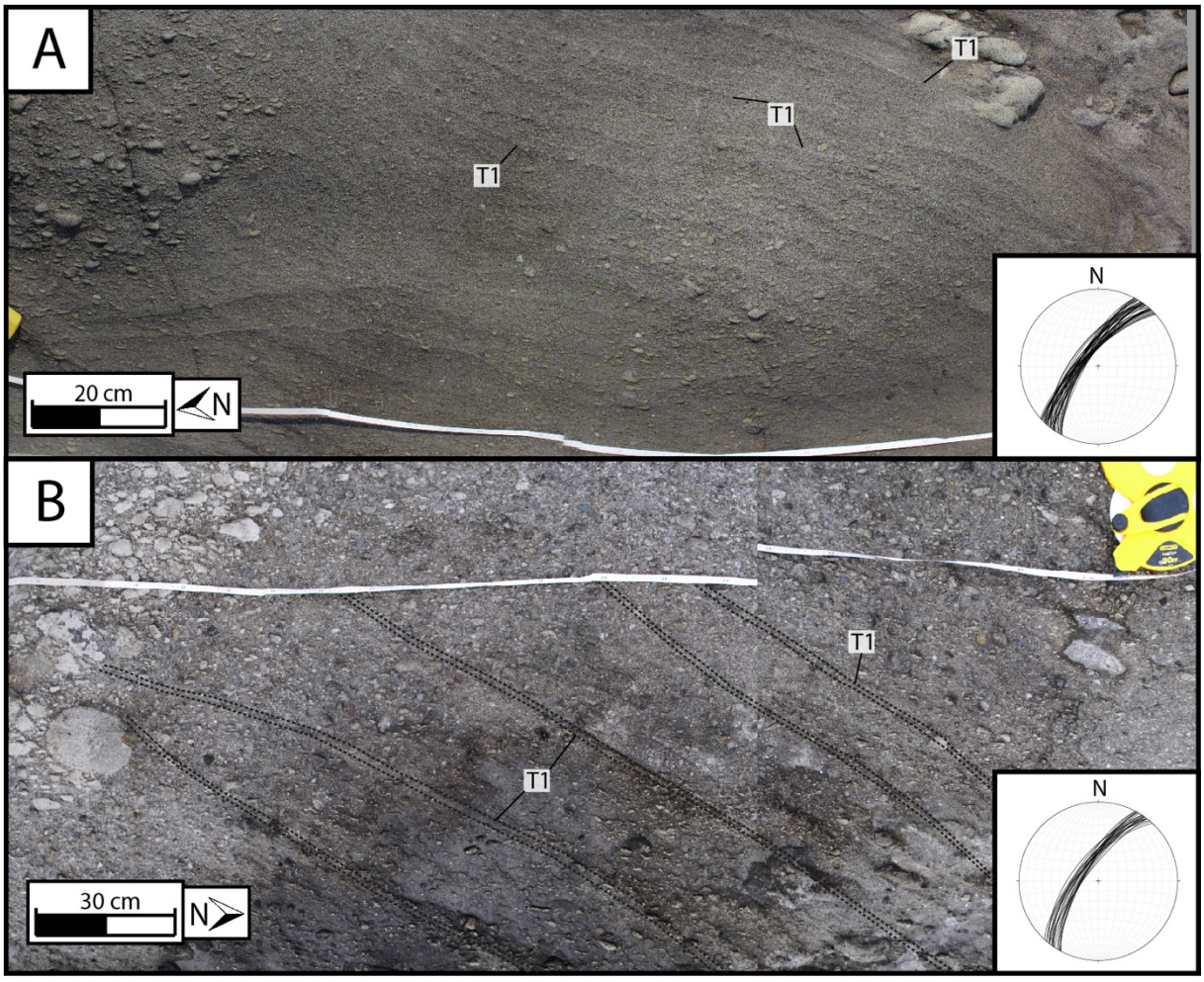

Figure 5.9: Field pictures showing the two meso localities of type 1 DBs; in medium and coarse-graded tuffaceous sandstone, respectively. A) Field picture of locality 1-1-A. The type 1 DBs are observed as distinct lines. The mean strike/dip value is 210/68. B) Field picture of locality 1-2-A in a coarser section of the tuffaceous sandstone. The mean strike/dip value is 214/71.

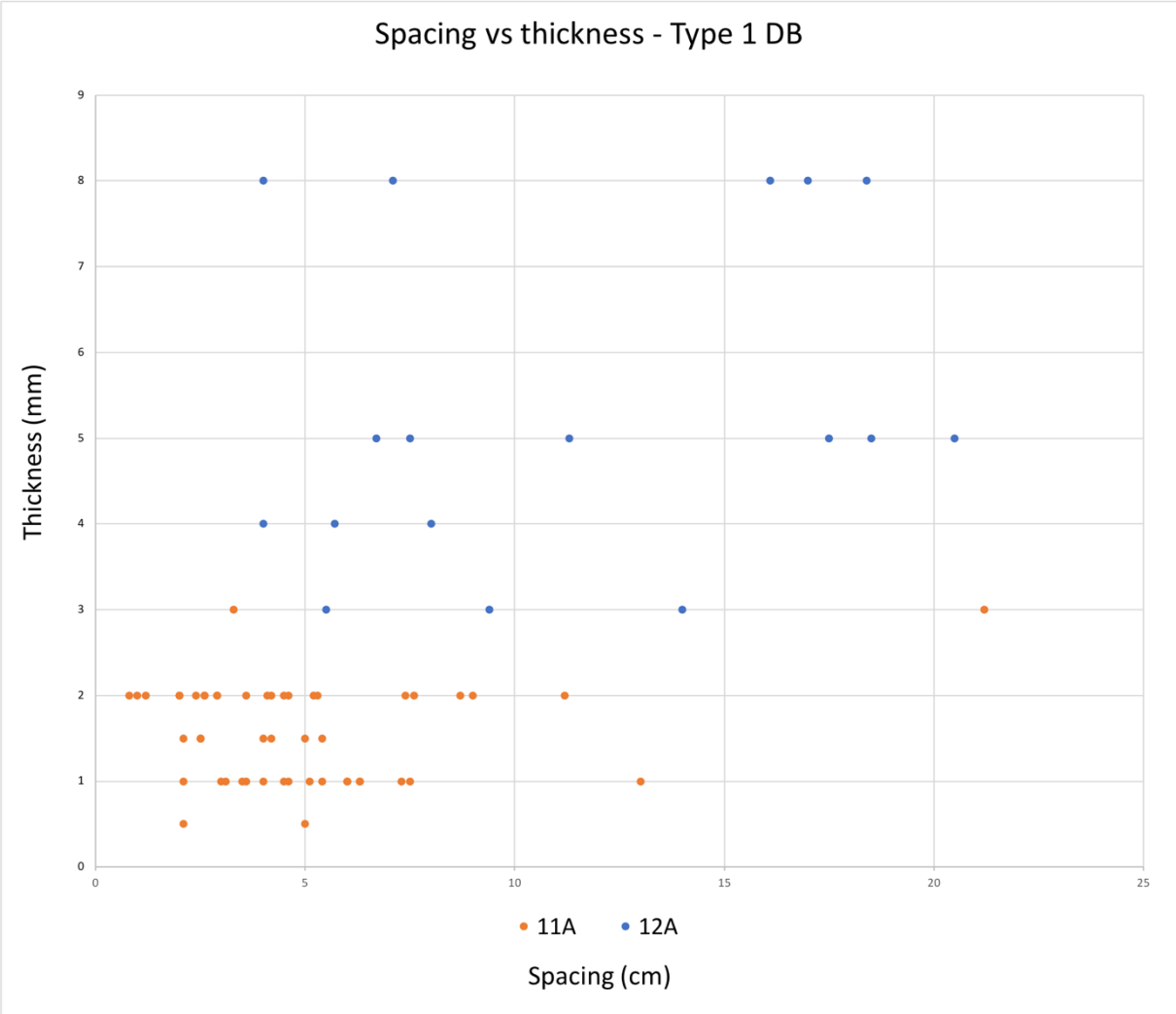

Figure 5.10: Crossplott between thickness and spacing measurements for the type 1 DB. Locality 1-1-A shows relative narrow thickness values between 1 to 3 millimeters, while locality 1-2-A shows thickness from 2.5 to 20 millimeters.

The type 1 DB does not appear with any evidence of shear movement in the field. Further investigations by light microscope and BSE-SEM analyses support these observations. The texture consists of slightly more compressed mineral grains with no visible comminution. The minerals within the DBs are oriented parallel to the band by their most prominent crystallographic axis, e.g. c-axis for orthopyroxene (Fig. 5.11). Type 1 DBs are recognized in light microscope by loss of pore space compared to the surrounding host rock, as illustrated by the blue epoxy in Fig. 5.11.

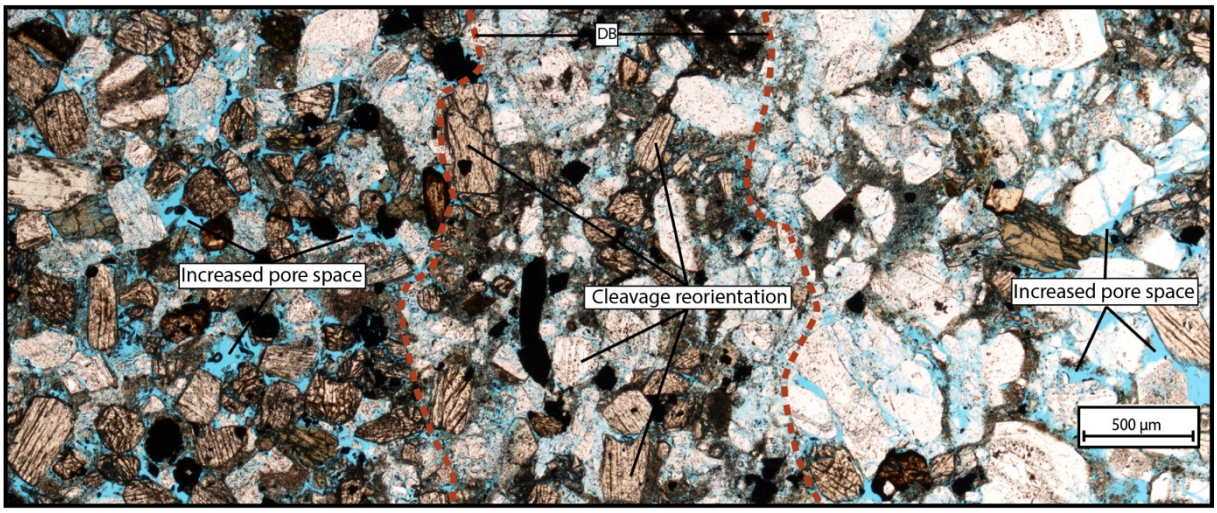

Figure 5.11: Light microscope picture in PPL of the type 1 DB, highlighting pore space loss and mineral reorientation. The red dashed line indicates the boundaries of the DB. Pyroxene minerals are reoriented parallel to the DB by their most prominent cleavage plane (i.e. crystallographic axis).

Total porosity measurements were carried out to document any porosity changes associated with the bands. The lowest porosity measured for the host rock (tuffaceous sandstone) is 16.0% and the highest 33.7%, with an overall average of 27.2% (Fig. 5.12). The sample provides porosity measurements that ranges from 15.0% to 21.7% within the band, with an overall average of 17.9%.

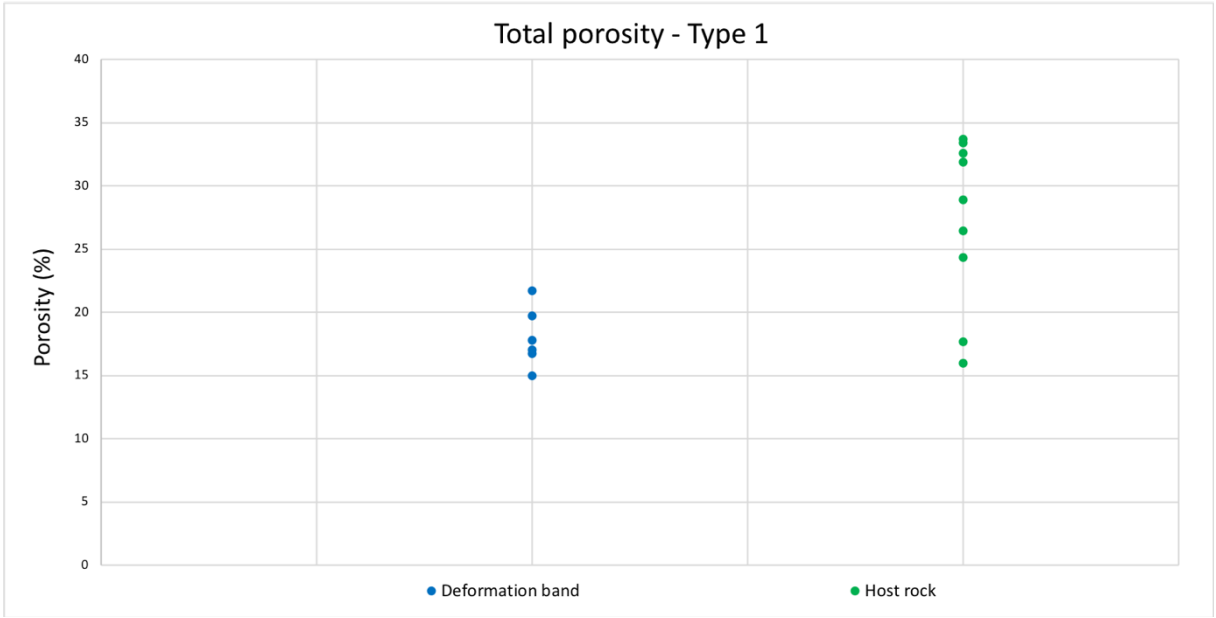

Figure 5.12: Total optical porosities calculated for the sampled type 1 DB. No apparent transitional zone were observed during the microstructural investigations of the bands.

5.2.2 Type 2

The type 2 DB appear as a denser set of DBs, which exhibit an overall geometry of a flat-ramp-flat thrust system (5.13A and B), and is further divided into three distinctive segment types: flat-segment, back-thrust, and ramp-thrust. These strands crop out as dark grey with distinct reliefs, or, as in the case of the flat-segments, as striated planes (Fig. 5.13C). The flat-segments and ramp-thrusts are observed in both the ignimbrites and tuffaceous sandstone units, while the back-thrusts only appear in the fine-graded tuffaceous sandstone. The type 2 DBs are cross cut by type 3 DB in the studied succession (Fig. 5.13D).

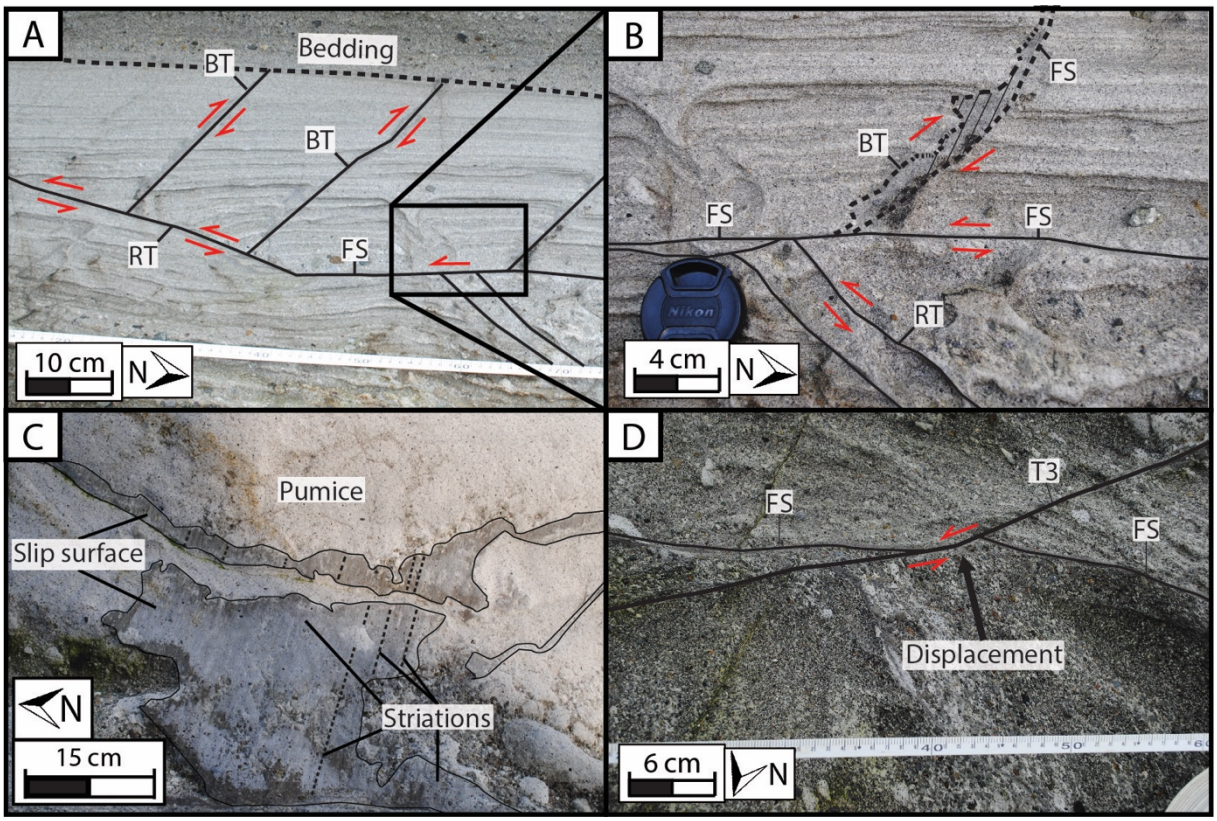

Figure 5.13: Field pictures and line sketches illustrating the type 2 DB in the Shihtiping White Tuff. These bands include denser conjugated sets of strands, which is represented in the figure. A) Field picture and Line sketch of the complete set of type 2 DB. B) Line sketch of all the segments and most notably the back-thrust, which develops along the flat-segment. The back-thrust appear with striations, and the thrust displacement are measured to be 1 centimeter. C) Field picture showing the striated surfaces of the flat-segment. D) Cross cutting relations between the type 2 and type 3 DB.

The flat-segments and the ramp-thrusts of the type 2 DBs at Cuesta typically ranges from 2 to 4 millimeters in thickness, while the back-thrusts are thinner with a mean thickness of 0.5 millimeter (Fig. 5.14). The flat-segment crop out subparallel with the bedding with similar low-angle dip (20-30°), while the ramp-thrust and back-thrust segments appear at a steeper dip (40-50°). As aforementioned, the three segments of type 2 DB are bound to layers (Fig. 5.15A), and

do not always crop out as a complete set. The flat-segment and ramp-thrust are most abundant, as it crops out without the back-thrust. The type 2 DBs thrusts both pumices and stratified tuffaceous sandstone, as shown in Fig. 5.15B. However, the offset varies between the three strand types (Fig. 5.14). The flat-segment displays the highest displacement, where the ramp-thrust and back-thrusts follows, respectively. Also, the type 2 DBs displays striated surfaces (i.e. slip surfaces) with clear evidence of grain crushing, which is most prominent in the flat-segments (Fig 5.15C). The slip surfaces exhibit a darker color than the host rock, which is pumice for Fig. 5.16. In addition, smaller mineral grains from the host rock are recognized within the flat-segment, thus indicating comminution.

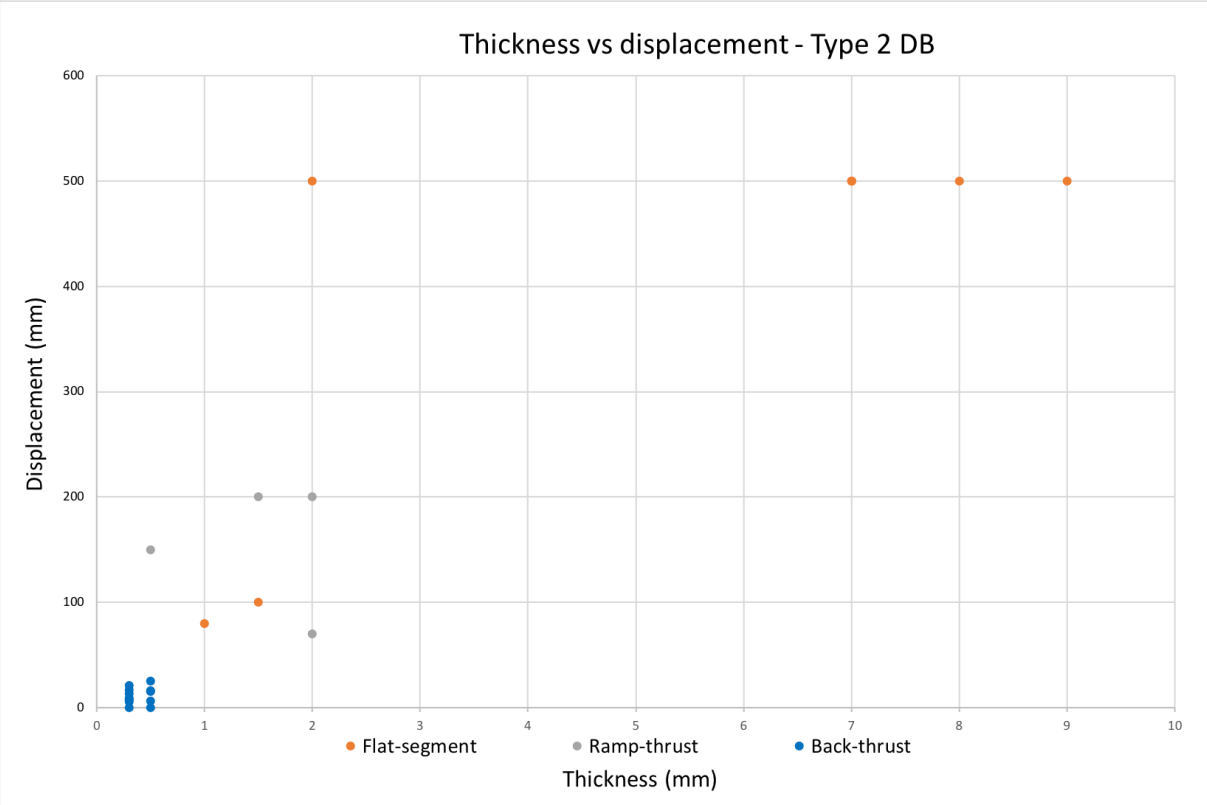

Figure 5.14: Crossplott between thickness and displacement measurements of the type 2 DB for each component. Observed displacement caused by the DB is plotted against thickness. The flat-segment appear with the highest displacement, and back-thrust with the lowest.

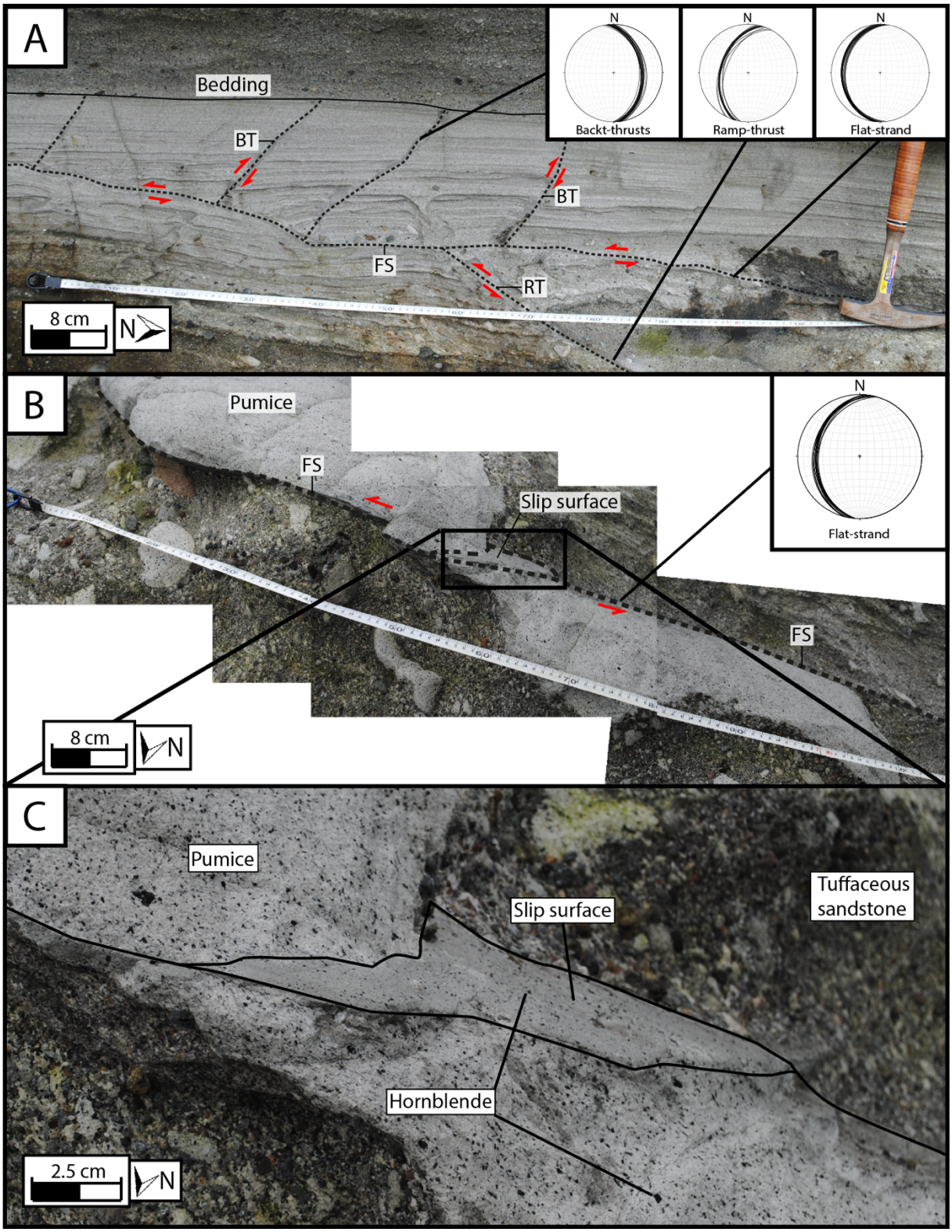

Figure 5.15: Field photo of the type 2 DB localities illustrating the displacement and the strike/dip measurements accordingly. A) Picture represents locality 2-1-A. All three 3 components of the type 2 DB are presented, in addition with their strike/dip measurements. The offset of back-thrusts is measured to a mean value of 1,1 centimeters. B) Field photo illustrating locality 2-2-A. Only the flat-segment is observed at this locality. Total displacement is measured to be 50 centimeters. C) Zoomed in field photo of the flat-segment, highlighting the slip surface. Comminution of mineral grains are observed between the host rock and the DB.

The shear displacement of the type 2 DB is further investigated in thin sections. The flat-segment has been the focus of the following analysis, due to more abundant sampling in the field. The flat-segment appear as thick, distinct brown lines/areas in light microscope, with an abrupt boundary (sharp transition) to the host rock (Fig. 5.16A). Black minerals (presumably iron oxides) are found along the boundary of the DB. In addition, the overall grain size within the DB is smaller (Fig. 5.17) than the host rock, suggesting grain comminution. However, lesser comminuted mineral grains are rotated parallel to the main direction of shear by their prominent crystallographic axis (i.e. cleavage plane) (Fig. 5.16B). Notably, volcanic glass fragments visible in BSE-SEM (Fig. 5.16C) appear less comminuted than mineral grains within the DB compared to the host rock.

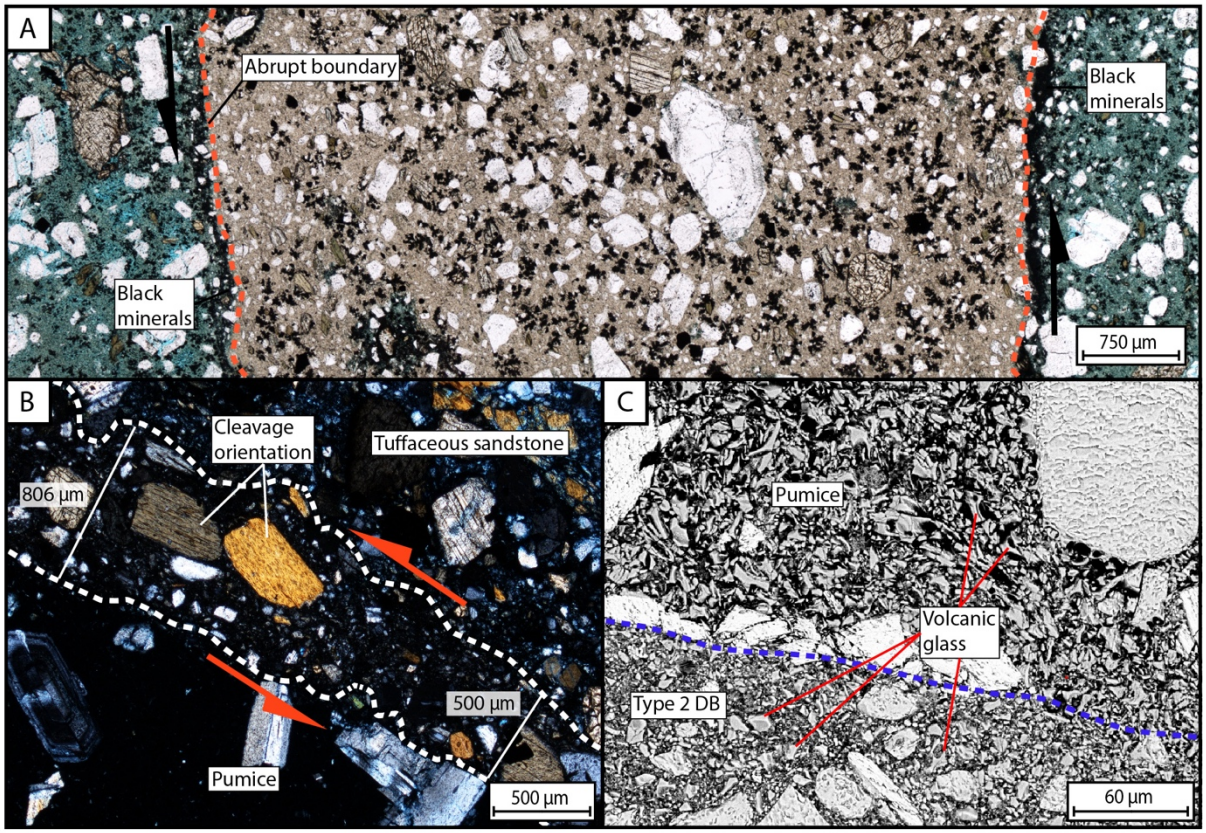

Figure 5.16: Light microscope picture of the flat-segment component in type 2 DB. A) Picture of the type 2 DB in PPL, showcasing the thickness of the flat-segment in pumice from locality 2-2-A. The boundaries between the host rock and the DB is abrupt and may feature alteration adjacent to the boundary. B) Picture in PPL showing the boundaries between pumice and tuffs. Larger mineral grains are reoriented parallel to the main direction of shear. C) Picture from BSE-SEM showing the abundance of volcanic glass fragments within the DB. The fragments appear to be included within the DB rather than comminuted.

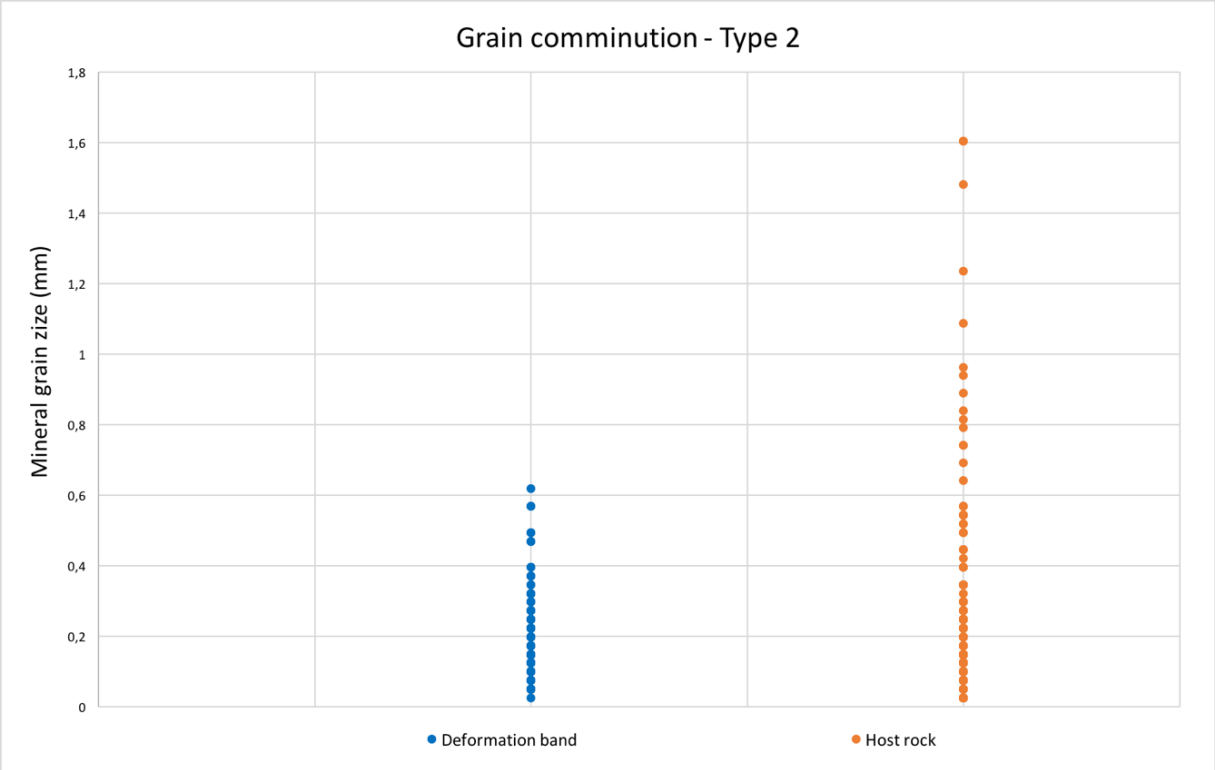

Figure 5.17: Mineral grain size measurements from DB and respective host rock. The type 2 bands appear abrupt in thin section, hence mineral grains in the transitional zone are not measured.

The principal direction of shear can be defined in the type 2 DB by kinematic indicators, e.g. mineral drag. These are disrupted grain contacts that occur along the boundary between host rock and the DB. This is shown in Fig 5.18, where an amphibole is prone to fracturing and comminution. Mineral fragments from the amphibole are dragged and incorporated into the DB. Notably, minerals are prone to fracturing both parallel and perpendicular to the most prominent cleavage planes. The fractures are affected by extensional- (T-fracture) and shear displacement (P-shear fracture) (Fig. 5.18B).

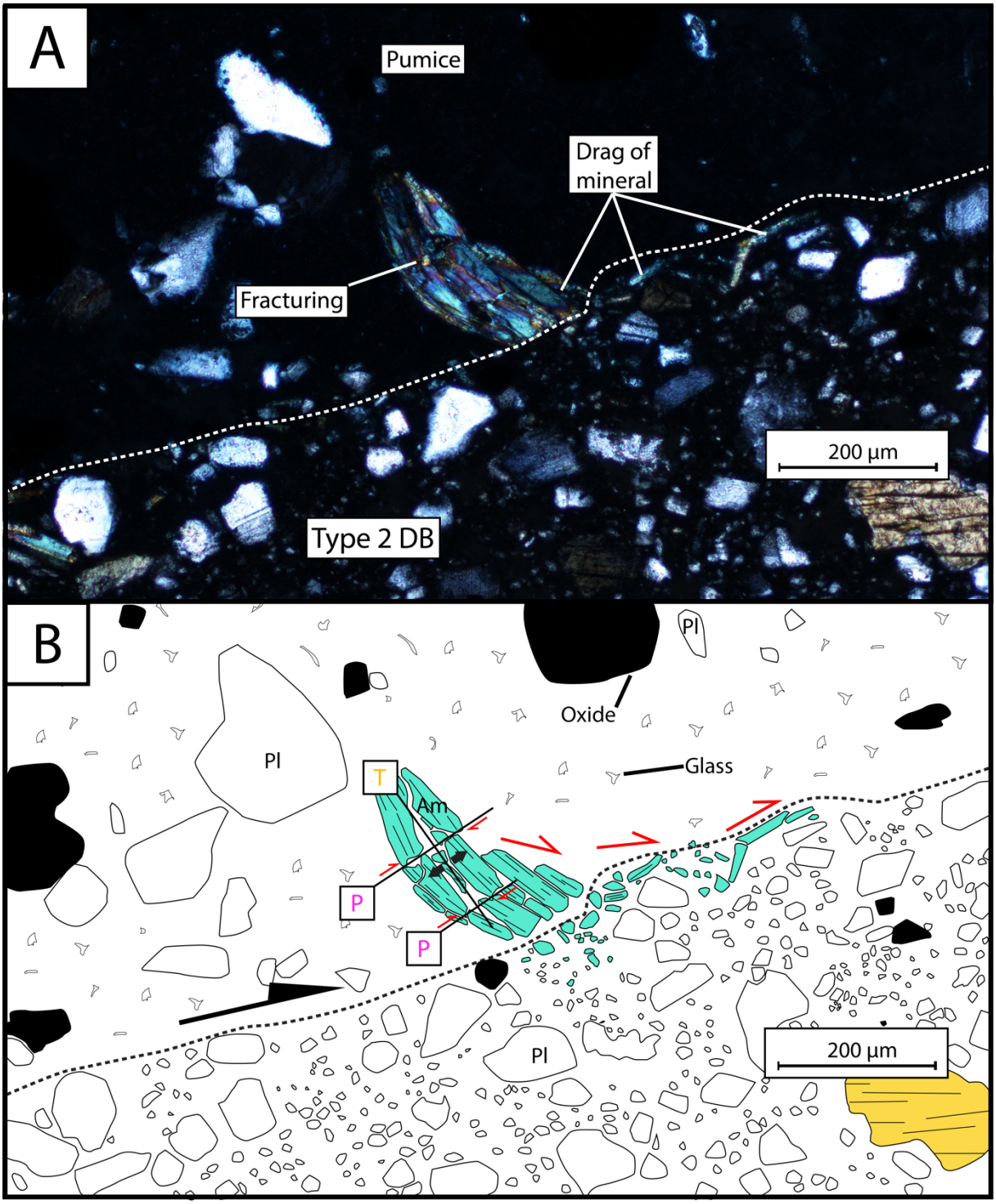

Figure 5.18: Mineral drag as a disrupted grain contact in a type 2 DB. Amphibole (Am) (green) is fractured and dragged along the DB boundary. In addition, grain comminution is visible as the DB contains smaller grain fragments than the host rock. A) Representative light microscopic picture from sample 22A-2A, which features type 2 DB in pumice. B) Sketch illustrating the features of the dragged mineral. The mineral is prone to P-fractures and T-fractures. Am: Amphibole, Pl: plagioclase.

Severely fractured minerals adjacent to the DBs may be used as kinematic indicators based on the Riedel shear fracture geometry. This is shown in an orthopyroxene mineral in Fig. 5.19. Synthetic fracturing (P-fractures) occurs parallel to the cleavage plane, while antithetic (R'-

fractures) appear perpendicular. Notably, the orthopyroxene is reoriented parallel to the DB by its most prominent cleavage plane (Fig. 5.19).

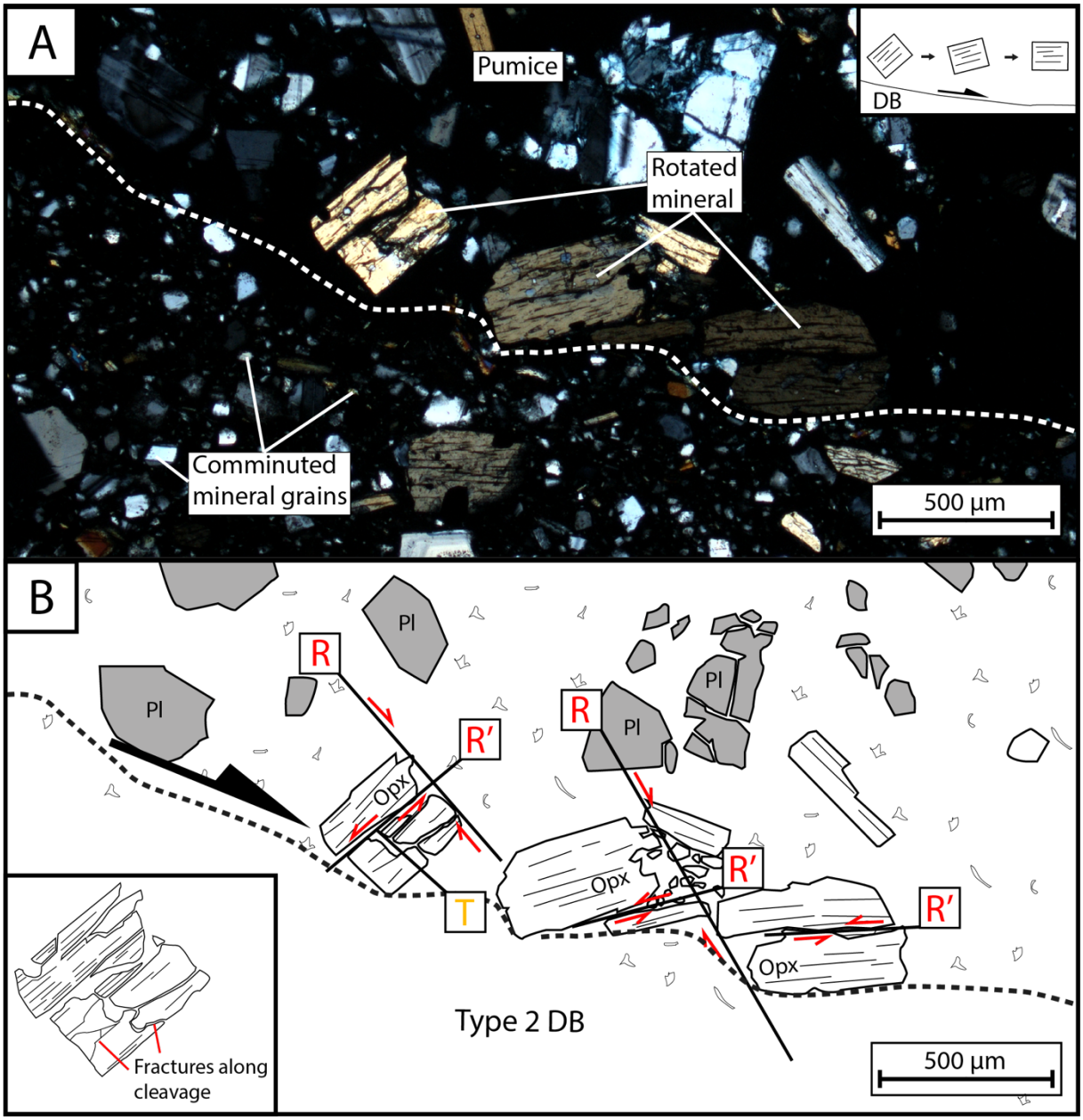

Figure 5.19: Fractured mineral grains along the boundary of a type 2 DB. A) Light microscopy picture of the DB and the fractured orthopyroxene (Opx). The picture is acquired from sample 22A-1B. B) Line sketch of the former, focusing on the fractures. Riedel fractures (R) occurs parallel to the cleavage, while the R'-fractures occurs perpendicular. Opx: orthopyroxene, Pl: plagioclase. Notably, fractures occur parallel and perpendicular to the cleavage.

Porosity measurements are conducted to document any porosity loss (or gain) associated with compaction (or dilation) and the observed grain comminution (Fig. 5.20). The analyses of the type 2 DBs are conducted in contrast to the porosity in the ignimbrite succession (mainly pumices and tuffaceous sandstone). The pumices exhibit a mean porosity value of 25.8%, while

the tuffaceous sandstone exhibits 30.2%. Porosity measurements from the type 2 DBs yields values in the range from 10.0% to 17.5% within the band, with an overall average of 13.2%. The transitional zone between the host rock and the DB display an average porosity of 19.2%.

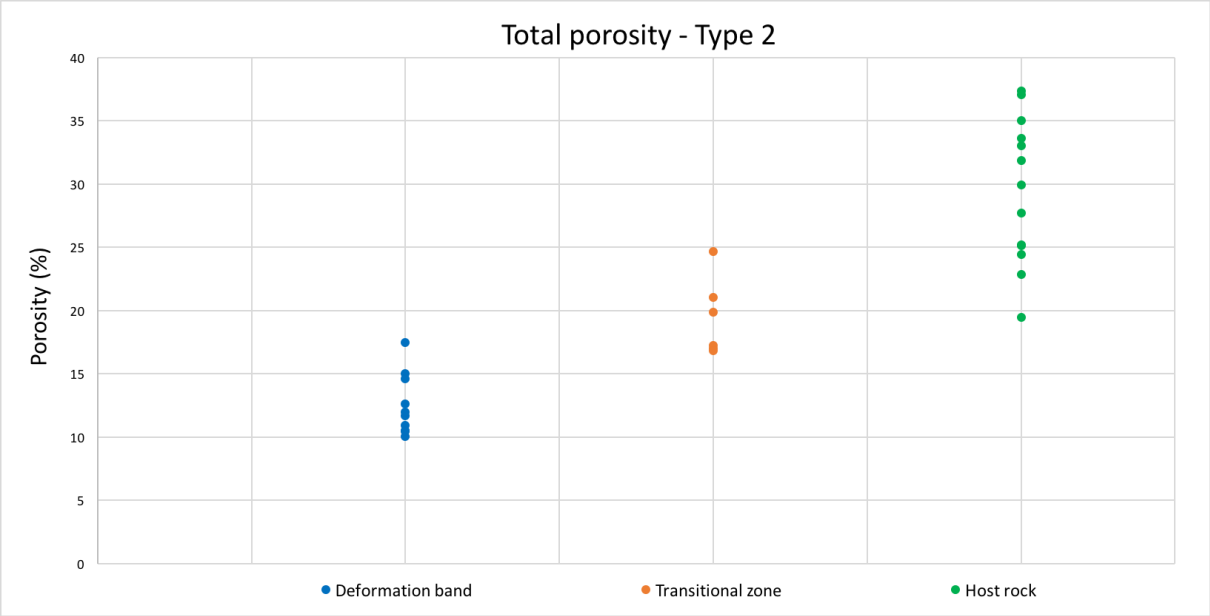

Figure 5.20: Total porosity calculated for the sampled type 2 DB. The plotted values are all the porosity measurements in each sub-zone. The DB contains the lowest porosity, the transitional zone intermediate, and the host rock contains the highest measured porosity.

5.2.3 Type 3

Type 3 DBs appear as conjugate sets of single strands, clusters or network of strands (Fig. 21A and B) with dextral and sinistral strike-slip shear movement. The strands crop out as dark grey elevated reliefs, or as striated planes (Fig. 5.21C), compared to the host rock. However, type 3 DBs are not strata-bound, and thus affect and dissect the entire studied succession (indicated in the stratigraphic log in Fig. 5.2). Type 3 DBs may evolve into faults, as expressed in Fig. 5.21D.

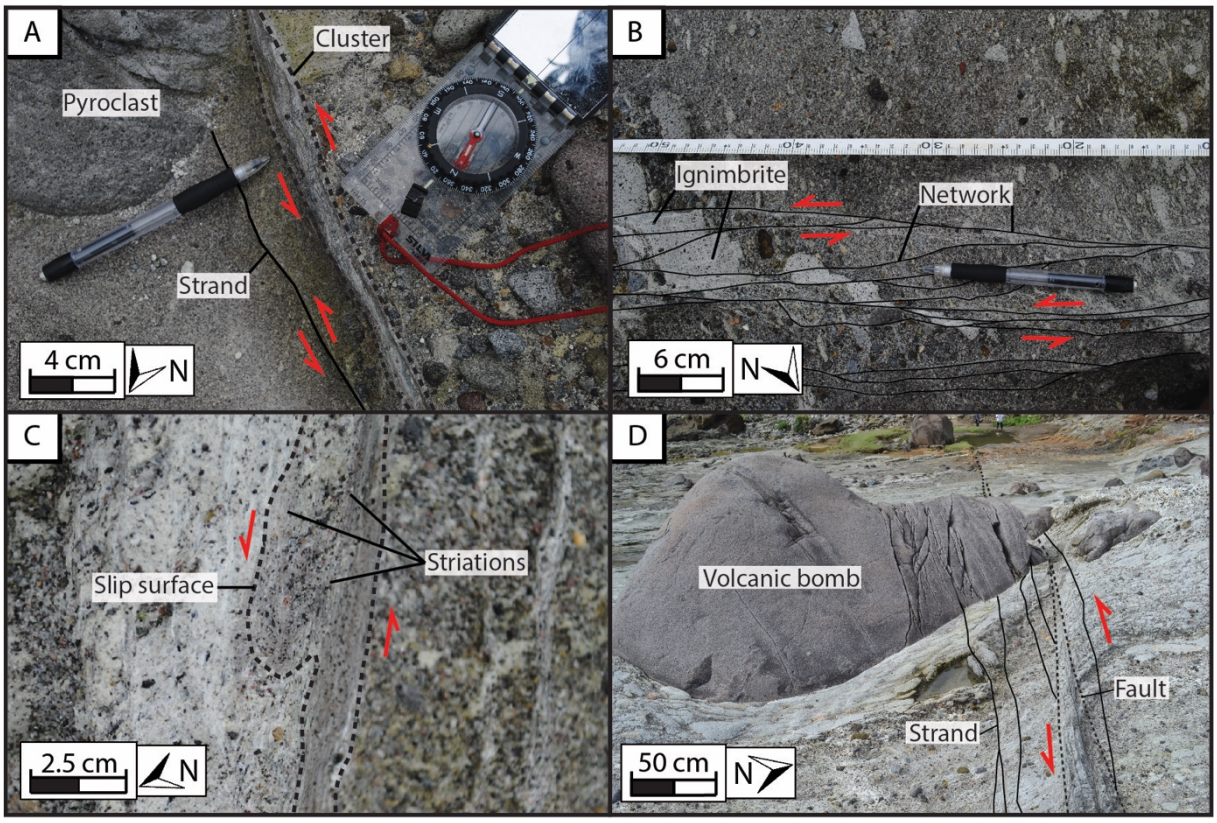

Figure 5.21: Field pictures and line sketches illustrating the abundant type 3 DB. A) Shows the difference between a cluster (dashed line) and a single strand (straight line). B) Field picture and line sketch of a network of strands, showing displacement of pumice in medium-graded tuffaceous sandstone. C) Field picture showcasing the striated plane of type 3 DB. D) Field picture and line sketch showcasing an evolved fault (dashed line) consisting of sinistral type 3 DB. The cracks in the volcanic bomb is oriented approx. 30° counterclockwise in terms of the shear displacement.

Even though the bands affect the entire studied succession, their intensity and thickness vary by lithology. Type 3 DB thickness varies from single strands of 0.5 mm to clusters of 2 cm. Notably, the type 3 bands may change its morphology through various succession in the succession. This is demonstrated in meso locality 3-1-A (Fig. 5.22A). The bands start out as a single strand in polygenic conglomerate. However, the same band appears as a cluster in the tuffaceous sandstone unit, and forms a network of strands in the ignimbrites unit.

Clear offset markers and slickenlines show that the two sets of DBs are associated with strike-slip sense of shear. The two sets are mutually crosscutting, and therefore coeval, trending NW-SE and WSW-ENE, respectively (Fig. 5.22B). The NW-SE striking set is characterized by sinistral sense of slip, whereas the WSW-ENE striking set have dextral motions (Fig. 5.23C). Both sets of DB exhibit relative high dip angle (60-90°). The sinistral shear bands exhibit a mean strike value of 125°, while the dextral is measured to 252°. The displacement varies along the bands, as shown in the Fig. 5.23.

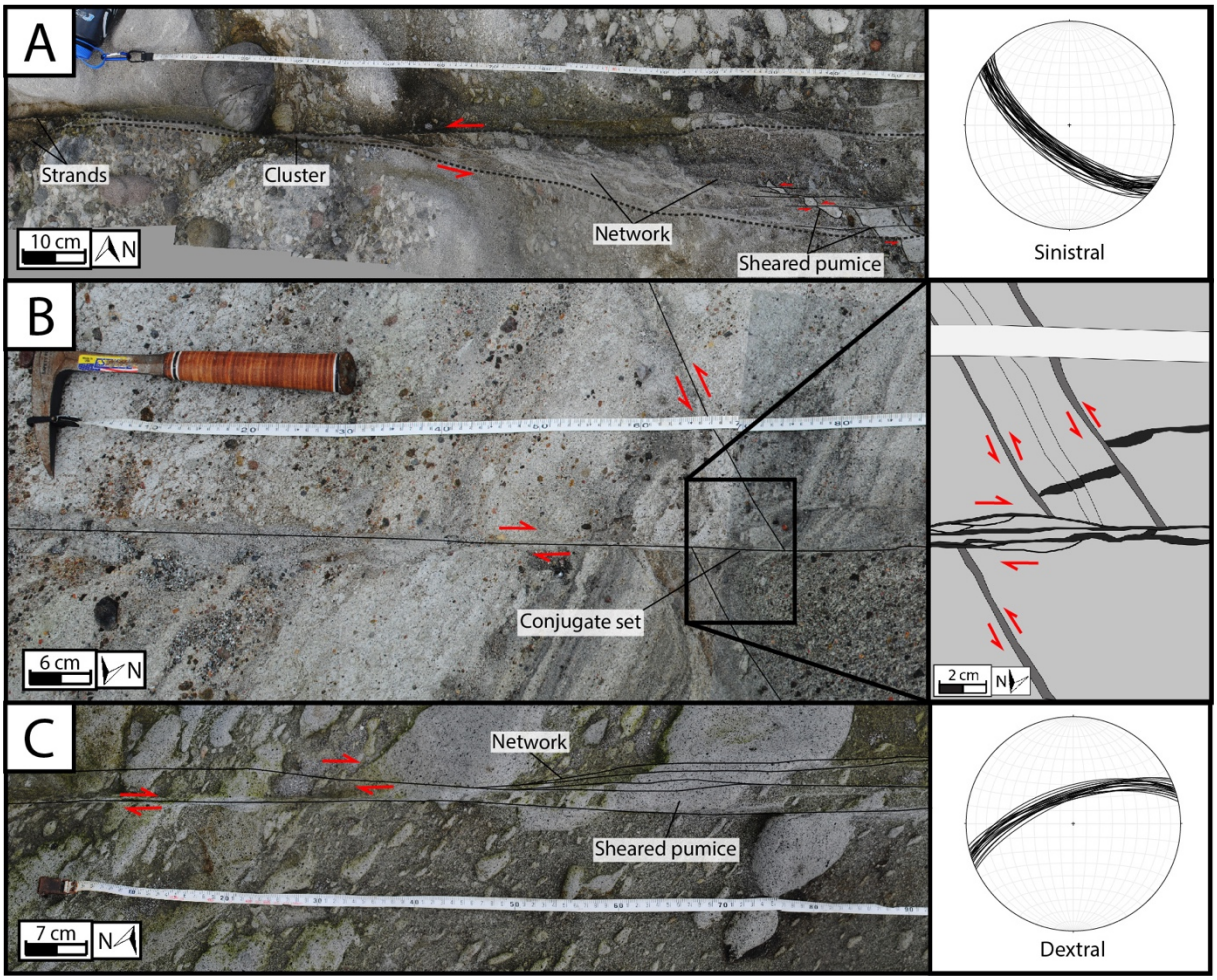

Figure 5.22: Field pictures of the meso localities for the type 3 DB. A) Meso locality 3-1-A showing the evolution of a sinistral type 3 DB from a single strand to an advance cluster. Pumices are observed within the networks and are sheared respectively. The strike/dip measurements for the sinistral type 3 DB shows a mean value of 125/67. B) Field picture and line sketch of meso locality 3-2-A, showing the interaction between the conjugated set of type 3 DB. Both the sinistral- and dextral strands are displacing each other, as shown in the sketch. The black lines illustrate the dextral strands, while the dark grey lines represent the sinistral. C) Field picture of meso locality 3-3-A. Individual strands are splitting into networks, causing multiple levels of displacement of pumices. The strike/dip measurements of the dextral type 3 DB show a mean value of 252/68.

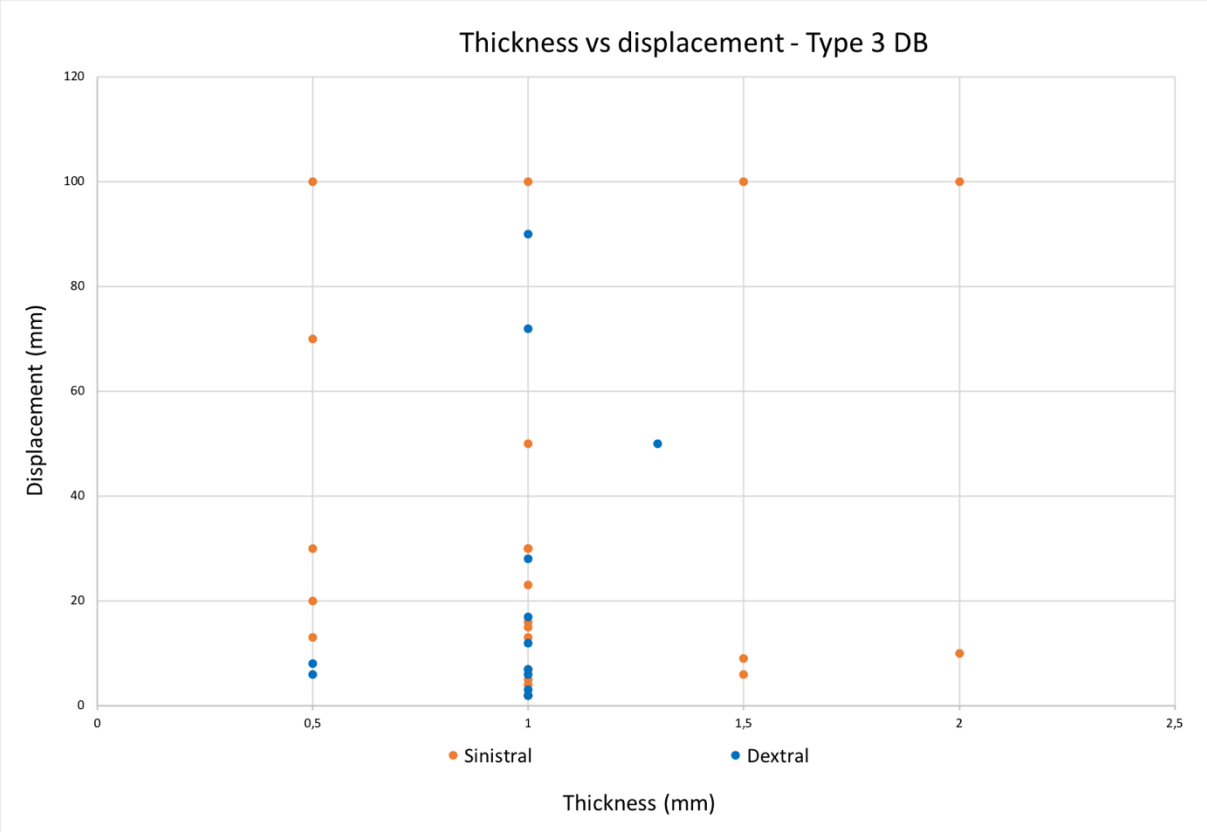

Figure 5.23: Crossplott of thickness and displacement measurements of the type 3 DB.

The DBs are observed in the field as narrow, tabular, localized structures. However, further analyses of the samples by optical microscope and BSE-SEM show that the bands are associated with great variations in thickness along strike (Fig. 5.24B). The strands appear with either abrupt or gradual boundaries to the host rock, respectively (Fig. 5.24A and 5.24B). The strands exhibiting gradual boundaries are encapsulated in a zone of compaction and grain reorganization, whereas the abrupt strands do not appear to feature such a zone. However, precipitated black minerals are observed along both boundaries. BSE-SEM images of the abrupt strand reveals fractures parallel to the DBs (Fig. 5.24D). Collision between mineral grains (i.e. Hertzian contact) are observed adjacent to the DBs, causing the weaker mineral to develop fractures (Fig. 5.24E).

The mineralogy within the DBs are identical to that of the host rock. Also, the overall grain size within the DB is smaller (Fig. 5.25) than the host rock, suggesting grain comminution.

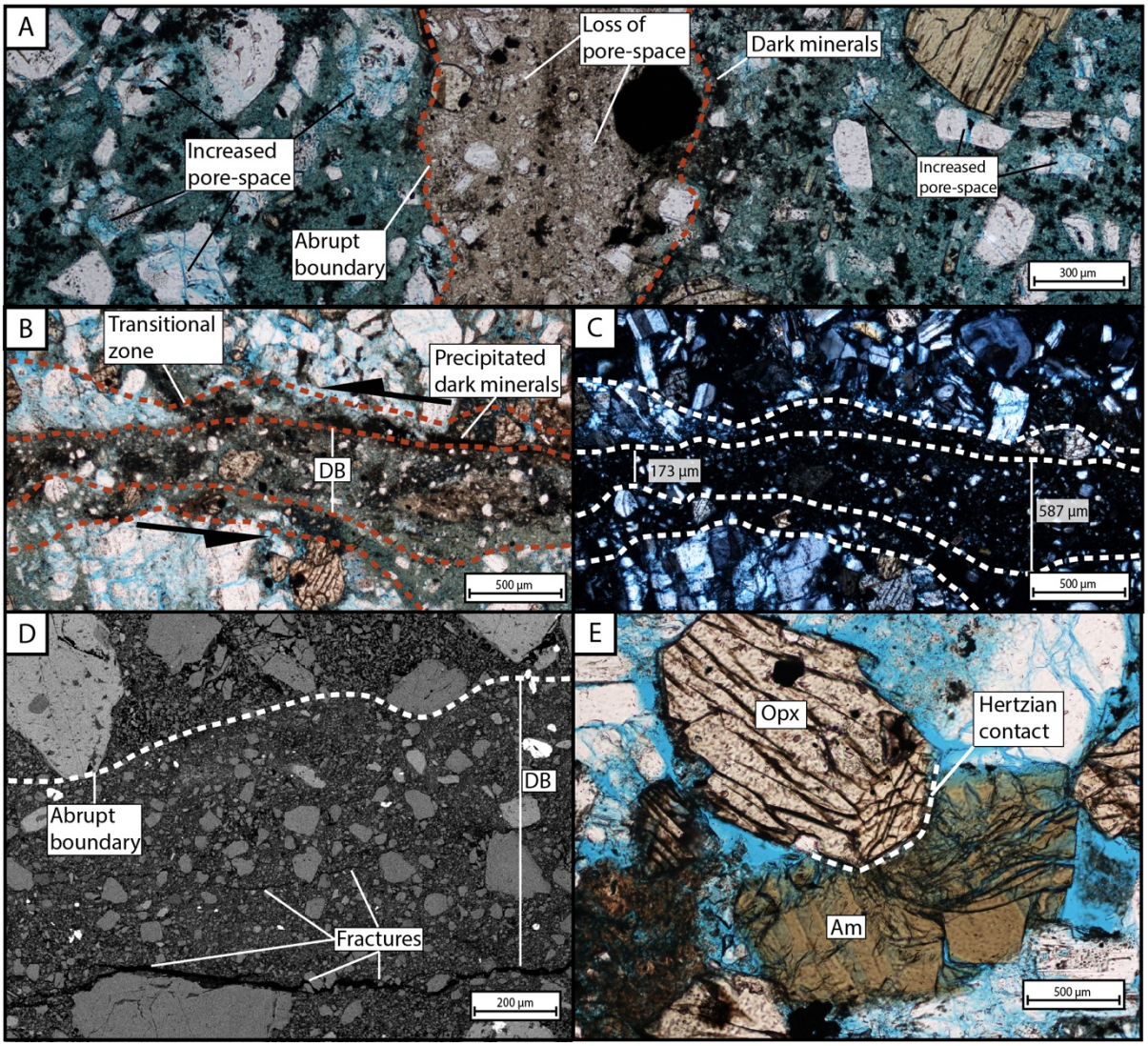

Figure 5.24: Light microscope picture of the type 3 DB. A) Picture of the type 3 DB in PPL, showcasing the abrupt boundary with respect to the host rock. The boundaries may also feature alteration. B) Picture in PPL showing the more gradual boundaries to the host rock. C) Picture in XPL of the latter band, showcasing the difference in thickness of the DB. D) BSE-SEM picture from type 3 DB featuring band parallel fractures. E) Grain fracturing as a result of Hertzian grain contact. Orthopyroxene is colliding with an amphibole.

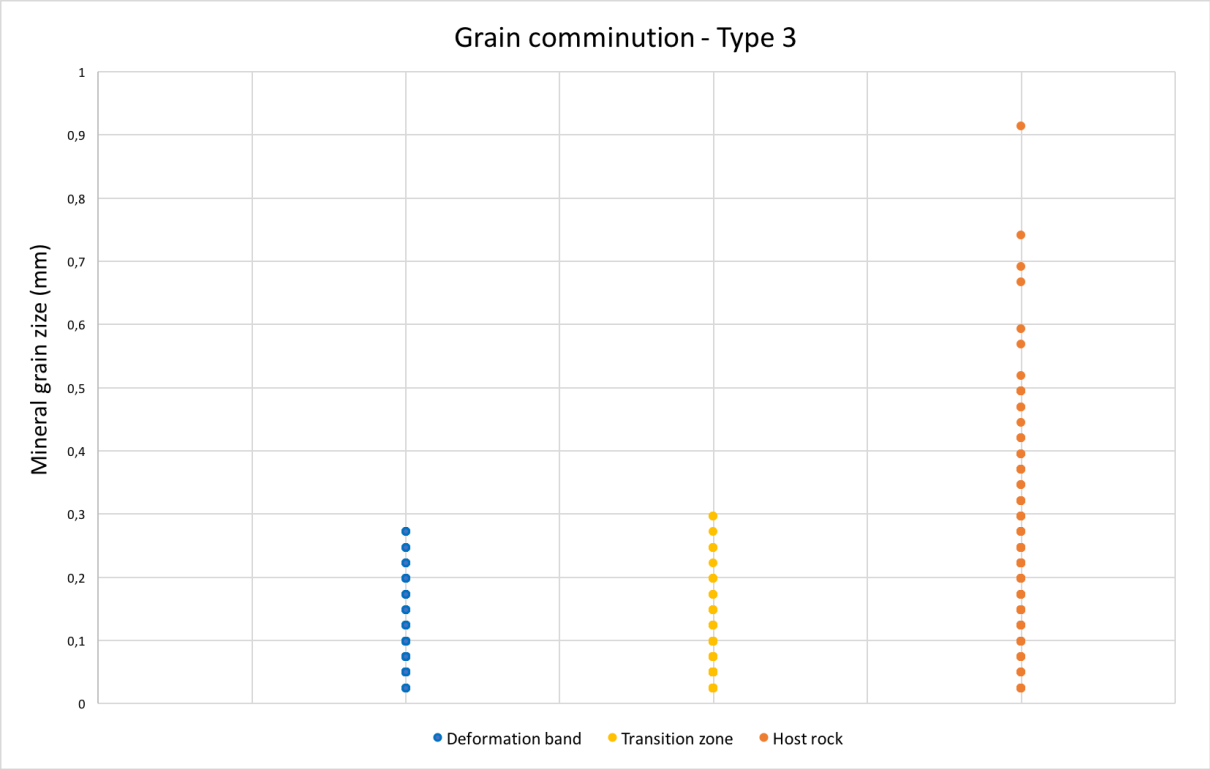

Figure 5.25: Mineral grain size measurements from the DB, associating transitional zone and respective host rock. Mineral grain measurements from the transitional zone were conducted from the DBs exhibiting gradual boundaries towards the host rock.

The porosity analysis of type 3 DBs does not differentiate between bands of dextral or sinistral shear displacement but are presented as one population (Fig. 5.26). The bands are associated with porosities in the range of 3.1% to 17.2%, with an overall average of 9.1%. The transitional zone between the host rock and the DB features an average porosity of 17.4%. In contrast, the host rock (tuffaceous sandstone unit) exhibit a porosity in the range of 26.0% to 38.5%, with an overall average of 31.9%.

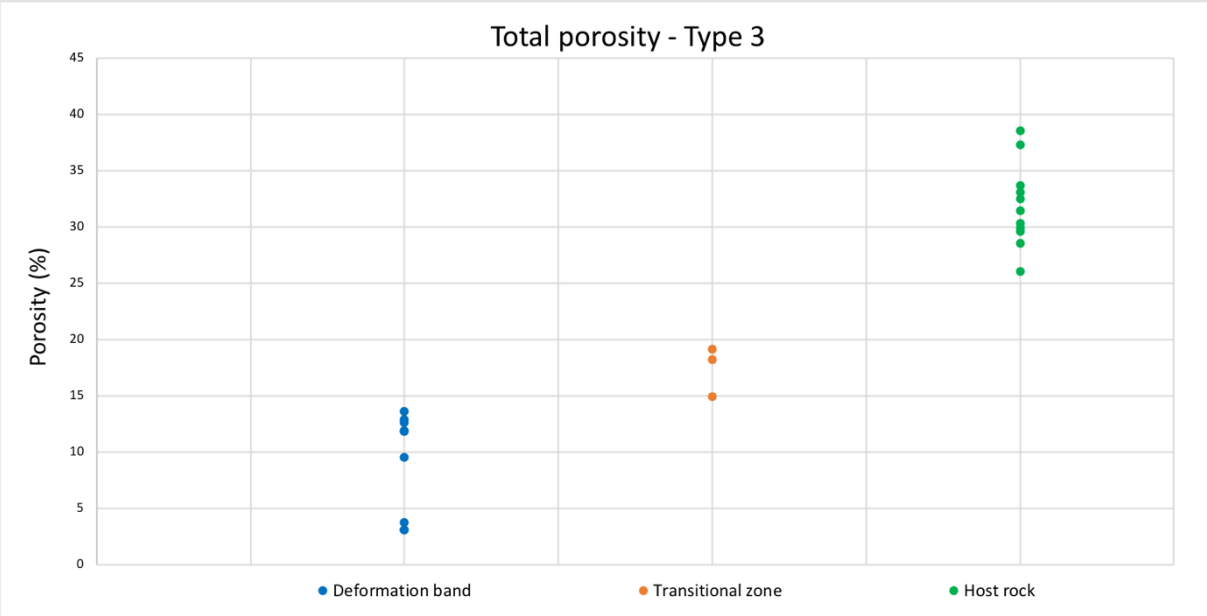

Figure 5.26: Total optical porosity measurements for type 3 DB. The plotted values are all the porosity measurements in each sub-zone. The DB contains the lowest porosity, the transitional zone intermediate, and the host rock contains the highest measured porosity.

Generally, mineral grains related to the DB are abundantly fractured in the thin sections, e.g. plagioclase. In Fig. 5.27A, plagioclase phenocrysts are prone to mineral drag as a disrupted grain contact between the host rock and the DB. The comminuted grains are dragged towards the principal direction of shear. This can be used as a kinematic indicator of the shear sense of the DB. Mineral drag is also affecting iron-oxides as elucidated by BSE-SEM imaging (Fig. 5.27C). Intragranular fractures, related to the mineral drag, are recognized as Riedel shear geometry fractures. Extensional fractures (T-fractures) are oriented counterclockwise to the principal direction of shear (Fig. 5.27B and Fig. 5.27D). Additional fractures are comprised of synthetic shear fractures (P- and R-shear fractures) and antithetic shear fractures (R'-shear fractures).

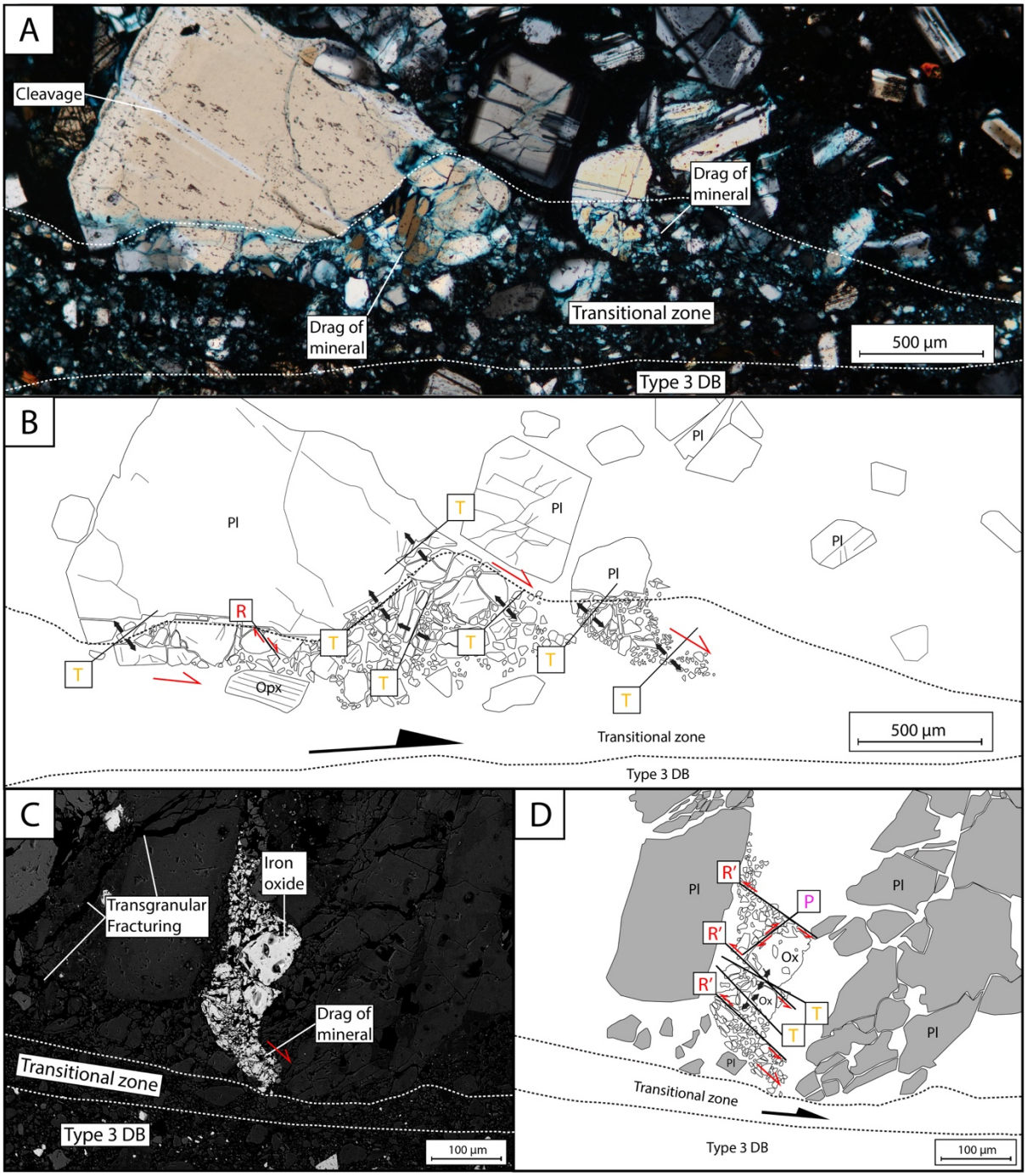

Figure 5.27: Pictures and line sketches from light microscope and BSE-SEM, showing mineral drag as disrupted mineral contacts. A) XPL picture from sample 33A-1 in light microscope. Plagioclase minerals are dragged with the main direction of shear (dextral type 3 DB). B) Illustrative sketch highlighting the various fractures. The sample is mainly dominated by T-fractures. C) BSE-SEM picture of mineral drag of an oxide, along the boundary from sample 33A-1. The oxide is severely fractured and dragged along the boundary of the DB. Transgranular fracturing is also documented. D) Line sketch of the latter picture. The oxide is prone to shear fracturing, such as R'-shear fractures, P-shear fractures and T-fractures.

Disrupted, or fractured, mineral grains are also observed with no apparent influence of shear forces. These minerals are often observed close to the DB, as shown in Fig. 5.28A and Fig. 5.28C. Generally, the minerals are prone to shear fractures perpendicular with respect to the most prominent cleavage plane. The angle of the fractures is either relative low dipping

(synthetic), or high-angle (antithetic) with respect to the DB. In contrast, extensional fractures affect the mineral parallel to the cleavage plane.

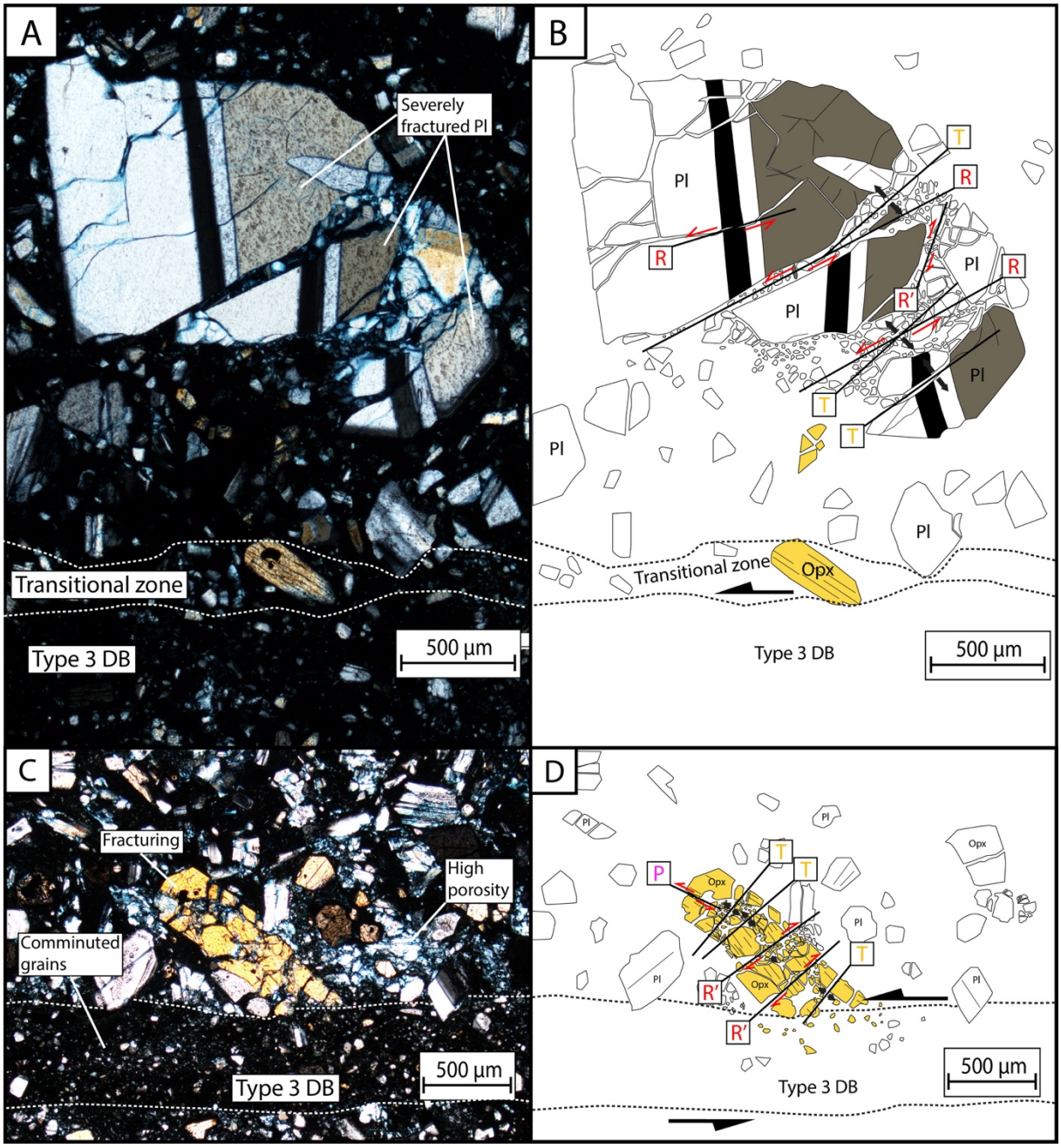

Figure 5.28: Light microscope pictures and line sketches of shear fractures adjacent to the DB, which is defined as the principal direction of shear. A) Light microscope picture in XPL showcasing the mineral of interest. The plagioclase is affected by the DB, and consequently fractured. B) Line sketch of the latter picture focusing on the fracture orientations. Three different fractures are distinguished, namely the Riedel shear fracture (R), R'-shear fracture and T- fracture. C) Light microscope picture of a fractured orthopyroxene (Opx). High porosity zones are observed as blueish zones due to the blue epoxy. D) Line sketch of the orthopyroxene, in which three types of fractures are observed: P-shear fracture, R'-shear fracture and T-fracture.

S-C structures are found within the network of strands (Fig. 5.29A). These asymmetric structures occur interposed between strands, and work as kinematic indicators of the shear sense

(Fig. 5.29C) (Fossen, 2010). To interpret the S-C structures, the following orientated structures are distinguished: C surface, C' surface and S foliation. The C surfaces are represented by the microshears and shear bands. The S foliation forms at an angle of 30-60° clockwise from the main C surface, which is parallel to the principal direction of shear. However, C' surfaces are not observed in the microstructural study.

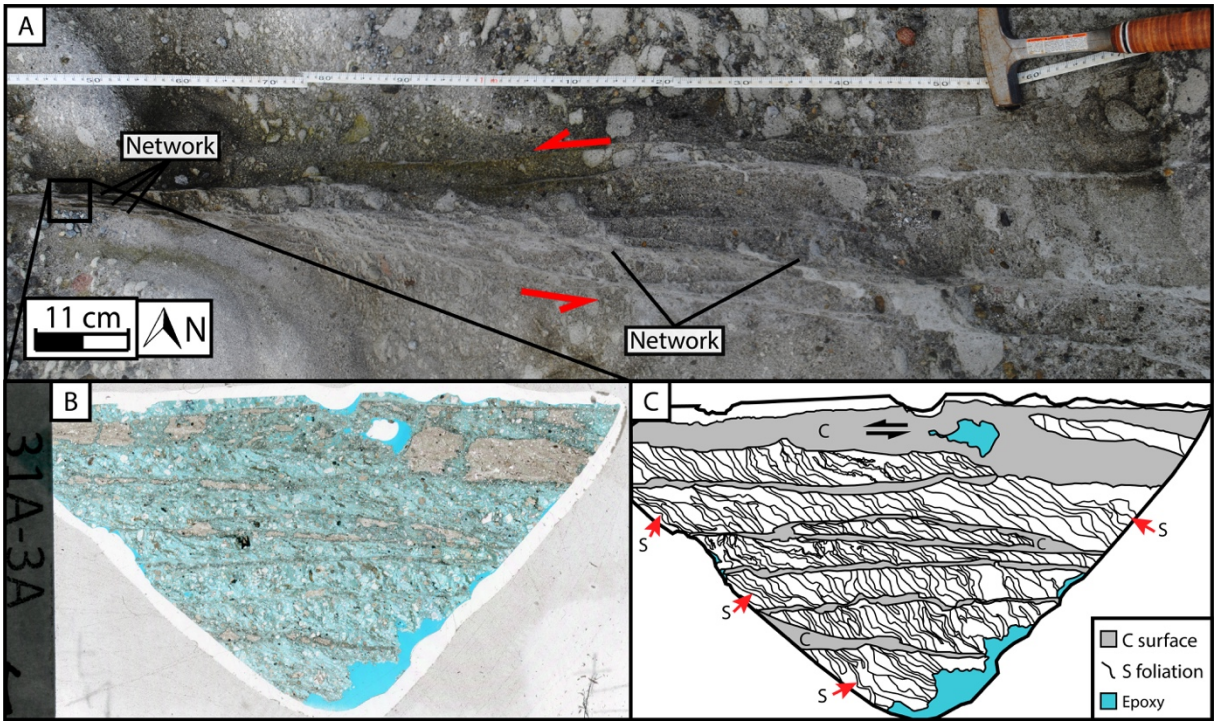

Figure 5.29: Field picture, thin section scan and line sketch of the S-C structures. A) Meso locality 3-1-A, showcasing the network of strands. The black square indicates the sampling of the following thin section. B) Thin section-scan of sample 31A-3A. C) Line sketch of the latter thin section, representing the various structures. The C surface and S foliation are distinguished.

In Fig. 5.30, a plagioclase mineral is observed in a S-C structure. The fractured fragments of plagioclase are oriented parallel to the S foliation, or sigmoidal-shaped volumes, creating an envelope of minerals (e.g. plagioclase in Fig. 5.30C). This envelope contains higher porosity than the adjacent envelope consisting of darker mineral fragments (e.g oxides). This is expressed in Fig. 5.30B and 5.30C, which shows pictures from BSE-SEM and XPL in light microscopy, respectively. Porosity measurements have been conducted to support this observation, in which the following results are found: 20.2% for the high porosity plagioclase zone, and 10.6% for the low porosity zones.

BSE-SEM analyses shows that intragranular fracturing dominates the mineral grains within the sigmoidal planes (Fig. 5.30B). Further, intragranular fractures are recognized as Riedel shear geometry fractures. Namely, R'-shear fractures and T-fractures are distinguished.

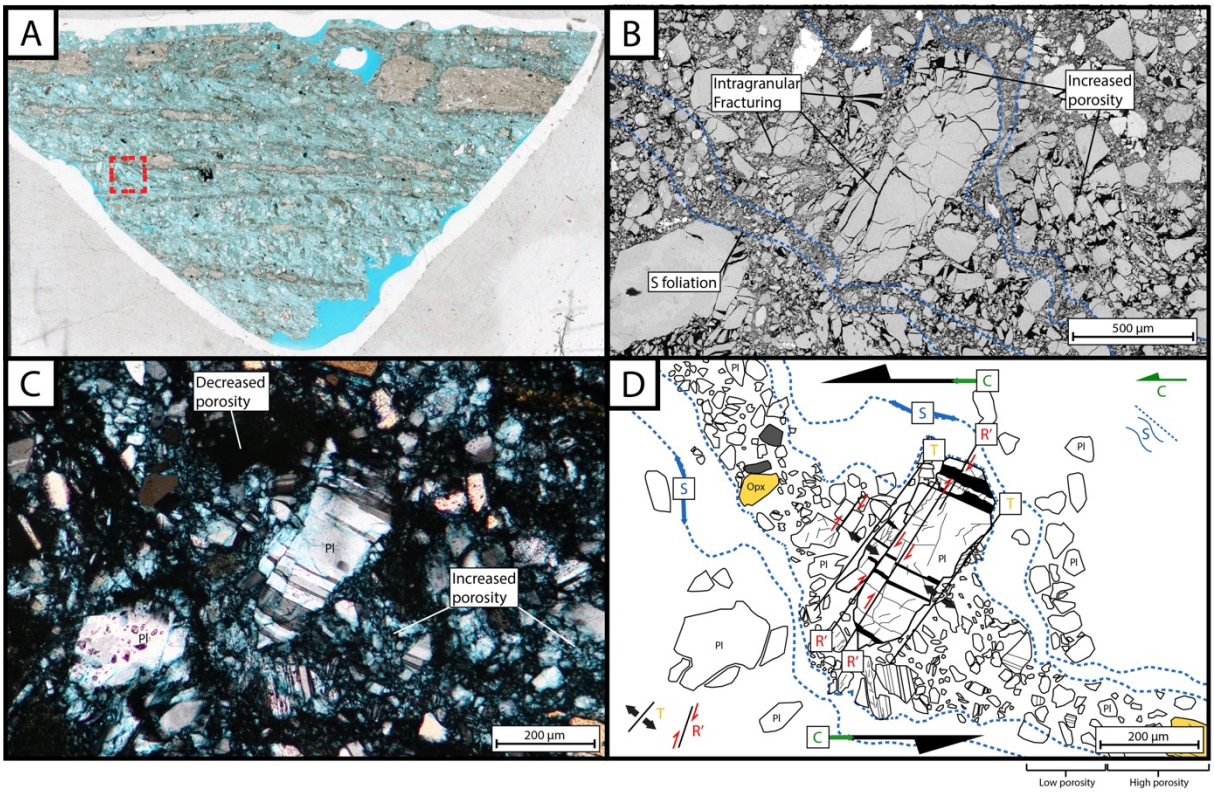

Figure 5.30: Observed S-C structure featuring plagioclase. A) Scan of the thin section of interest. The red square shows orientation of the following photos/figures. B) BSE-SEM picture of the plagioclase mineral and the S-C structure. The fractures appear to be bound to singular minerals. C) XPL picture from the same plagioclase mineral and S-C structure. A difference in porosity is indicated by the blue color, which is highlighted by epoxy in empty pore space. D) Line sketch of the latter, focusing on the present fractures. Notably, structure planes are defined as C surface and S foliation, and fractures as T-fractures and R'-shear fractures.

In contrast to plagioclase phenocrysts, comminuted pyroxene minerals create envelopes of low porosity. The pyroxene envelopes appear to be encapsulated by a blackish coating of iron oxides. This is shown in Fig. 5.31. Further, these low porosity zones are enclosed by a high porosity envelope of plagioclase fragments, thus segregating the different minerals.

Fractures within the low porosity zones appear to be restricted to the grain boundaries, which is also the case of the high porosity zones (Fig. 5.31B). The clinopyroxene in Fig. 5.31 is fractured mainly along two axes, which is recognized as Riedel shear geometry fractures. The most abundant ones are R'-shear fractures (antithetic), which is subparallel with the T-fractures (Fig. 5.31D). P-shear fractures is also present.

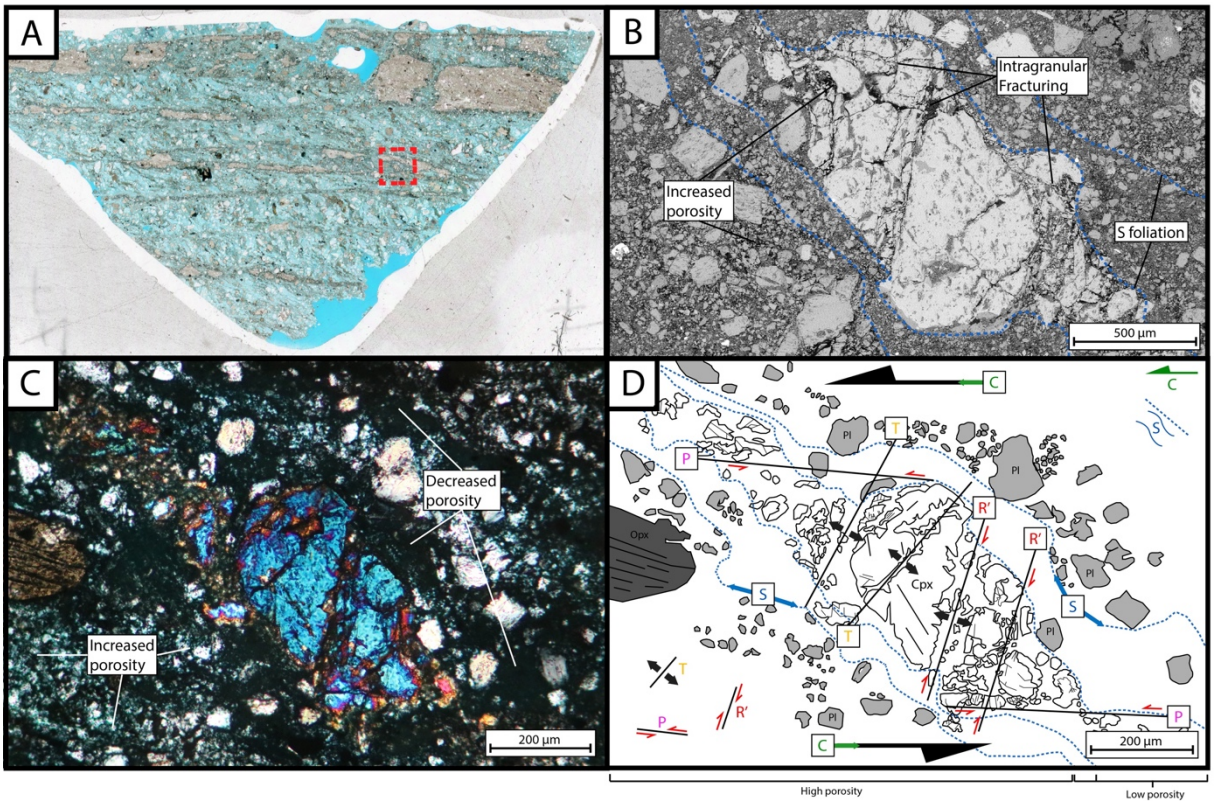

Figure 5.31: Observed S-C structure featuring clinopyroxene (CPX). A) Scan of the thin section of interest. The red square indicates the orientation of the following figures. B) BSE-SEM picture of the S-C structure and the CPX. The fractures appear to be bound to only the crystal face. C) The same mineral in XPL from light microscopy. A difference in porosity is indicated by the blueish color, which is highlighted by epoxy in empty pore space. Notably, low porosity is observed in the CPX-envelope. D) Line sketch of the light microscope picture. Multiple fractures are observed in this particular CPX: P-shear fractures, R'-shear fractures and T-fractures.

5.3 Summary of the results

The DBs in the Shihtiping White Tuff member are classified (*following* Aydin et al., 2006; Fossen et al., 2007) based on kinematics, which was determined based on their orientation relative to bedding, evidence for shear displacement, and porosity decrease within the bands relative to the host rock. The DBs are classified as follows:

TYPE 1: PURE COMPACTION BANDS

The type 1 DB are classified as pure compaction bands (PCBs) due to the observed reduction in porosity with respect to the host rock and the lack of shear movement. The bands are restricted to fine-graded tuffaceous sandstone (Fig. 5.2) and are oriented perpendicular to the bedding.

TYPE 2: REVERSE COMPACTIONAL SHEAR BANDS

The type 2 DBs are classified as reverse-sense *compactional shear bands* (RCSBs), based on the observations that RCSBs show evidence of porosity reduction, grain comminution/cataclasis and (reverse-sense) shear displacement. The flat-segments and ramp-thrusts are oriented parallel with the bedding and restricted to ignimbrite units and tuffaceous sandstone units. However, back-thrusts are only observed in fine-graded tuffaceous sandstone.

TYPE 3: STRIKE-SLIP COMPACTIONAL SHEAR BANDS

The type 3 DBs are classified as strike-slip *compactional shear bands* (SCSBs) due to the documented reduction in porosity with respect to the host rock, clear evidence of (strike-slip) shear displacement. These bands are not restricted to certain layers and pervasive through the entire studied area. RCSB are vertical and independent of local bedding.

6 Discussion

The aim of this chapter is to discuss the observations and results presented in Chapter 5. Specifically, the following topics are discussed: (i) deformation mechanisms of deformation bands (DBs) in volcaniclastics compared to other host rocks (Section 6.1), (ii) development and significance of structural fabrics observed in the studied DBs (Section 6.2), (iii) structural evolution of the studied area (Section 6.3), and (iv) implications for fluid flow (Section 6.4).

6.1 Deformation mechanisms in the studied deformation bands, and how they compare to other host rocks

Microstructural evidence suggests that purely granular flow mechanisms were responsible for the development of the pure compaction bands (PCBs). Minerals, e.g. plagioclase and orthopyroxenes, within the PCBs are reoriented parallel to the DB by its most prominent crystallographic plane (i.e. cleavage) (Fig. 5.11). The reorientation is accommodated by packing geometry which results in porosity loss. The minerals within the PCBs do not show any evidence of grain fracturing or grain comminution, which is why purely granular flow mechanisms are suggested for their development. However, clear grain fracturing (e.g. Fig. 5.28) and grain comminution (e.g. Fig 5.19A) are observed within the reverse compactional shear bands (RCSBs) and strike-slip compactional shear bands (SCSBs). Total porosity measurements conclude that the DBs cause porosity loss in contrast to the host rocks. It is clear from these observations that the dominating mechanism within these bands are cataclasis. Mineral grains along the boundaries of the DBs are intensely fractured and, in some cases, dragged along the principal direction of shear (e.g. Fig. 5.27). Notably, based on microstructural evidence from the results chapter, it is clear that mechanical fracturing is controlled by activation of weakness zones related to cleavage (i.e. cleavage microcracks). Firstly, the phenocrysts are reoriented 30-40° with respect to the DB by the most prominent cleavage plane. Furthermore, cleavage microcracking within the minerals develop shear fractures parallel and perpendicular of the most prominent cleavage plane. In addition, extensional fractures develop perpendicular to the cleavage plane. These intragranular factures show similar orientation to Riedel shear fractures in gouge zones (e.g. Yuan et al., 2015). Granular flow is also likely a contributing deformation mechanism within the RCSBs and SCSBs, as suggested by evidence of reorganization of fractured minerals parallel to the DBs (Fig. 5.11 and Fig. 5.16B). However, volcanic glass does not exhibit cleavage planes and do not feature clear fracturing. The glass is

prone to comminution, but not to the same extent as brittle phenocrysts. Evidence elucidated by BSE-SEM images (e.g. Fig. 5.16C) suggest that granular flow (reorganization and compaction) are a key mechanism for deformation of volcanic glass rather than cataclasis.

The study of DBs in porous sandstones, and more recently carbonates, has been a field of on-going research for several decades (Aydin, 1978; Aydin and Johnson, 1978; Antonellini et al., 1994; Mollema and Antonellini, 1996; Torabi, 2014; Ballas et al., 2015). Development mechanisms of DBs in porous sandstones are widely known to be granular flow (disaggregation/reorganization of grains), phyllosilicate smearing, cataclasis, cementation and solution. Internal properties that affect the deformation mechanism in sandstones are suggested to be comprised of porosity, mineralogy, grain size and shape, grain packing geometry and degree of cementation (Fossen et al., 2007; Fossen et al., 2018). In carbonates, complex interactions between granular flow mechanisms and pressure solution generally dominates the driving mechanisms for the development of DBs (Cilona et al., 2012; Tondi et al., 2012; Fossen et al., 2018), while internal properties are suggested to be comprised of grain sorting, intergranular porosity, and sphericity of the carbonate grains (Rustichelli et al., 2012).
However, the controls of DBs in volcaniclastic rocks are not well established. Studies conducted by Wilson et al. (2003) and Soden and Shipton (2013) suggest that welding is an important control on deformation in volcaniclastic rocks in addition to host rock porosity. Mineral grains in the studied non-welded volcaniclastic host rocks clearly exhibits evidence of reorientation, translation, fracturing and comminution as result of strain localization. Documented Hertzian grain contacts (Fig. 5.24E), mechanical grain fracturing and disrupted grain contacts suggest that cataclasis is initiated by stress concentrations at grain contacts (cf. Antonellini et al., 1994; Fossen et al., 2018), which resembles deformation mechanisms in porous sandstones. Notably, the grain fracturing and grain comminution within the volcaniclastic host rocks are more controlled by the mineral cleavage in contrast to siliciclastic host rock. This might be related to the mechanical strength of the minerals and the lack of cleavage of quartz, which is a common mineral in porous sandstones (e.g. Aydin, 1978; Fossen et al., 2018).

The compactional shear bands in this study may also deviate from classic compactional shear bands, in porous sandstones, due to documented slip surfaces. The RCSBs and SCSBs exhibit striated slip planes in the field (e.g. Fig. 5.13C), which is represented by abrupt boundaries with and without parallel fractures in microstructural analyses (e.g. Fig. 5.16A). In addition, these bands lack a grain compaction envelope around the cataclastic zone. The DBs

with slip surfaces often exhibit large displacements in contrast to individual strands without a slip surface, and are generally thicker than 2 mm. Studies by Aydin and Johnson (1978) suggests that an increased thickness of the crushed zone within DBs might result in an instability of strain hardening (commonly associated with cataclastic bands). Hence, reducing interactions and strength between crushed mineral grains which results in strain softening. Mechanical weak volcanic glass fragments may exhibit a lubricating effect on grain boundaries, favoring non-cataclastic granular flow. Hence, contributing to strain softening, similar to previous studies of phyllosilicates within DBs (e.g Fossen et al., 2018). Based on these interpretations, formation of slip surfaces might be related to strain softening of the crushed material within the DBs, which have previously been suggested in porous sandstones by Rotevatn et al. (2008).

Intergranular pressure solution and cataclastic pore collapse are not observed in this study, which are commonly associated to DBs in carbonate rocks (e.g. Tondi et al., 2006; Zhu et al., 2010). In experimental studies of DBs in non-welded ignimbrites by Zhu et al. (2011), the DBs showed similarities to bands in porous limestones due to the extent of cataclastic pore collapse, which initiated from stress concentrations at the periphery of larger pores (> 33 μm). Findings from Zhu et al., 2011 suggests that concentric halos (i.e. intense damage rims) encapsulate collapsed pores, in addition to comminuted fragments that may spall and fall into the pores. However, evidence from this study suggests that cataclasis is initiated and controlled by stress concentrations at mineral contacts rather than at the periphery of pores. Small vesicles (< 33 μm) within the volcanic glass are observed (i.e. pores) in the studied samples with no sign of concentric halos or comminuted fragments.

In sum, two important deformation mechanisms are distinguished in the DBs of this study: granular flow and cataclasis. The observations from microstructural analyses suggests that mineral grain fracturing and comminution is controlled by the orientation of the cleavage plane with relative orientation to the DB. Comparisons of the deformation mechanisms in volcaniclastic rocks to other types of host rocks conclude that the development of DBs in this study are different of sandstones or carbonates. Notably, the mineralogy of the host rocks serves as the key factor for the development of volcaniclastic DBs.

6.2 S-C fabric in the studied deformation bands

In contrast to previous studies of DBs, the SCSB in this study exhibits a structural fabric that resembles what is known as 'S-C fabric' in ductile shear zones or gouge zones (e.g. Lister and Snoke, 1984; Culshaw, 1987; Buatier et al., 2015). The S-C fabric is not common but is observed locally within networks of the SCSB. This structural fabric consists of μm-thick slip zones (i.e. C surface) with high degree of comminution parallel to the DBs, which suggests pure mechanical processes (Fig. 5.29B and C). Sigmoidal-shaped structural envelopes (i.e. S foliation) occur between the C surfaces and are characterized by moderate comminution of mineral grains with porosity reduction in contrast to the host rock (Fig. 5.30C). C' foliation is not observed, which suggest that the structural fabric is not well-developed, as C' foliation tend to form during the late stage of shear zone activity due to increased strain (Fossen, 2010).

As established in section 6.1, the SCSBs exhibits slip surfaces (i.e. slip zones) which is interpreted as a result of strain softening due to increased accumulation of strain. Localized slip zones within DBs have previously been described by Rotevatn et al. (2008) and Nicchio et al. (2018) in other host rocks with similar attributes (coarse-grained siliciclastic host rocks with high porosity). These slip zones comprise the C surfaces in the S-C fabric. Furthermore, the host rock situated between the C surfaces in SCSB networks are sheared as the result of strain accumulation. Mineral grains are mechanical reoriented 30-40° due to the brittle shear deformation and comminuted by cleavage-controlled fracturing. Thus, sigmoidal-shaped volumes (i.e. S foliation) are developed as a result from the preferred orientation of the fractured mineral grains. The shear fracturing and extension between mineral cleavage planes within these zones causes an increase of pore space, thus creating an envelope of increased porosity in contrast to the host rock. Notably, feldspars develop envelopes of higher porosity than pyroxenes. These envelopes are defined as S foliation and forms an angle of 30-60° from the main direction of shear. Based on these interpretations, the following conceptual evolutionary model is proposed for the development of S-C foliation related to DBs:

Firstly, grain fragmentation occurs as a result of interplay between and granular flow and cataclastic mechanisms (rotation, translation and fracturing of mineral grains) in the DB (Fig. 6.1B). The porosity is partially reduced in this stage (mineral packing geometry), and the grain comminution is moderate. Further, grain comminution increases by shearing until the band

develops cataclastic fabric (Fig. 6.1C) as a result of strain hardening. As strain is accumulating within the deformed host rock, µm-thick slip zones are accreted within the band boundaries as a result of strain softening (Fig. 6.1D). These zones consist of heavily comminuted minerals and fragments of volcanic glass, which is referred to as the C surfaces. Heavily comminuted mineral fragments interposed between these zones are prone to reorientation as a result of increasing shear movement. Hence, sigmoidal-shaped volumes are developed between the C surfaces (Fig. 6.1E).

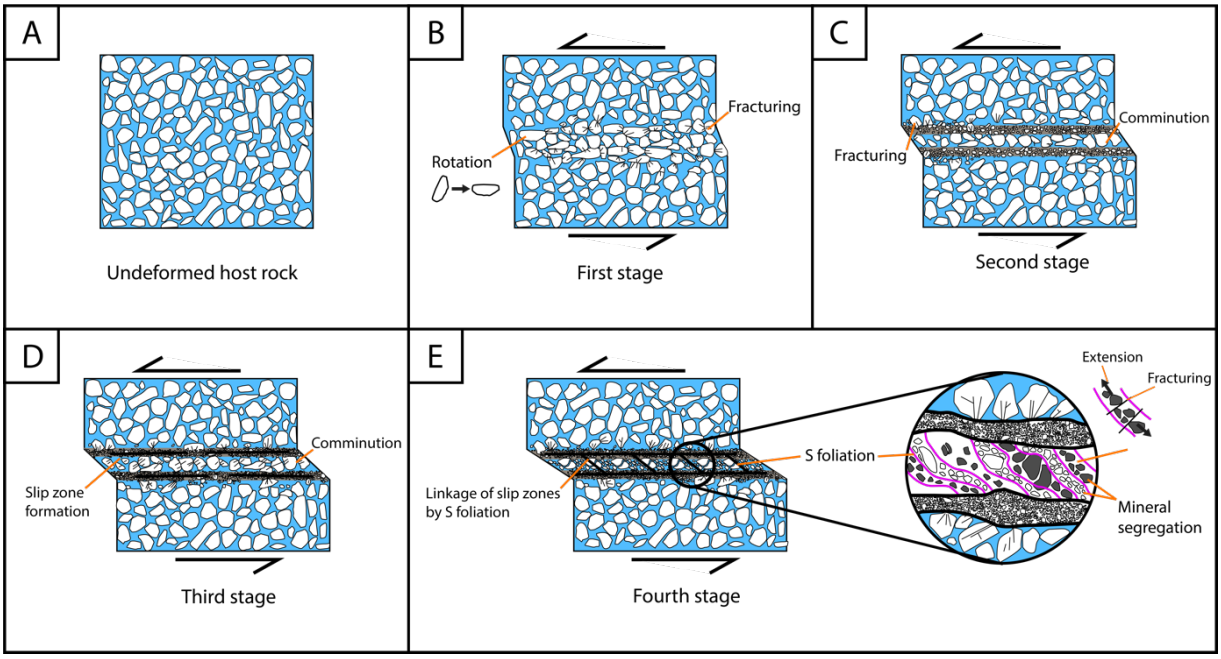

Figure 6.1: Evolutionary model of the S-C fabric related to the SCSB in tuffaceous sandstone, inspired by Nicchio et al. (2018). A) Undeformed host rock (tuffaceous sandstone). B) Initial stage of the development of S-C fabrics. Granular flow mechanisms, such as translation and rotation, of mineral grains occurs. C) Grain fracturing and comminution occurs due to increased shear forces. D) Comminuted grains forms slip surfaces (C surface) within the DB. E) Shear forces increases, and the slip surfaces are joined together by S foliation.

6.3 How DBs relate to the structural evolution of the studied area

The volcaniclastics of the Shihtiping White Tuff originates from the aforementioned Luzon arc, which formed in response to the subduction of the South China Sea plate beneath the Philippine Sea plate (Teng, 1990; Song and Lo, 2002). Three types of DBs are observed within this succession, namely PCB, RCSB and SCSB, which differ in terms of kinematics, microstructural deformation mechanisms and network architecture in the outcrop. In order to understand the spatiotemporal evolution of the studied bands, and elucidate their age relations, we use field observations (cross cutting relations, orientations relative to folded bedding) and discuss this in light of previous published material about the regional stress state through time. The PCBs and

RCSBs are both consistently cross cut by the SCSBs; the SCSBs are therefore clearly younger than PCBs and RCSBs. However, relative age relations between PCBs and RCSBs are not observed in the field. Thus, three competing hypotheses are proposed that may account for how PCBs and RCSBs developed, prior to the later development of SCSBs:

i. PCBs developed first
ii. RCSBs developed first
iii. PCBs and RCSBs developed simultaneously

The first hypothesis, i), suggests that the PCBs were the first to initiate. These bands are strata-bound in poorly consolidated tuffaceous sandstones and appear sub-vertical to the bedding (50-80°). The orientation of the bands is consistent with nucleation and growth perpendicular to bedding, and perpendicular to a horizontal maximum principal stress axis ($\sigma 1$) related to shortening due to the ongoing plate convergence (Sibuet and Hsu, 2004). This suggests that the PCBs originated from horizontal compression rather than vertical loading. In addition, PCBs are accommodated by granular flow mechanisms which may suggest shallow burial depth and low confining pressure (e.g. Fossen et al., 2007). Further, large scale folding is initiated due to ongoing shortening of the studied succession. Consequently, confining stress and burial depth are increasing, which promotes a shift of deformation mechanisms from granular flow to cataclasis (e.g. Antonellini et al., 1994; Mair et al., 2002; Fossen., 2007). The RCSB develops coevally with folding as a result of thrusting and layer-parallel shortening of the bedding (e.g. Fossen et al., 2018).

The arguments of the first hypothesis counter the second hypothesis, ii), which suggests that the RCSBs developed first. This appears implausible as the deformation mechanism would shift from cataclasis to granular flow, and back again to cataclasis (SCSBs).

The third hypothesis, iii), suggests that the PCB and the RCSB initiated simultaneously under the influence of compressive forces. These bands do not interfere within the studied stratigraphy and are bound to certain layers. The PCB initiated in very porous, poorly consolidated tuffaceous sandstones, whereas the RCSB initiated as a result of layer-parallel shortening of the bedding. Layers containing larger fragments of pumices and bomb sags, e.g. the polgygenic conglomerate unit, were not affected by the deformation during this stage.

Hypothesis i) however, appears more plausible than hyptothesis iii). In regards of hypothesis iii), it is unlikely that both PCBs and RCSBs would develop in similar successions and not interfere. In addition, the strike/dip measurements between PCBs and RCSB suggests a shift in stress direction, in which RCSB are parallel to the folded bedding while the PCBs are not (Fig. 6.2A and B). Hypothesis ii) suggests that increased burial stress and a shift of deformation mechanisms resulted in the development of the RCSBs and SCBSs (Fig. 6.2B). This hypothesis coincides with previous studies that have shown that PCBs often predates other shear-dominated DBs in porous sandstones related to horizontal shortening (e.g. Aydin and Ahmadov, 2009; Fossen et al., 2015). Based on these observations, hypothesis ii) appears most plausible in terms of the timing of development between the PCBs and RCSBs. As established initially based on cross cutting relations, the SCSBs were the last to form. The SCSBs are not affected by the folding and appear with a high angle towards the bedding (60-90°). The SCSBs are coeval, thus developed with the maximum principal stress axis ($\sigma 1$) as the acute bisector between the conjugate set. The progressive burial lead to a high increase of confining stress. Consequently, the vertical stress became greater than the intermediate horizontal stress. Thus, flipping the orientation of $\sigma 2$ and $\sigma 3$ (Fig. 6.2B and Fig. 6.2C) which induces a change in stress state, resulting in a transition from reverse-sense kinematics (RCSBs) to strike-slip kinematics (SCSBs) (Fig. 6.2C).

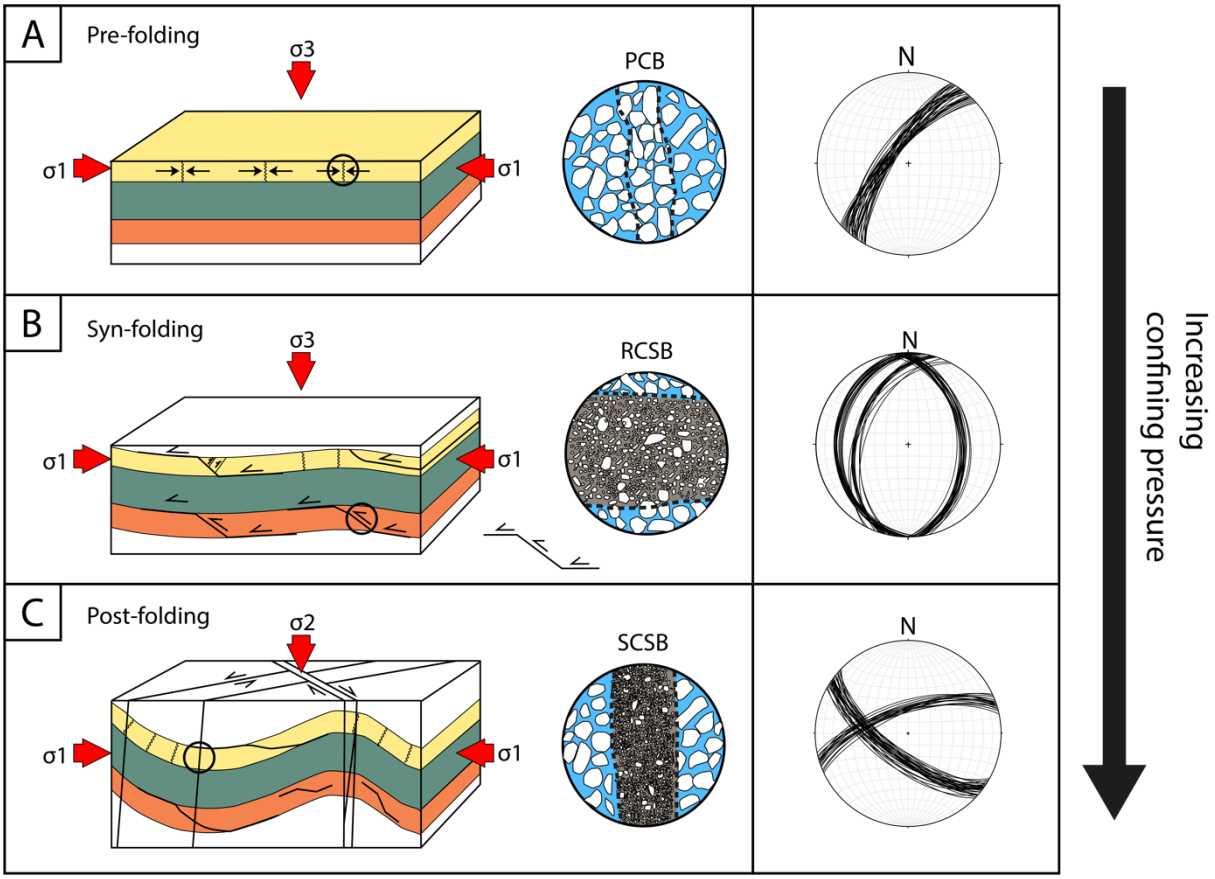

Figure 6.2: Evolutionary model of the development of DBs in a contractional regime. A) Initial stage of DB development. Compression induces the pure compaction bands (PCB). B) Folding occurs and is accommodated by the development of the RCSB due to increased confining pressure. C) σ3 and σ2 switches orientation due to increased overburden pressure. The development of SCSB is initiated post-folding.

6.4 Implications for fluid flow in subsurface reservoirs/aquifers

DBs are widely proven as important features which may act as conduits or barriers for fluids (e.g. Fisher and Knipe, 2001; Fossen and Bale, 2007; Ballas et al., 2015). Porosity measurements from this study suggests that DBs represent zones of reduced porosity, which varies within different types of bands (Fig. 6.3). The highest porosity loss in contrast to the host rock occurs in DBs accommodated by grain fracturing and comminution (Fig 6.3). Consequently, the compactional shear bands will reduce permeability due to intense grain crushing (e.g. Fossen et al., 2018). The PCBs exhibits the least cataclasis and therefore the least permeability-reducing effect, while the RCSBs and SCSBs exhibits the largest effect. The porosity measurements in this thesis are presented in Fig. 6.3, which compares the data with previous studies of DBs in sandstone. Although the host rocks are of different origin, the porosity data are comparable. The RCSBs and SCSBs in this study show similar porosity reduction to previous measurements of slip surface featuring bands by Rotevatn et al. (2008).

Studies conducted by Torabi et al. (2013) suggests that thick clusters of cataclastic DBs, particularly if paired with faults, can induce potential hydrocarbon traps. Faults may form preferential, vertical fluid migration pathways between aquifers situated several hundred meters apart when the permeability of the fault is strongly anisotropic (Bense and Person, 2006). Consequently, the faults may still act as a barrier to lateral flow. In terms of this study, the RCSB and SCSB features slip surfaces that provides evidence of palaeo-fluid flow due to precipitated black minerals (oxides) along their outer boundaries (e.g. Fig. 5.16A). The development of slip surfaces within the bands may result in anisotropic permeability (e.g. Rotevatn et al., 2008), in which the bands may function as conduits for band-parallel fluid flow but representing baffles for across-band flow.

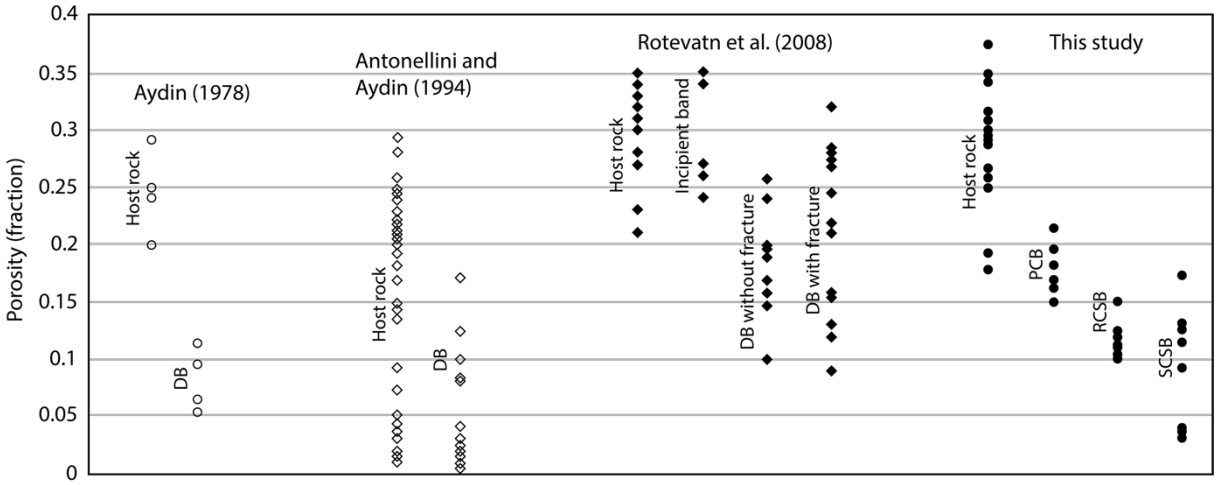

Figure 6.3: Porosity data for DBs in this study compared to data from Aydin (1978), Antonellini and Aydin (1994), and Rotevatn et al. (2008). Macro- and microporosity were analysed by the means of photomicrographs and BSE-SEM images. Modified after Rotevatn et al. (2008).

Evidence from this study suggest that DBs may influence and control fluid flow in a subsurface reservoir. Examples of some well-known processes and areas of application are:

i. Geothermal, hydrocarbon or groundwater reservoirs/acquifers
ii. Pollutant transport and groundwater contamination
iii. Ore deposits

DBs, faults, fractures, and structurally complex zones are widely recognized to influence subsurface reservoirs and aquifers. However, as the geometry and architecture of small-scale fracture networks and DBs often fall beneath seismic resolution, the prediction of subsurface flow is very complicated (Rotevatn et al., 2009). To further investigate of their influence on reservoirs and aquifers, outcrop analogues and field-based documentation can provide reliable

predicitions. Findings from Sass and Götz (2012) suggests that permeability and thermal conductivity belong to the key parameters in order to understand the fluid flow in geothermal reservoirs. Geothermal energy is a renewable energy source in the form of heat or electricity, which is gaining more importance as an alternative to hydrocarbons. (Sass and Götz, 2012; Kana et al., 2015; Rühaak et al., 2015). In terms of volcaniclastic reservoirs, findings from Sass and Götz (2012) and Mielke et al. (2015) suggests that the degree of alteration of magmatic rocks seems to have similar importance as distinct sedimentary facies types of siliciclastic and carbonate rocks. Recrystallization processes in volcaniclastic rocks (e.g. non-welded ash tuffs) of primary minerals and precipitations of secondary hydrothermal minerals with advancing alteration may cause permeability to increase by a few percent. However, advancing alteration may cause a decrease of the permeability in sandstones up to multiple orders of magnitude. Most volcanic geothermal reservoirs have relatively low matrix permeability, thus fluid flow and bulk permeability are controlled by structures, such as DBs and fractures (Dobson et al., 2003).

DBs, faults, fractures, and structurally complex zones in the shallow crust also applies to environmental issues related to flow patterns (direction and obstruction) of groundwater, and deposal contaminant transport (Bense et al., 2003; Mayer et al., 2007; Bense et al., 2013). Studies carried out by Fossen and Bale (2007) suggests that DBs and DB clusters works as barriers for fluid flow, which coincides with findings in this study. Precipitated oxides along the outer boundaries of DBs provides evidence of palaeo-fluid flow. However, aquifer vulnerability may depend on the interaction with geothermal reservoirs (La Felice et al., 2014). Arsenic is a well-known toxic and carcinogenic metalloid, which may be diffused from host rocks (e.g. sulphide ore deposits, pyrites) into the groundwater in active volcanic regions (Saunders et al., 2008; Bundschuh and Maity, 2015).

The understanding of DBs, and faults, may be of economic importance in terms of economically significant ore deposits, and characterizing the risk for hydrocarbon leakage (Beukes et al., 2003; Rotevatn and Fossen, 2011). Findings from Sibson (1996) suggests that fluid overpressure in the crust hold great control on faulting and mineralization. In addition, mineralizing environments can be characterized through varying seismic style in different tectonic settings. In terms of volcanic reservoirs, studies by Mao et al. (2008) showed that magma conduits formed differentiated intrusions along deep faults, thus resulting in Cu-Ni

sulphide deposits. Additional mineral deposits in tuffs associated with faults and fractures are Fluorspar, Beryllium and Uranium (Lindsey, 1982).

In sum, DBs, fractures, faults and structural complexity zones exhibit significant controls on fluid flow within subsurface reservoirs (e.g. geothermal, hydrocarbon, groundwater). This have been highlighted through the findings of this study by outcrop-based investigations, in addition to porosity measurements by image analysis, in volcaniclastic host rocks.

7 Final conclusions and further work

7.1 Conclusions

The main aims of this thesis have been to improve and gain understanding on the deformation mechanisms for deformation bands (DBs) in volcaniclastic rocks. These aims were reached through field-based investigations, analyses of microstructural and lithological characteristics of DBs and documented porosity variations between host rocks and DBs. From the results and discussion presented herein, the following conclusions are drawn:

- Microstructural analyses revealed clear evidence that deformation mechanisms for DBs in volcaniclastic rocks are dominated by granular flow (PCB; type 1) and cataclasis (RCSB; SCSB; types 2 and 3) of mineral grains. Notably, mineral fracturing and comminution are initiated by stress concentrations at grain contacts.
- Microstructural study suggests that mineral cleavage (i.e. cleavage microcracking) exerts a strong control on the deformation mechanisms in the DBs. Riedel shear fractures and extensional fractures are initiated parallel and perpendicular of the most prominent crystallographic axis in the mineral.
- This study has, for the first time, documented the occurrence of S-C fabric in DBs within volcaniclastic host rocks. The S-C fabric are suggested to be a result preferred orientation of fractured and comminuted mineral grains between networks of DBs featuring slip zones.
- The studied DBs are a result of shortening related to plate convergence. Cross cutting relations, orientation relative to bedding and prominent deformation mechanisms suggests that pure compaction bands were the first to develop followed by reverse compactional shear bands and strike-slip compactional shear bands, respectively.
- Porosity estimations show a general trend of lower porosity within the DBs in contrast to the host rock, which coincides with porosity measurements of similar band types within sandstones and carbonates. These findings suggest that compaction shear bands within volcaniclastic host rocks may affect the fluid flow within subsurface reservoirs/aquifers. However, permability measurements should be conducted to make an accurate statement regarding the bands effect on fluid flow.

Deformation mechanisms of DBs in volcaniclastic deposits have been highlighted through the findings of this study, providing new insights into the geometry, occurrence and evolution of

DBs in porous volcaniclastic rocks through microstructural study. DBs and their architecture related to faults and lithology are currently being analysed by Jervidalo (in progress, 2018) in a sister MSc project, thus treated herein.

7.2 Further work

This study offers direct documentation and quantification of DBs in volcaniclastic host rocks and their initial deformation mechanism. Building out from this, there are several outstanding questions and venues for future work. Some suggestions for further research are listed below:

- It would be interesting to perform more large-scale outcrop-based study on the architecture and lithological control on the DBs in order to gain further understanding on their architecture. Limitations were met through the microstructural study, as the host rocks contain identical mineral assemblage throughout the three units within the studied succession. However, significant variations of the DBs are observed through different units in the field.
- CT scanning of rock samples featuring network of strands could shed light on further understanding on the development of S-C fabrics. The CT scanning can produce a high-resolution, cross sectional image of the networks without destroying the structural integrity of the sample (e.g. Soh, et al., 1993).
- Permeability measurements can be carried out to investigate the DBs total effect on fluid flow in subsurface reservoirs/aquifers. In addition, transmissivity can be addressed based on permeability and the thickness of the DBs, respectively.
- In general, DBs in volcaniclastic rocks still lacks study and proper understanding. For this reason, more field-based studies would be of great importance for the understanding of nucleation and growth of DBs in volcaniclastic rocks. Experimental studies of DBs by triaxial compression of volcaniclastic rock samples could be carried out, in order to advance the understanding of the initial deformation mechanisms of the bands. A more extensive database would make the classification of DBs in volcaniclastic deposits more predicative.

8 References

Antonellini, M., Aydin, A., and Pollard, D., 1994, Microstructure of deformation bands in porous sandstones at Arches National Park, Utah: Journal of structural geology, v. 16, no. 7, p. 941-959.

Antonellini, M., Petracchini, L., Billi, A., and Scrocca, D., 2014, First reported occurrence of deformation bands in a platform limestone, the Jurassic Calcare Massiccio Fm., northern Apennines, Italy: Tectonophysics, v. 628, p. 85-104.

Aydin, A., 1978, Small faults formed as deformation bands in sandstone, Rock Friction and Earthquake Prediction, Springer, p. 913-930.

Aydin, A., and Ahmadov, R., 2009, Bed-parallel compaction bands in aeolian sandstone: their identification, characterization and implications: Tectonophysics, v. 479, no. 3-4, p. 277-284.

Aydin, A., Borja, R. I., and Eichhubl, P., 2006, Geological and mathematical framework for failure modes in granular rock: Journal of Structural Geology, v. 28, no. 1, p. 83-98.

Aydin, A., and Johnson, A. M., 1978, Development of faults as zones of deformation bands and as slip surfaces in sandstone: Pure and Applied Geophysics, v. 116, no. 4, p. 931-942.

Ballas, G., Fossen, H., and Soliva, R., 2015, Factors controlling permeability of cataclastic deformation bands and faults in porous sandstone reservoirs: Journal of Structural Geology, v. 76, p. 1-21.

Barrier, E., and Angelier, J., 1986, Active collision in eastern Taiwan: the Coastal Range: Tectonophysics, v. 125, no. 1-3, p. 39-72.

Baud, P., Klein, E., and Wong, T.-f., 2004, Compaction localization in porous sandstones: spatial evolution of damage and acoustic emission activity: Journal of Structural Geology, v. 26, no. 4, p. 603-624.

Bense, V., Gleeson, T., Loveless, S., Bour, O., and Scibek, J., 2013, Fault zone hydrogeology: Earth-Science Reviews, v. 127, p. 171-192.

Bense, V., and Person, M., 2006, Faults as conduit-barrier systems to fluid flow in siliciclastic sedimentary aquifers: Water Resources Research, v. 42, no. 5.

Bense, V., Van den Berg, E., and Van Balen, R., 2003, Deformation mechanisms and hydraulic properties of fault zones in unconsolidated sediments; the Roer Valley Rift System, The Netherlands: Hydrogeology Journal, v. 11, no. 3, p. 319-332.

Bésuelle, P., and Rudnicki, J. W., 2004, Localization: shear bands and compaction bands: INTERNATIONAL GEOPHYSICS SERIES., v. 89, p. 219-322.

Beukes, N., Gutzmer, J., and Mukhopadhyay, J., 2003, The geology and genesis of high-grade hematite iron ore deposits: Applied Earth Science, v. 112, no. 1, p. 18-25.

Buatier, M. D., Cavailhes, T., Charpentier, D., Lerat, J., Sizun, J. P., Labaume, P., and Gout, C., 2015, Evidence of multi-stage faulting by clay mineral analysis: Example in a normal fault zone affecting arkosic sandstones (Annot sandstones): Journal of Structural Geology, v. 75, p. 101-117.

Bundschuh, J., and Maity, J. P., 2015, Geothermal arsenic: Occurrence, mobility and environmental implications: Renewable and Sustainable Energy Reviews, v. 42, p. 1214-1222.

Cashman, S., and Cashman, K., 2000, Cataclasis and deformation-band formation in unconsolidated marine terrace sand, Humboldt County, California: Geology, v. 28, no. 2, p. 111-114.

Cavailhes, T., and Rotevatn, A., Submitted, Deformation bands in volcaniclastic rocks - insights from the Shihtiping tuffs, Coastal Range of Taiwan: Journal of Structural Geology.

Chai, B. H., 1972, Structure and tectonic evolution of Taiwan: Am. J. Sci, v. 272, no. 5, p. 389-422.

Chang, C., Angelier, J., Huang, C., and Liu, C., 2001, Structural evolution and significance of a mélange in a collision belt: the Lichi Mélange and the Taiwan arc–continent collision: Geological Magazine, v. 138, no. 6, p. 633-651.

Charalampidou, E.-M., Hall, S. A., Stanchits, S., Lewis, H., and Viggiani, G., 2011, Characterization of shear and compaction bands in a porous sandstone deformed under triaxial compression: Tectonophysics, v. 503, no. 1, p. 8-17.

Chen, J.-C., Geochemistry of andesites from the Coastal Range, eastern Taiwan, *in* Proceedings Proc. Geol. Soc. China1975, Volume 18, p. 73-88.

Chen, W. H., Huang, C. Y., Yan, Y., Dilek, Y., Chen, D., Wang, M. H., Zhang, X., Lan, Q., and Yu, M., 2017, Stratigraphy and provenance of forearc sequences in the Lichi Mélange, Coastal Range: Geological records of the active Taiwan arc-continent collision: Journal of Geophysical Research: Solid Earth, v. 122, no. 9, p. 7408-7436.

Cilona, A., Baud, P., Tondi, E., Agosta, F., Vinciguerra, S., Rustichelli, A., and Spiers, C. J., 2012, Deformation bands in porous carbonate grainstones: Field and laboratory observations: Journal of Structural Geology, v. 45, p. 137-157.

Culshaw, N., 1987, Microstructure, c-axis pattern, microstrain and kinematics of some SC mylonites in Grenville gneiss: Journal of structural geology, v. 9, no. 3, p. 299-311.

Davis, G. H., Bump, A. P., García, P. E., and Ahlgren, S. G., 2000, Conjugate Riedel deformation band shear zones: Journal of Structural Geology, v. 22, no. 2, p. 169-190.

Dimmen, V., Rotevatn, A., Peacock, D. C., Nixon, C. W., and Nærland, K., 2017, Quantifying structural controls on fluid flow: Insights from carbonate-hosted fault damage zones on the Maltese Islands: Journal of Structural Geology, v. 101, p. 43-57.

Dinwiddie, C. L., Bradbury, K. K., McGinnis, R. N., Fedors, R. W., and Ferrill, D. A., 2006, Fault Zone Deformation Overprints Permeability of Nonwelded Ignimbrite: Chalk Cove Fault, Bishop Tuff, Bishop, California: Vadose Zone Journal, v. 5, no. 2, p. 610.

Dinwiddie, C. L., Bradbury, K. K., McGinnis, R. N., Stillman, D. E., and Ferrill, D. A., 2012, Hydrogeologic heterogeneity of faulted and fractured Glass Mountain bedded tuffaceous sediments and ash-fall deposits: The Crucifix site near Bishop, California: Lithosphere, v. 4, no. 1, p. 40-62.

Dobson, P. F., Kneafsey, T. J., Hulen, J., and Simmons, A., 2003, Porosity, permeability, and fluid flow in the Yellowstone geothermal system, Wyoming: Journal of Volcanology and Geothermal Research, v. 123, no. 3, p. 313-324.

Du Bernard, X., Eichhubl, P., and Aydin, A., 2002a, Dilation bands: A new form of localized failure in granular media: Geophysical Research Letters, v. 29, no. 24, p. 29-21.

Du Bernard, X., Labaume, P., Darcel, C., Davy, P., and Bour, O., 2002b, Cataclastic slip band distribution in normal fault damage zones, Nubian sandstones, Suez rift: Journal of Geophysical Research: Solid Earth, v. 107, no. B7.

Egerton, R. F., 2005, Physical principles of electron microscopy, Springer.

Ehrenberg, S., 1993, Preservation of anomalously high porosity in deeply buried sandstones by grain-coating chlorite: examples from the Norwegian continental shelf: AAPG Bulletin, v. 77, no. 7, p. 1260-1286.

Eichhubl, P., Hooker, J. N., and Laubach, S. E., 2010, Pure and shear-enhanced compaction bands in Aztec Sandstone: Journal of Structural Geology, v. 32, no. 12, p. 1873-1886.

Engelder, J. T., 1974, Cataclasis and the generation of fault gouge: Geological Society of America Bulletin, v. 85, no. 10, p. 1515-1522.

Evans, J. P., and Bradbury, K. K., 2004, Faulting and Fracturing of Nonwelded Bishop Tuff, Eastern California: Vadose Zone Journal, v. 3, no. 2, p. 602-623.

Exner, U., and Tschegg, C., 2012, Preferential cataclastic grain size reduction of feldspar in deformation bands in poorly consolidated arkosic sands: Journal of structural geology, v. 43, p. 63-72.

Farooqui, M., Hou, H., Li, G., Machin, N., Neville, T., Pal, A., Wang, Y., Shirivastva, C., Yang, F., and Yin, C., 2009, Evaluating volcanic reservoirs: Oilfield Review, v. 21, no. 1, p. 36-47.

Feng, Z.-q., 2008, Volcanic rocks as prolific gas reservoir: a case study from the Qingshen gas field in the Songliao Basin, NE China: Marine and Petroleum Geology, v. 25, no. 4-5, p. 416-432.

Ferreira, T., and Rasband, W., 2012, ImageJ user guide. IJ1. 46r.: Available: https://imagej.nih.gov/ij/docs/guide/ [Accessed 13.01.18].

Fisher, Q., and Knipe, R., 2001, The permeability of faults within siliciclastic petroleum reservoirs of the North Sea and Norwegian Continental Shelf: Marine and Petroleum Geology, v. 18, no. 10, p. 1063-1081.

Fisher, Q., Knipe, R., and Worden, R., 2009, Microstructures of deformed and non-deformed sandstones from the North Sea: implications for the origins of quartz cement in sandstones: Quartz cementation in sandstones, v. 14, p. 129-146.

Folk, R. L., 1954, The distinction between grain size and mineral composition in sedimentary-rock nomenclature: The Journal of Geology, v. 62, no. 4, p. 344-359.

Fossen, H., 2010, Structural Geology, v. First edition, no. ISBN 978-0-521-51664-8, p. 190-360.

Fossen, H., and Bale, A., 2007, Deformation bands and their influence on fluid flow: AAPG bulletin, v. 91, no. 12, p. 1685-1700.

Fossen, H., Hesthammer, J., Johansen, T. E. S., and Sygnabere, T. O., 2003, Structural geology of the Huldra Field, northern North Sea—a major tilted fault block at the eastern edge of the Horda Platform: Marine and Petroleum Geology, v. 20, no. 10, p. 1105-1118.

Fossen, H., Schultz, R. A., Shipton, Z. K., and Mair, K., 2007, Deformation bands in sandstone: a review: Journal of the Geological Society, v. 164, no. 4, p. 755-769.

Fossen, H., Soliva, R., Ballas, G., Trzaskos, B., Cavalcante, C., and Schultz, R. A., 2018, A review of deformation bands in reservoir sandstones: geometries, mechanisms and distribution: Geological Society, London, Special Publications, v. 459, no. 1, p. 9-33.

Fossen, H., Zuluaga, L. F., Ballas, G., Soliva, R., and Rotevatn, A., 2015, Contractional deformation of porous sandstone: Insights from the Aztec Sandstone, SE Nevada, USA: Journal of Structural Geology, v. 74, p. 172-184.

Gibson, R. G., 1998, Physical character and fluid-flow properties of sandstone-derived fault zones: Geological Society, London, Special Publications, v. 127, no. 1, p. 83-97.

Hesthammer, J., and Fossen, H., 2001, Structural core analysis from the Gullfaks area, northern North Sea: Marine and Petroleum Geology, v. 18, no. 3, p. 411-439.

Hirtzel, J., Chi, W.-C., Reed, D., Chen, L., Liu, C.-S., and Lundberg, N., 2009, Destruction of Luzon forearc basin from subduction to Taiwan arc–continent collision: Tectonophysics, v. 479, no. 1, p. 43-51.

Ho, C., 1986, A synthesis of the geologic evolution of Taiwan: Tectonophysics, v. 125, no. 1-3, p. 1-16.

Hsieh, M.-L., Liew, P.-M., and Hsu, M.-Y., 2004, Holocene tectonic uplift on the Hua-tung coast, eastern Taiwan: Quaternary International, v. 115, p. 47-70.

Issen, K., and Rudnicki, J., 2001, Theory of compaction bands in porous rock: Physics and Chemistry of the Earth, Part A: Solid Earth and Geodesy, v. 26, no. 1-2, p. 95-100.

Jahn, B., Martineau, F., Peucat, J., and Cornichet, J., 1986, Geochronology of the Tananao schist complex, Taiwan, and its regional tectonic significance: Tectonophysics, v. 125, no. 1-3, p. 103-124.

Kana, J. D., Djongyang, N., Raïdandi, D., Nouck, P. N., and Dadjé, A., 2015, A review of geophysical methods for geothermal exploration: Renewable and Sustainable Energy Reviews, v. 44, p. 87-95.

Kolyukhin, D., Schueller, S., Espedal, M. S., and Fossen, H., 2010, Deformation band populations in fault damage zone—impact on fluid flow: Computational Geosciences, v. 14, no. 2, p. 231-248.

Korkanç, M., and Solak, B., 2016, Estimation of engineering properties of selected tuffs by using grain/matrix ratio: Journal of African Earth Sciences, v. 120, p. 160-172.

Kosuga, M., Sato, H., Tanaka, T., and Sheu, H. C., 1988, Crustal movement along a collision boundary of plates (case of eastern Taiwan): Journal of geodynamics, v. 10, no. 2-4, p. 189-205.

Krinsley, D. H., Pye, K., Boggs Jr, S., and Tovey, N. K., 2005, Backscattered scanning electron microscopy and image analysis of sediments and sedimentary rocks, Cambridge University Press.

La Felice, S., Montanari, D., Battaglia, S., Bertini, G., and Gianelli, G., 2014, Fracture permeability and water–rock interaction in a shallow volcanic groundwater reservoir and the concern of its interaction with the deep geothermal reservoir of Mt. Amiata, Italy: Journal of Volcanology and Geothermal Research, v. 284, p. 95-105.

Lai, Y.-M., and Song, S.-R., 2013, The volcanoes of an oceanic arc from origin to destruction: A case from the northern Luzon Arc: Journal of Asian Earth Sciences, v. 74, p. 97-112.

Lenhardt, N., and Götz, A. E., 2011, Volcanic settings and their reservoir potential: An outcrop analog study on the Miocene Tepoztlán Formation, Central Mexico: Journal of Volcanology and Geothermal Research, v. 204, no. 1, p. 66-75.

Liew, P., Pirazzoli, P., Hsieh, M., Arnold, M., Barusseau, J., Fontugne, M., and Giresse, P., 1993, Holocene tectonic uplift deduced from elevated shorelines, eastern Coastal Range of Taiwan: Tectonophysics, v. 222, no. 1, p. 55-68.

Lindsey, D. A., 1982, Tertiary volcanic rocks and uranium in the Thomas Range and northern Drum Mountains, Juab County, Utah: USGPO, 2330-7102.

Lister, G., and Snoke, A., 1984, SC mylonites: Journal of Structural Geology, v. 6, no. 6, p. 617-638.

Lothe, A., Gabrielsen, R., Hagen, N. B., and Larsen, B., 2002, An experimental study of the texture of deformation bands: effects on the porosity and permeability of sandstones: Petroleum Geoscience, v. 8, no. 3, p. 195-207.

Mair, K., Elphick, S., and Main, I., 2002, Influence of confining pressure on the mechanical and structural evolution of laboratory deformation bands: Geophysical Research Letters, v. 29, no. 10.

Mair, K., Main, I., and Elphick, S., 2000, Sequential growth of deformation bands in the laboratory: Journal of Structural Geology, v. 22, no. 1, p. 25-42.

Malavieille, J., and Trullenque, G., 2009, Consequences of continental subduction on forearc basin and accretionary wedge deformation in SE Taiwan: Insights from analogue modeling: Tectonophysics, v. 466, no. 3-4, p. 377-394.

Mao, J. W., Pirajno, F., Zhang, Z. H., Chai, F. M., Wu, H., Chen, S. P., Cheng, L. S., Yang, J. M., and Zhang, C. Q., 2008, A review of the Cu–Ni sulphide deposits in the Chinese Tianshan and Altay orogens (Xinjiang Autonomous Region, NW China): principal characteristics and ore-forming processes: Journal of Asian Earth Sciences, v. 32, no. 2-4, p. 184-203.

Mayer, A., May, W., Lukkarila, C., and Diehl, J., 2007, Estimation of fault-zone conductance by calibration of a regional groundwater flow model: Desert Hot Springs, California: Hydrogeology Journal, v. 15, no. 6, p. 1093-1106.

McGinnis, R. N., Morris, A. P., Ferrill, D. A., and Dinwiddie, C. L., 2009, Deformation analysis of tuffaceous sediments in the Volcanic Tableland near Bishop, California: Lithosphere, v. 1, no. 5, p. 291-304.

Mielke, P., Nehler, M., Bignall, G., and Sass, I., 2015, Thermo-physical rock properties and the impact of advancing hydrothermal alteration—A case study from the Tauhara geothermal field, New Zealand: Journal of Volcanology and Geothermal Research, v. 301, p. 14-28.

Miyashiro, A., 1974, Volcanic rock series in island arcs and active continental margins: Amer. Jour. Sci., v. 274, p. 321-355.

Mollema, P., and Antonellini, M., 1996, Compaction bands: a structural analog for anti-mode I cracks in aeolian sandstone: Tectonophysics, v. 267, no. 1, p. 209-228.

Moon, V. G., 1993, Geotechnical characteristics of ignimbrite: A soft pyroclastic rock type: Engineering Geology, v. 35, no. 1-2, p. 33-48.

Nicchio, M. A., Nogueira, F. C., Balsamo, F., Souza, J. A., Carvalho, B. R., and Bezerra, F. H., 2018, Development of cataclastic foliation in deformation bands in feldspar-rich conglomerates of the Rio do Peixe Basin, NE Brazil: Journal of Structural Geology, v. 107, p. 132-141.

Okubo, C. H., 2012, Spatial distribution of damage around faults in the Joe Lott Tuff Member of the Mount Belknap Volcanics, Utah: A mechanical analog for faulting in pyroclastic deposits on Mars: Journal of Geophysical Research: Planets, v. 117, no. E8.

Okubo, C. H., Schultz, R. A., Chan, M. A., and Komatsu, G., 2009, Deformation band clusters on Mars and implications for subsurface fluid flow: Geological Society of America Bulletin, v. 121, no. 3-4, p. 474-482.

Page, B. M., and Suppe, J., 1981, The Pliocene Lichi melange of Taiwan; its plate-tectonic and olistostromal origin: American Journal of Science, v. 281, no. 3, p. 193-227.

Pola, A., Martínez-Martínez, J., Macías, J. L., Fusi, N., Crosta, G., Garduño-Monroy, V. H., and Núñez-Hurtado, J., 2016, Geomechanical characterization of the Miocene Cuitzeo ignimbrites, Michoacán, Central Mexico: Engineering Geology, v. 214, p. 79-93.

Rawling, G. C., and Goodwin, L. B., 2003, Cataclasis and particulate flow in faulted, poorly lithified sediments: Journal of Structural Geology, v. 25, no. 3, p. 317-331.

Reed, S. J. B., 2005, Electron microprobe analysis and scanning electron microscopy in geology, Cambridge University Press.

Reichelt, R., 2007, Scanning electron microscopy, Science of microscopy, Springer, p. 133-272.

Rotevatn, A., Buckley, S. J., Howell, J. A., and Fossen, H., 2009, Overlapping faults and their effect on fluid flow in different reservoir types: A LIDAR-based outcrop modeling and flow simulation study: AAPG bulletin, v. 93, no. 3, p. 407-427.

Rotevatn, A., and Fossen, H., 2011, Simulating the effect of subseismic fault tails and process zones in a siliciclastic reservoir analogue: Implications for aquifer support and trap definition: Marine and Petroleum Geology, v. 28, no. 9, p. 1648-1662.

Rotevatn, A., and Fossen, H., 2012, Soft faults with hard tips: magnitude-order displacement gradient variations controlled by strain softening versus hardening; implications for fault scaling: Journal of the Geological Society, v. 169, no. 2, p. 123-126.

Rotevatn, A., Sandve, T., Keilegavlen, E., Kolyukhin, D., and Fossen, H., 2013, Deformation bands and their impact on fluid flow in sandstone reservoirs: the role of natural thickness variations: Geofluids, v. 13, no. 3, p. 359-371.

Rotevatn, A., Thorsheim, E., Bastesen, E., Fossmark, H. S. S., Torabi, A., and Sælen, G., 2016, Sequential growth of deformation bands in carbonate grainstones in the hangingwall of an active growth fault: Implications for deformation mechanisms in different tectonic regimes: Journal of Structural Geology, v. 90, p. 27-47.

Rotevatn, A., Torabi, A., Fossen, H., and Braathen, A., 2008, Slipped deformation bands: A new type of cataclastic deformation bands in Western Sinai, Suez rift, Egypt: Journal of Structural Geology, v. 30, no. 11, p. 1317-1331.

Rustichelli, A., Tondi, E., Agosta, F., Cilona, A., and Giorgioni, M., 2012, Development and distribution of bed-parallel compaction bands and pressure solution seams in carbonates (Bolognano Formation, Majella Mountain, Italy): Journal of Structural Geology, v. 37, p. 181-199.

Rühaak, W., Guadagnini, A., Geiger, S., Bär, K., Gu, Y., Aretz, A., Homuth, S., and Sass, I., 2015, Upscaling thermal conductivities of sedimentary formations for geothermal exploration: Geothermics, v. 58, p. 49-61.

Sass, I., and Götz, A. E., 2012, Geothermal reservoir characterization: a thermofacies concept: Terra Nova, v. 24, no. 2, p. 142-147.

Saunders, J., Lee, M.-K., Shamsudduha, M., Dhakal, P., Uddin, A., Chowdury, M., and Ahmed, K., 2008, Geochemistry and mineralogy of arsenic in (natural) anaerobic groundwaters: Applied Geochemistry, v. 23, no. 11, p. 3205-3214.

Sibson, R. H., 1996, Structural permeability of fluid-driven fault-fracture meshes: Journal of Structural Geology, v. 18, no. 8, p. 1031-1042.

Sibuet, J., and Hsu, S., 2004, How was Taiwan created?: Tectonophysics, v. 379, no. 1, p. 159-181.

Sibuet, J.-C., and Hsu, S.-K., 1997, Geodynamics of the Taiwan arc-arc collision: Tectonophysics, v. 274, no. 1, p. 221-251.

Sibuet, J.-C., Hsu, S.-K., Le Pichon, X., Le Formal, J.-P., Reed, D., Moore, G., and Liu, C.-S., 2002, East Asia plate tectonics since 15 Ma: constraints from the Taiwan region: Tectonophysics, v. 344, no. 1, p. 103-134.

Soden, A., Lunn, R., and Shipton, Z., 2016, Impact of mechanical heterogeneity on joint density in a welded ignimbrite: Journal of Structural Geology, v. 89, p. 118-129.

Soden, A. M., and Shipton, Z. K., 2013, Dilational fault zone architecture in a welded ignimbrite: The importance of mechanical stratigraphy: Journal of Structural Geology, v. 51, p. 156-166.

Soh, W., Byrne, T., Taira, A., and Kono, A., 1993, 10. COMPUTED TOMOGRAPHY (CT) SCAN IMAGE ANALYSIS OF SITE 808 CORES: STRUCTURAL AND PHYSICAL PROPERTY IMPLICATIONS1.

Song, S.-R., and Lo, H.-J., 1988, Volcanic geology of Fengpin-Takangkou area, coastal range of Taiwan: Yánjiū bāogāo-Guólè Táiwān dāxué. Lǐxuéyuān dèzhèxué xè, no. 26, p. 223-235.

Song, S.-R., and Lo, H.-J., 2002, Lithofacies of volcanic rocks in the central Coastal Range, eastern Taiwan: implications for island arc evolution: Journal of Asian Earth Sciences, v. 21, no. 1, p. 23-38.

Stephan, J. F., Blanchet, R., Rangin, C., Pelletier, B., Letouzey, J., and Muller, C., 1986, Geodynamic evolution of the Taiwan-Luzon-Mindoro belt since the late Eocene: Tectonophysics, v. 125, no. 1-3, p. 245-268.

Sternlof, K. R., Karimi-Fard, M., Pollard, D., and Durlofsky, L., 2006, Flow and transport effects of compaction bands in sandstone at scales relevant to aquifer and reservoir management: Water Resources Research, v. 42, no. 7, p. W07425.

Storvoll, V., Bjørlykke, K., Karlsen, D., and Saigal, G., 2002, Porosity preservation in reservoir sandstones due to grain-coating illite: a study of the Jurassic Garn Formation from the Kristin and Lavrans fields, offshore Mid-Norway: Marine and Petroleum Geology, v. 19, no. 6, p. 767-781.

Tamura, Y., Busby, C. J., Blum, P., Guèrin, G., Andrews, G. D. M., Barker, A. K., Berger, J. L. R., Bongiolo, E. M., Bordiga, M., DeBari, S. M., Gill, J. B., Hamelin, C., Jia, J., John, E. H., Jonas, A. S., Jutzeler, M., Kars, M. A. C., Kita, Z. A., Konrad, K., Mahony, S. H., Martini, M., Miyazaki, T., Musgrave, R. J., Nascimento, D. B., Nichols, A. R. L., Ribeiro, J. M., Sato, T., Schindlbeck, J. C., Schmitt, A. K., Straub, S. M., Vautravers, M. J., and and Yang, Y., 2015, Expedition 350 methods: Available: http://publications.iodp.org/proceedings/350/102/350_102.html [Accessed 27.04.17].

Tang, H., Kong, T., Liu, X., Yang, D., Huo, H., and Huang, Y., 2017, Formation mechanism of high-quality reservoirs of Lower Cretaceous volcaniclastic sedimentary rocks in Songliao Basin: Petroleum Research, v. 2, no. 2, p. 186-198.

Teng, L. S., 1990, Geotectonic evolution of late Cenozoic arc-continent collision in Taiwan: Tectonophysics, v. 183, no. 1-4, p. 57-76.

Teng, L. S., Chen, W.-S., Wang, Y., Song, S.-R., and Lo, H.-J., 1988, Toward a comprehensive stratigraphic system of the Coastal Range, eastern Taiwan: Acta Geologica Taiwanica, v. 26, p. 19-36.

Teng, L. S., and Wang, Y., Island arc system of the Coastal Range, eastern Taiwan, *in* Proceedings Proc. Geol. Soc. China1981, Volume 24, p. 99-112.

Thomas, M. Y., Avouac, J.-P., Gratier, J.-P., and Lee, J.-C., 2014a, Lithological control on the deformation mechanism and the mode of fault slip on the Longitudinal Valley Fault, Taiwan: Tectonophysics, v. 632, p. 48-63.

Thomas, M. Y., Avouac, J. P., Champenois, J., Lee, J. C., and Kuo, L. C., 2014b, Spatiotemporal evolution of seismic and aseismic slip on the Longitudinal Valley Fault, Taiwan: Journal of Geophysical Research: Solid Earth, v. 119, no. 6, p. 5114-5139.

Thorsheim, E., 2015, The geometry and evolution of deformation bands in carbonate grainstones along the Maghlaq Fault, Malta: MSc. thesis, University of Bergen, Bergen, 91 p.

Tindall, S., and Eckert, A., 2015, Geometric and mechanical-stiffness controls on jointing in cataclastic deformation bands: Journal of Structural Geology, v. 77, p. 126-137.

Tondi, E., Antonellini, M., Aydin, A., Marchegiani, L., and Cello, G., 2006, The role of deformation bands, stylolites and sheared stylolites in fault development in carbonate grainstones of Majella Mountain, Italy: Journal of structural geology, v. 28, no. 3, p. 376-391.

Tondi, E., Cilona, A., Agosta, F., Aydin, A., Rustichelli, A., Renda, P., and Giunta, G., 2012, Growth processes, dimensional parameters and scaling relationships of two conjugate sets of compactive shear bands in porous carbonate grainstones, Favignana Island, Italy: Journal of Structural Geology, v. 37, p. 53-64.

Torabi, A., 2014, Cataclastic bands in immature and poorly lithified sandstone, examples from Corsica, France: Tectonophysics, v. 630, p. 91-102.

Torabi, A., Braathen, A., Cuisiat, F., and Fossen, H., 2007, Shear zones in porous sand: Insights from ring-shear experiments and naturally deformed sandstones: Tectonophysics, v. 437, no. 1, p. 37-50.

Torabi, A., and Fossen, H., 2009, Spatial variation of microstructure and petrophysical properties along deformation bands in reservoir sandstones, v. 93, no. AAPG Bulletin, p. 919-938.

Torabi, A., Fossen, H., and Braathen, A., 2013, Insight into petrophysical properties of deformed sandstone reservoirs: AAPG bulletin, v. 97, no. 4, p. 619-637.

Twiss, R. J., and Moores, E. M., 1992, Structural geology, San Francisco, CA, Macmillan.

Ujiie, K., Maltman, A. J., and Sánchez-Gómez, M., 2004, Origin of deformation bands in argillaceous sediments at the toe of the Nankai accretionary prism, southwest Japan: Journal of structural geology, v. 26, no. 2, p. 221-231.

van der Meer, J. J., Menzies, J., and Rose, J., 2003, Subglacial till: the deforming glacier bed: Quaternary Science Reviews, v. 22, no. 15, p. 1659-1685.

Vinciguerra, S., Del Gaudio, P., Mariucci, M., Marra, F., Meredith, P., Montone, P., Pierdominici, S., and Scarlato, P., 2009, Physical properties of tuffs from a scientific borehole at Alban hills volcanic district (central Italy): Tectonophysics, v. 471, no. 1, p. 161-169.

Von Hagke, C., Philippon, M., Avouac, J.-P., and Gurnis, M., 2016, Origin and time evolution of subduction polarity reversal from plate kinematics of Southeast Asia: Geology, v. 44, no. 8, p. 659-662.

Walderhaug, O., 1996, Kinetic modeling of quartz cementation and porosity loss in deeply buried sandstone reservoirs: AAPG bulletin, v. 80, no. 5, p. 731-745.

Wibberley, C., 1999, Are feldspar-to-mica reactions necessarily reaction-softening processes in fault zones?: Journal of Structural Geology, v. 21, no. 8-9, p. 1219-1227.

Wilson, J. E., Goodwin, L. B., and Lewis, C. J., 2003, Deformation bands in nonwelded ignimbrites: Petrophysical controls on fault-zone deformation and evidence of preferential fluid flow: Geology, v. 31, no. 10, p. 837-840.

Wilson, J. E., Goodwin, L. B., and Lewis, C. J., 2006, Diagenesis of deformation band faults: Record and mechanical consequences of vadose zone flow and transport in the Bandelier Tuff, Los Alamos, New Mexico: Journal of Geophysical Research, v. 111, no. B9.

Wittke, J. H., 2015, Electron Microanalysis Core Facility [Online]. Northern Arizona University, Flagstaff, Arizona.: Available: http://nau.edu/cefns/labs/electron-microprobe/glg-510-class-notes/instrumentation/ [Accessed 12.01.18].

Yamaguchi, M., and Ota, Y., 2004, Tectonic interpretations of Holocene marine terraces, east coast of Coastal Range, Taiwan: Quaternary International, v. 115-116, p. 71-81.

Yu, S.-B., and Kuo, L.-C., 2001, Present-day crustal motion along the Longitudinal Valley Fault, eastern Taiwan: Tectonophysics, v. 333, no. 1, p. 199-217.

Yuan, R.-m., Zhang, B.-l., Xu, X.-w., Lin, C.-y., and Han, Z.-j., 2015, Microstructural and mineral analysis on the fault gouge in the coseismic shear zone of the 2008 M w 7.9 Wenchuan earthquake: International Journal of Earth Sciences, v. 104, no. 5, p. 1425-1437.

Yui, T., Maki, K., Lan, C., Hirata, T., Chu, H., Kon, Y., Yokoyama, T., Jahn, B., and Ernst, W., 2012, Detrital zircons from the Tananao metamorphic complex of Taiwan: Implications for sediment provenance and Mesozoic tectonics: Tectonophysics, v. 541, p. 31-42.

Zhou, W., Apkarian, R., Wang, Z. L., and Joy, D., 2006, Fundamentals of scanning electron microscopy (SEM), Scanning microscopy for nanotechnology, Springer, p. 1-40.

Zhu, W., Baud, P., Vinciguerra, S., and Wong, T. f., 2011, Micromechanics of brittle faulting and cataclastic flow in Alban Hills tuff: Journal of Geophysical Research: Solid Earth, v. 116, no. B6.

Zhu, W., Baud, P., and Wong, T. f., 2010, Micromechanics of cataclastic pore collapse in limestone: Journal of Geophysical Research: Solid Earth, v. 115, no. B4, p. B04405.

Appendix I: Figures in high quality

The following link will direct you to a google drive folder with all the “home-made” figures from this thesis in full quality. Some of the images were compressed in this document due to high file sizes.

Link: https://drive.google.com/open?id=1L1y24uhFTc4IFZHylyzCLHOUSOdSQtfn

Appendix II: Field data and measurements

Lok. 1-1-A	No. Strands	Spacing (cm)	Thickness (mm)	Tot. Thickness(cm)	Offsett (mm)	Total offsett	Strike/dip
100cm	10	8,7	2	68,5			244/71
		2,1	1				222/75
		1,2	2				235/79
		9	2				236/65
		2	2				241/70
		13	1				231/76
		2,9	2				227/75
		7,6	2				217/63
		6	1				221/76
			1				223/59
130cm	14	5,4	1	63			221/61
		4,2	2				224/73
		2,5	1,5				225/73
		4,5	1				226/74
		4,2	1,5				223/70
		5	1,5				222/77
		4,1	2				214/70
		4,6	2				223/75
		2,4	2				220/68
		4	1				216/70
		2,9	2				211/70
		1	2				215/78
		2	2				208/75
		0,8	2				216/65
		2,1	1,5				215/77
		3	1				211/77
		7,5	1				208/78
			1				201/71
160cm	13	5,3	2	62			191/69
		7,3	1				187/60
		4,6	1				194/60
		4	1,5				190/63
		6,3	1				198/64
		7,4	2				186/67
		6,3	1				182/67
		3,6	1				183/62
		5	0,5				178/62
		2,6	2				181/73
		5,1	1				175/67
		2,6	2				170/72
			3				171/64
190cm	13	21,2	3	73,85			165/65
		3,6	2				172/61
		11,2	2				186/48
		2,1	0,5				
		3,1	1				
		6	1				
		3,5	1				
		5,4	1,5				
		5,2	2				
		2,5	1,5				
		4,5	2				
		3,3	3				
			2				

Lok. 1-2-A	No. Strands	Spacing (cm)	Thickness (mm)	Tot. Thickness(cm)	Offsett (mm)	Total offsett	Strike/dip
50cm	5	14	3	35,8			215/76
		9,4	3				228/74
		5,7	4				218/71
		5,5	3				218/63
			3				218/68
80cm	5	18,5	5	44,1			218/70
		11,3	5				215/71
		8	4				213/75
		4	4				218/77
			5				208/73
120cm	5	6,7	5	54,8			205/68
		7,5	5				210/72
		17	8				216/74
		20,5	5				208/70
			8				209/75
150cm	6	7,1	5	66,7			214/70
		16,1	8				205/65
		4	5				211/74
		18,4	8				216/68
		17,5	5				223/70
			5				209/75
							209/74
							220/67
							221/70
							214/66

lok. 2-1-A	No. Strands	Spacing (cm)	Thickness (mm)	Tot. Thickness(cm)	Offsett (mm)	Total offsett	Strike/dip: Flat-segment	Strike/dip: Ramp-thrust	Strike/dip: Back-thrust	Striations: Backthrust
	7	10,5	0,5	87,5	6	7,22	173/24	201/52	357/28	22-090
		7	0,3		0,1		184/22	213/52	350/31	30-087
		11,5	0,5		0,1		178/22	197/44	351/43	23-092
		13	0,5		15		186/23	208/46	002/28	26-092
		27	0,5		25		178/21	225/47	353/38	42-093
		18,5	0,3		17		180/23	206/38	359/37	20-094
			0,3		9		178/24	194/43	355/44	27-098
							173/22	195/44	357/42	27-094
							182/24	183/51	352/49	28-081
							191/19	198/43	353/49	25-084
							187/29	189/47	354/44	34-072
							184/26	191/48	357/40	37-072
								186/41	358/42	
								198/43	000/46	
								194/42	355/39	
								197/42	353-40	
								196/41	352/42	
								194/41	354/34	
								217/44	001/39	
									347/41	
									353/33	
									357/34	
									355/38	

Lok. 2-2-A	No. Strands	Spacing (cm)	T (mm)	Ttot (cm)	O	Otot (cm)	Strike/dip: Flat-segment	Striations: Flat-segment
50	3	14	2	23		50	185/29	26-304
		2	1				185/27	23-286
			7				194/25	29-279
90	1		2	2		50	194/27	25-287
120	2	120	8	13			196/33	25-287
			2				185/32	23-289
							188/34	23-302
							185/31	20-318
							185/29	23-297
							184/30	
							190/30	
							193/27	

Lok. 3-1-A	No. Strands	Spacing (cm)	Thickness (mm)	Tot. Thickness(cm)	Offsett (mm)	Total offsett	Strike/dip
30cm	5	1,5	0,1	14,2		60	099/80
		2	0,3				095/80
		1,5	0,3				090/84
		1	7				108/78
			0,5				098/80
50cm	10	1	0,3	29,8		70	092/87
		1,3	1				099/82
		7	0,3				111/81
		1,8	1				113/80
		2	0,2				119/83
		3	4				116/73
		1,5	1				126/75
		1	1				125/83
		1	1				132/73
			0,4				129/67
70cm	12	26	1	74,6		30	124/65
		1,5	2				131/58
		1	0,8				120/63
		2,3	0,5				116/60
		6	0,5				122/67
		3,5	0,8				125/72
		3,8	0,8				131/59
		4	0,5				125/68
		3	0,5				126/67
		5	0,8				126/62
		3	0,8				134/63
		4	1				125/58
			2				
90cm	14	4	1	108,8		55	
		28	1				
		23	1				
		4	0,8				
		3	0,8				
		2	0,5				
		4	1				
		6	1,5				
		2	1				
		4	1				
		3	0,8				
		5	1				
		3	0,8				
		4	0,8				
			0,8				
110	10	4	1	158,6		70	
		32	1				
		44	3				
		3	1				
		17	1				
		4	1				
		6	0,8				
		30	0,8				
		7	1				
			1				
140	12	39	0,8	197,2		40	
		5	1				
		51	1				
		13	0,5				
		28	0,3				
		4	0,3				
		8	0,5				
		4	1				
		4	1				
		25	0,8				
		5	2				
			2				

Lok. 3-2-A	No. Strands	Spacing (cm)	Thickness (mm)	Tot. Thickness(cm)	Offsett (mm)	Total offsett	Strike/dip
30cm	10	4	2	31,3			249/89
		4	1				252/86
		2	0,5				250/86
		2	0,5				248/89
		5	2				253/86
		2	0,5				251/86
		1,5	0,5				248/89
		1,5	0,3				253/86
		1	0,5				251/85
			0,5				252/87
30cm	3	1	0,3	9,9			251/88
		4	0,3				253/88
		1,5	2				251/88
			0,8				250/88
70cm	5	2,5	0,8	12,9		55	
		1,5	0,8				
		2	0,5				
		3	1				
			0,8				
90cm	8	1,5	1	37,3		74	
		2	1				
		1,5	1				
		3	0,5				
		7	0,5				
		13	0,5				
		3	0,8				
			1				

Lok. 3-3-A	No. Strands	Spacing (cm)	Thickness (mm)	Tot. Thickness(cm)	Offsett (mm)	Total offsett	Strike/dip
30cm	3	0,4	1	3,45	9	13,4	246/69
		2,8	0,5				245/72
			1		1,7		258/69
60cm	6	1,8	1	4,8	7,2	19,6	253/68
		0,8	1		0,7		249/68
		1	1		1,2		252/67
		0,4	0,5		0,8		252/63
		0,3	1		0,2		247/70
			0,5		0,6		256/70
90cm	6	1,6	13	6,3	5		253/66
	(5+1 cluster)	0,3	1		2,8		253/72
		1,7	1				251/70
		0,4	1		0,6		251/65
		0,5	1		0,3		253/61
			1				254/72
120cm	6	1,5	1,5	5,45			256/74
		0,2	1				249/69
		1,8	1				250/71
		0,8	2				255/67
		0,2	3				
			1				